

2018

Cross Calibration and Validation of Landsat 8 OLI and Sentinel 2A MSI

M. M. Farhad

South Dakota State University

Follow this and additional works at: <https://openprairie.sdstate.edu/etd>

 Part of the [Electrical and Computer Engineering Commons](#), and the [Remote Sensing Commons](#)

Recommended Citation

Farhad, M. M., "Cross Calibration and Validation of Landsat 8 OLI and Sentinel 2A MSI" (2018). *Electronic Theses and Dissertations*. 2687.

<https://openprairie.sdstate.edu/etd/2687>

This Thesis - Open Access is brought to you for free and open access by Open PRAIRIE: Open Public Research Access Institutional Repository and Information Exchange. It has been accepted for inclusion in Electronic Theses and Dissertations by an authorized administrator of Open PRAIRIE: Open Public Research Access Institutional Repository and Information Exchange. For more information, please contact michael.biondo@sdstate.edu.

CROSS CALIBRATION AND VALIDATION OF LANDSAT 8 OLI AND SENTINEL

2A MSI

BY

M M FARHAD

A thesis submitted in the partial fulfilment of the requirement for the

Master of Science

Major in Electrical Engineering

South Dakota State University

2018

CROSS CALIBRATION AND VALIDATION OF LANDSAT 8 OLI AND SENTINEL
2A MSI

This thesis is approved as a creditable and independent investigation by a candidate for the Master of Science in Electrical Engineering degree and is acceptable for meeting the thesis requirements for this degree. Acceptance of this thesis does not imply that the conclusions reached by the candidate are necessarily the conclusions of the major departments.

Morakot Kaewmancee
Thesis Advisor

Date

Dennis Helder, PhD
Major Advisor

Date

Steven Hietpas, PhD
Head, Electrical Engineering & Computer Science

Date

Dean, Graduate School

Date

ACKNOWLEDGEMENTS

I would like to express my deepest gratitude to my advisor, Dr. Dennis Helder. Without his advice, inspiration and guidance, this project would not have been possible. I appreciate the support he has given me in my time at South Dakota State University.

My sincere thanks go to my thesis advisor, Morakot Kaewmanee, whose wisdom and encouragement were the driving force behind this project. I appreciate the time and dedication she has provided in support of this work. My heartfelt thanks and gratitude also go to Larry Leigh, who has provided invaluable technical support and knowledge in support of this project.

My special thanks go to Tim Ruggles, who has provided invaluable assistance in the grammatical review and edited the thesis content. I am grateful to him for the time he has spent in this endeavor.

I am grateful to my peers in the Image Processing Laboratory, who have supported me at all times, and encouraged me to continue with this project to its completion.

Finally, I would like to dedicate this thesis to my parents. Without their continued love and support, this project would not have been possible.

TABLE OF CONTENTS

ABBREVIATIONS.....	vi
LIST OF FIGURES.....	ix
LIST OF TABLES.....	xii
ABSTRACT.....	xiv
Chapter 1 Introduction.....	1
1.1 Cross Calibration	2
1.2 Comparison of MSI and OLI Radiometric Performance	3
1.2.1 Sentinel 2A	4
1.2.2 Landsat 8	5
1.2.3 Side-by-Side Comparison	7
1.3 Summary	7
 Chapter 2 Literature Review	 9
2.1 Calibration Site Selection	9
2.1.1 Saharan and Arabian Desert Sites	9
2.1.2 CEOS Recommended PICS and Calibration	10
2.2 SBAF in Cross Calibration	11
2.3 BRDF Correction	13
2.4 Cross Calibration	15
2.5 Uncertainty of Cross Calibration	19
2.5.1 Uncertainty in SBAF	20

2.5.2	Other Sources of Uncertainty	20
2.6	Summary	21
Chapter 3	Methodology	23
3.1	Select Appropriate Region(s) of Interest	24
3.2	Scene Pair Selection	25
3.3	SBAF Calculation and Correction	25
3.4	BRDF Modeling and Correction	26
3.5	Gain and Offset Calculation	29
3.6	Uncertainty Analysis	31
3.6.1	Uncertainty in Spectral Domain	31
3.6.1.1	Uncertainty in Prelaunch RSR	31
3.6.1.2	Uncertainty Due to Spectral Filter Changes	31
3.6.1.3	Uncertainty in Hyperspectral Profile Interpolation	33
3.6.2	Uncertainty in Spatial Domain	34
3.6.2.1	Uncertainty Due to Geometric Registration Error	34
3.6.2.2	Uncertainty Due to Differences in Spatial Resolutio.....	35
3.6.2.3	Uncertainty Due to Site Non-Uniformity	36
3.6.3	Uncertainty in Temporal Domain	37
3.6.3.1	Uncertainty Due to Sun Angle Differences	38
3.6.3.2	Uncertainty Due to Atmospheric Change	38
3.7	Summary	39

Chapter 4	Result and Discussion	40
4.1	Scene Pairs	40
4.2	SBAF Calculations	41
4.3	BRDF Models and Correction	44
4.3.1	Reference Angle Selection	47
4.4	Gain and Bias Calculation	49
4.5	Uncertainty Estimation	52
4.5.1	Uncertainty in Spectral Domain	51
4.5.1.1	Uncertainty Inherent in RSR Measurement	53
4.5.1.1	Uncertainty Due to Spectral Filter Change	53
4.5.1.2	Uncertainty Due to Spectral Bandwidth Change	53
4.5.2	Uncertainty in Spatial Domain	57
4.5.2.1	Uncertainty Due to Image Registration Error	57
4.5.2.2	Uncertainty Due to Spatial Resolution Mismatch	60
4.5.2.3	Uncertainty Due to Site Spatial Non-Uniformity	61
4.5.3	Uncertainty in Temporal Domain	61
4.5.3.1	Uncertainty Due to Overpass Time Difference	61
4.5.3.2	Uncertainty Due to Atmospheric Variation	65
4.5.4	Summary of Uncertainty Analysis	68
4.6	Validation	69
4.7	Summary	75

Chapter 5	Conclusion	78
5.1	Process Recommendation	78
5.2	Direction of Future Work	79
References		81
Appendix		87

ABBREVIATIONS

ALI	Advanced Land Imager
AVHRR	Advanced Very High Resolution Radiometer
BRDF	Bidirectional Reflectance Distribution Factor
CA	Coastal Aerosol
CEOS	Committee on Earth Observation Sciences
CMOS	Complementary Metal Oxide Semiconductor
DN	Digital Number
EO	Earth Orbiting
ESA	European Space Agency
ETM+	Enhanced Thematic Mapper Plus
FOV	Field of View
MERIS	MEDium Resolution Imaging Spectrometer
MLST	Mean Local Solar Time
MODIS	MODerate-resolution Imaging Spectroradiometer
MODTRAN	MODerate resolution atmospheric TRANsmission
MSI	MultiSpectral Instrument
NIR	Near Infrared
NOAA	National Oceanic and Atmospheric Administration
OLI	Operational Land Imager
PICS	Pseudo Invariant Calibration Sites
POLDER	POLarization and Directionality of the Earth's Reflectances
ROI	Region of Interest
RRV	Railroad Valley Playa
RSR	Relative Spectral Response
SAA	Solar Azimuth Angle

SBAF	Spectral Band Adjustment Factor
SNO	Simultaneous Nadir Overpass
SNR	Signal to Noise Ratio
SWIR	Short Wave Infrared
SZA	Solar Zenith Angle
TIRS	Thermal Infrared Sensor
TOA	Top of Atmosphere
TRUTHS	Traceable Radiometry Underpinning Terrestrial and Helio Studies
VAA	View Azimuth Angle
VNIR	Visible Near Infrared
VZA	View Zenith Angle
WRS	Worldwide Reference System

LIST OF FIGURES

Figure no.	Figure Title	Page
Figure 1.1	Generic Cross Calibration Processing Sequence.	03
Figure 1.2	MSI Configuration, Full Instrument.	05
Figure 1.3	OLI Architecture.	07
Figure 2.1	Linear BRDF Model for Libya4 Based on Solar Zenith Angle.	15
Figure 2.2	Example of the Computed Surface Reflectance for a CAL, PARASOL, Starting from Surface Reflectance Measurements from an REF, MERIS, for the Libya4 Site.	16
Figure 2.3	1-1 Plot of Grid-Cell TOA Reflectances of MSI and OLI. Subplot at Lower Right Corner is for Cirrus Band.	18
Figure 2.4	Differences between OLI and MSI Response Before (open circle) and After (closed circle) Cross Calibration.	19
Figure 3.1	Flow Chart of Cross-Calibration Algorithm.	23
Figure 3.2	Example Spectral Signature and SBAF Representation.	25
Figure 3.3	TOA Reflectance Vs Spherical Coordinate Solar Angles.	28
Figure 3.4	TOA Reflectance Vs Cartesian Coordinate Converted Solar Angles.	28
Figure 3.5	One to One Regression Plot of SWIR2 Band TOA Reflectance.	30
Figure 4.1	Hyperion Scenes for Libya 4, (a) Before Filter Application, (b) After filter Application.	41
Figure 4.2	SBAF Distribution for Libya4 PICS for Different Bands.	42

Figure 4.3	Relative Spectral Response of OLI (Solid Line) and MSI (Dotted Line).	44
Figure 4.4	Before and After BRDF Corrected TOA Reflectance of OLI over Sudan1 Site.	46
Figure 4.5	Plot of different angles over Libya 1 Sentinel 2A (Red Marker), Landsat 8 (Green Marker).	48
Figure 4.6	Regression Line for the Cross Calibration of OLI and MSI.	50
Figure 4.7	Regression Line for the Cross Calibration of OLI and MSI Without Bias.	51
Figure 4.8	Distribution of SBAF After Simulation of SBAF Caused by Spectral Filter Shift.	54
Figure 4.9	The Distribution of SBAF Due to the Change of Bandwidth.	56
Figure 4.10	Distribution of TOA Reflectances from MSI Scene of Libya4 PICS, 03/09/2016.	58
Figure 4.11	Distribution of TOA Reflectances for Lake Tahoe MSI scene, 05/22/2016.	59
Figure 4.12	Hyperspectral Reference Surface Reflectance Profile.	62
Figure 4.13	MODTRAN Simulated TOA Reflectance over Libya4 PICS, 06/22/2017 (DOY 173).	62
Figure 4.14	MODTRAN Simulated TOA Reflectance over Libya4 PICS, 12/31/2017 (DOY 365).	62
Figure 4.15	Distribution of Simulated Mean TOA Reflectance, DOY 365.	64

Figure 4.16	Generated Random Aerosol Optical Depth at 550nm, (b) Generated Random Water Vapor.	66
Figure 4.17	Simulated Reflectance with Randomly Sampled Water Vapor and Aerosol Optical Depth at 550nm.	67
Figure 4.18	Boxplot of OLI and MSI Reflectance Before and After BRDF Correction, MSI After Applying Both set of Gain, Algodones Dunes.	70
Figure A.1	OLI, MSI and ROI position for Target Sites.	87
Figure A.2	Variation of Reflectance for Overpass Time Difference over Libya4 @DOY 173	88
Figure A.3	Variation of Reflectance for Overpass Time Difference over Libya4 @DOY 365	89
Figure A.4	Reflectance vs Spherical Coordinate Solar Angles	90
Figure A.5	Reflectance vs Cartesian Coordinate Converted Solar Angles.	91
Figure A.6	Reflectance vs Spherical Coordinate View Angles	92
Figure A.7	Reflectance vs Cartesian Coordinate Converted Solar Angles.	93

LIST OF TABLES

Table No.	Title	Page
Table 1.1	OLI/MSI Comparison.	7
Table 3.1	Misregistration and Corresponding Shift in Pixels for OLI and MSI.	35
Table 4.1	Scene Pairs Used for Cross Calibration.	40
Table 4.2	Mean Band-Specific SBAF and Standard deviation.	43
Table 4.3	Summary of the SBAF of All Target Sites.	43
Table 4.4	Percentage uncertainty in OLI TOA reflectance of Libya4 PICS data before and after BRDF correction.	45
Table 4.5	Sudan1 OLI TOA Reflectance's Before and After Four Angle BRDF Correction.	47
Table 4.6	Gain and Bias Statistics of Cross-Calibration Regression of MSI and OLI.	49
Table 4.7	Gain and Bias Statistics of Cross-Calibration Regression of MSI and OLI.	52
Table 4.8	Bandwise SBAF Uncertainty Due to Spectral Filter Center Wavelength Shift.	55
Table 4.9	Uncertainty Due to Change of Bandwidth Change of OLI and MSI.	56
Table 4.10	Uncertainty Due to Image Registration Error of Libya 4 and Lake Tahoe.	60
Table 4.11	Uncertainty Due to Spatial Resolution Mismatch.	60
Table 4.12	Uncertainty Due to Site Inhomogeneity.	61
Table 4.13	Highest Percent Difference on DOY 173 and DOY 365.	63

Table 4.14	Uncertainty in Simulated TOA Reflectance at DOY 173 and 365 over Libya4.	65
Table 4.15	Uncertainty Associated with Simulated TOA Reflectances.	68
Table 4.16	Summary of all the Uncertainties.	68
Table 4.17	Comparison of Statistical Test Results for Cross Calibration Gain Applied to MSI Reflectances.	72
Table 4.18	Sentinel 2A Different Processing Versions and Their Anomalies.	74
Table 5.1	Recommended Cross Calibration Gain and Bias and their uncertainty for Each Band.	79
Table A.1	UTM Values for ROI Corner Coordinates for Target Sites.	88

ABSTRACT

CROSS CALIBRATION AND VALIDATION OF LANDSAT 8 OLI AND SENTINEL

2A MSI

M M FARHAD

2018

This work describes a proposed radiometric cross calibration between the Landsat 8 Operational Land Imager (OLI) and Sentinel 2A Multispectral Instrument (MSI) sensors. The cross calibration procedure involves i) correction of the MSI data to account for spectral band differences with the OLI; and ii) correction of BRDF effects in the data from both sensors using a new model accounting for the view zenith/azimuth angles in addition to the solar zenith/view angles. Following application of the spectral and BRDF corrections, standard least-squares linear regression is used to determine the cross calibration gain and offset in each band. Uncertainties related to each step in the proposed process are determined, as is the overall uncertainty associated with the complete processing sequence. Validation of the proposed cross calibration gains and offsets is performed on image data acquired over the Algodones Dunes site.

In general, the estimated cross calibration offsets in all bands were small, on the order of 0.0075 or less in magnitude. The cross calibration gains generally varied less than 1.0% from unity; for the Blue and Red bands, the gains varied by approximately -2.5% and -1.4% from unity, respectively. For a forced zero offset, the estimated gain in all but the Blue band changed little; the Blue band gain varied by approximately 1.86% from unity. Consequently, cross calibration of the Blue band requires both the gain and nonzero offset.

To maintain processing consistency, it is recommended to use the gain and (nonzero) offset in all bands.

Overall, the net uncertainty in the proposed process was estimated to be on the order of 6.76%, with the largest uncertainty component due to each sensor's calibration uncertainty, on the order of 5% and 3% for the MSI and OLI, respectively. Other significant contributions to the uncertainty include: seasonal changes in solar zenith and azimuth angles, on the order of 2.27%; target site non-uniformity, on the order of 1.8%; variability in atmospheric water vapor and/or aerosol concentration, on the order of 1.29%; and potential shifts in each sensor's spectral filter central wavelength and/or bandwidth, on the order of 0.82% and 0.28%, respectively.

Chapter 1 Introduction

When an Earth-orbiting satellite sensor is launched, a primary concern is to ensure the quality and accuracy of its image data throughout its operating lifetime [1]. This requires regular monitoring of the sensor's radiometric and geometric performance and adjusting the relevant operating parameters as needed to maintain data accuracy and quality. In terms of radiometric performance, these parameters are the band-averaged gains and offsets that convert the image data from DNs to radiance or reflectance values. The measured values are compared to a known, accepted standard in a process known as *absolute radiometric calibration*. Other radiometric parameters of interest include the relative gains and offsets of the sensor's detectors; these parameters are determined through a process of *relative radiometric calibration*, and are used to remove 'striping' and/or 'banding' artifacts due to differences in detector response.

Absolute radiometric calibration of a sensor prior to satellite launch determines the initial operating gains and offsets. Due to launch-related stresses and aging of components in the space environment [2], the sensor response can degrade over time such that the initial gains and offsets may no longer be valid. Subsequent radiometric calibrations are typically performed after launch to monitor the sensor response and adjust the gains/offsets accordingly.

Post-launch calibration can use a variety of "reference" measurements. Measurements of on-board calibration sources such as a solar diffuser panel or black body can be used if they are available. *In-situ* measurements of surface radiance or reflectance at a calibration site on the Earth's surface can also be used if the required set of measurements exists. Another source can be measurements from a well-calibrated sensor imaging a calibration

site on a regular basis; the calibration can be “transferred” from the source sensor to an (uncalibrated) sensor of interest through a process of *cross calibration*. This calibration method has the advantage of not relying on an onboard calibration system, which simplifies the sensor design and reduces its overall cost, and it does not rely on *in-situ* surface measurements of sites that are inaccessible due to physical remoteness or local/regional political instability. In general, cross-calibration offers a quick, highly repeatable, and inexpensive way to perform reliable radiometric calibration of satellite sensors [3].

This thesis proposes a technique to perform reflectance-based cross calibration between the Landsat 8 Operational Land Imager (OLI) and Sentinel 2A Multispectral Instrument (MSI) sensors, using co-incident pairs of OLI and MSI images acquired over four North African Pseudo-Invariant Calibration Sites (PICS) which are Libya 4, Libya 1, Niger 2 and Sudan 1. This work also includes some dark targets to incorporate a wide range of TOA reflectance value, which are Lake Tahoe and Volcanic site near Libya. Due to the unavailability of coincident pairs, some near coincident pairs which are within 3 days have been used for the Volcanic site near Libya. The work described in this thesis contributes to the ongoing process of “harmonizing” image data from current and future sensors such as the MSI with legacy Landsat image data.

1.1 Cross Calibration

As mentioned earlier, the cross-calibration method transfers the calibration from a well-calibrated “reference” sensor to an uncalibrated sensor of interest, as shown in Figure 1.1. While any site imaged by both sensors could in principle be used, PICS [4] are considered desirable due to their observed temporal, spatial, and spectral stability. The only requirement to enable cross calibration is that both sensors simultaneously (or near-

simultaneously) image the site, in order to minimize effects from changing atmospheric characteristics.

Cross calibration assumes that both sensors are measuring the same radiances or reflectances. In practice this assumption is seldom valid, as the relative spectral responses (RSRs) of the two sensors are not equal. Any cross calibration technique should take this into account by applying band-dependent scaling factors to the uncalibrated sensor data in order to spectrally “match” the calibrated sensor data. A method to derive and apply these factors is described in Chapter 3.

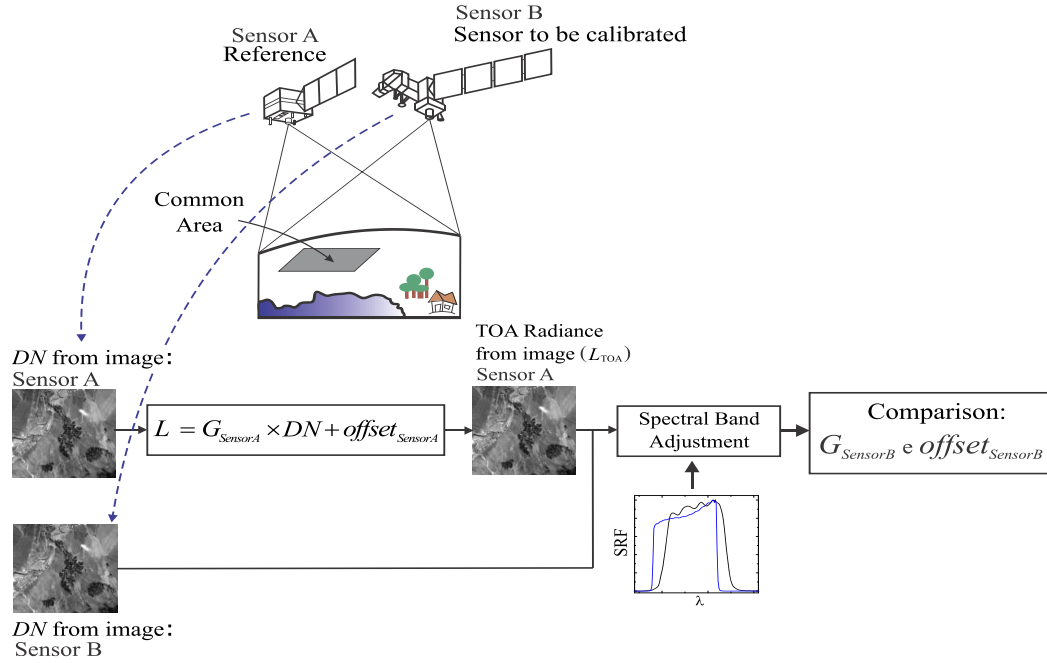


Figure 1.1 Generic Cross Calibration Processing Sequence [5].

Cross calibration can be either radiance-based or reflectance-based. The following equations are used:

$$L_{CAL} = G_L * L_{REF} + B_L \quad (1a)$$

$$\rho_{CAL} = G_\rho * \rho_{REF} + B_\rho \quad (1b)$$

where $G_L(G_p)$ is the radiance(reflectance) gain, $B_L(B_p)$ is the radiance(reflectance) offset, and $L_{REF}(\rho_{REF})$ and $L_{CAL}(\rho_{CAL})$ are the reference and calibrated radiance(reflectance).

1.2 Comparison of MSI and OLI Radiometric Performance

1.2.1 Sentinel 2A

The Sentinel 2 mission is part of the European Space Agency's (ESA) Copernicus program [6]. Sentinel 2A offers coverage of the Earth's land and coastal areas at spatial, spectral and radiometric resolutions comparable to those provided by the Landsat 8 mission, with a revisit time of 10 days. The revisit time reduces to 5 days with both satellites in the Sentinel 2 series (Sentinel 2A and 2B) operational.

Sentinel 2A was launched on June 23, 2015, and Sentinel 2B was launched on March 7, 2017. Both satellites fly at a mean altitude of approximately 786 km in nearly polar, sun synchronous orbits phased 180° apart. The equatorial crossing of their descending nodes occurs at approximately 10:30 AM Mean Local Solar Time (MLST). The imaged path covers a latitude range between 83° N and 56° S. (Sections 1.5.1 and 1.5.2, Sentinel-2 Users Handbook [7]).

Multi Spectral Instrument (MSI)

The MSI (Figure 1.2), a push broom sensor, is the sole payload onboard Sentinel 2A. The main telescope, a set of three anastigmatic mirrors, directs incident radiation onto two focal planes, separated by a dichroic beam splitter [7], that image the Visible/Near Infrared (VNIR) and Short-wave Infrared (SWIR) portions of the electromagnetic spectrum. The VNIR focal plane consists of a monolithic CMOS module containing 12 detectors, while

the SWIR focal plane consists of a CMOS read-out circuit containing 12 HgCdTe detectors passively cooled to temperatures less than 195° K. The focal plane detectors are staggered such that the resulting cross-track field-of-view (FOV) is approximately 20.6°, corresponding to a swath width of approximately 290 km.

The spatial resolution of MSI image data varies by band. The visible bands and primary NIR band (B2, B3, B4, and B8) are imaged at 10 m resolution. Three “Red Edge” bands, a second NIR band, and two SWIR bands (B5, B6, B7, B8a, B11, and B12) are imaged at 20 m resolution. Finally, three “atmospheric” bands (B1, B9, and B10) are imaged at 60 m resolution [8]. The MSI images data with 12-bit radiometric resolution (0-4095 DN). The overall calibration accuracy achieved to date is better than 5%, with efforts underway for improvement to better than 3% [6].

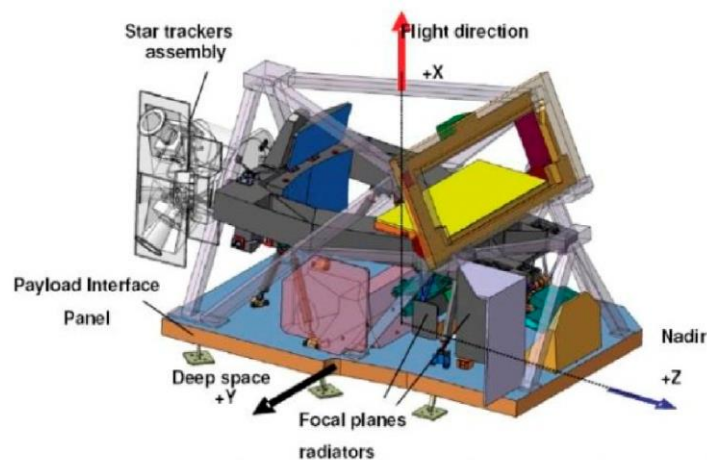


Figure 1.2 MSI Configuration, Full Instrument [7].

1.2.2 Landsat 8

Landsat 8, launched on February 11, 2013, is the latest in a series of satellites that are part of the Landsat mission, which has provided continuous global imaging of the Earth's

surface since its beginning in 1972. It flies at a nominal mean altitude of approximately 705 km in a nearly polar, sun synchronous orbit that follows the Worldwide Reference System (WRS-2), with a revisit time of 16 days. The equatorial crossing of the descending node occurs at approximately 10:11 AM MLST. The imaged orbital path covers a latitude range between approximately 80° N and 80° S [9]. Unlike the previous Landsat satellites, Landsat 8 can maneuver to allow its sensors to acquire off-nadir imaging. It can also maneuver to allow imaging of the Moon.

Operational Land Imager (OLI)

The OLI (Figure 1.3) is one of two sensors comprising the Landsat 8 payload, the other being the Thermal Infrared Sensor (TIRS). It is a push broom sensor, based on advanced concepts and technologies developed for the Earth Observing 1 Advanced Land Imager (EO-1 ALI) [10]. These advances allow significantly improved radiometric performance over the Landsat 7 Enhanced Thematic Mapper Plus (ETM+) while maintaining overall data continuity with the existing Landsat archive.

The OLI's main telescope consists of four anastigmatic mirrors, which direct incident radiation to a focal plane containing 14 modules imaging the VNIR and SWIR portions of the electromagnetic spectrum. These modules are staggered so that the cross-track FOV is approximately 15°, corresponding to a swath width of approximately 185 km. Each module contains 494 detectors for the multispectral bands (Si PIN for the VNIR bands, HgCdTe for the SWIR bands), and 988 detectors for the panchromatic band (Si PIN) [11]. The entire focal plane is cooled to temperatures less than 200° K. Unlike ETM+, OLI does

not have a thermal band—TIRS provides thermal band imaging in a spectral range similar to ETM+ but split into two bands.

OLI's spatial resolution is consistent with that of ETM+. All multispectral bands acquire data with 30 m resolution, while the panchromatic band acquires data with 15 m resolution, as shown in Table 1.3. For thermal band imaging, the ETM+ acquires data at 60 m resolution, while TIRS acquires data at 100 m resolution. OLI initially acquires data with 14-bit radiometric resolution; the final image data, however, are quantized to the 12 least significant bits, resulting in a radiometric resolution equal to MSI and significantly greater than the 8-bit radiometric resolution in ETM+.

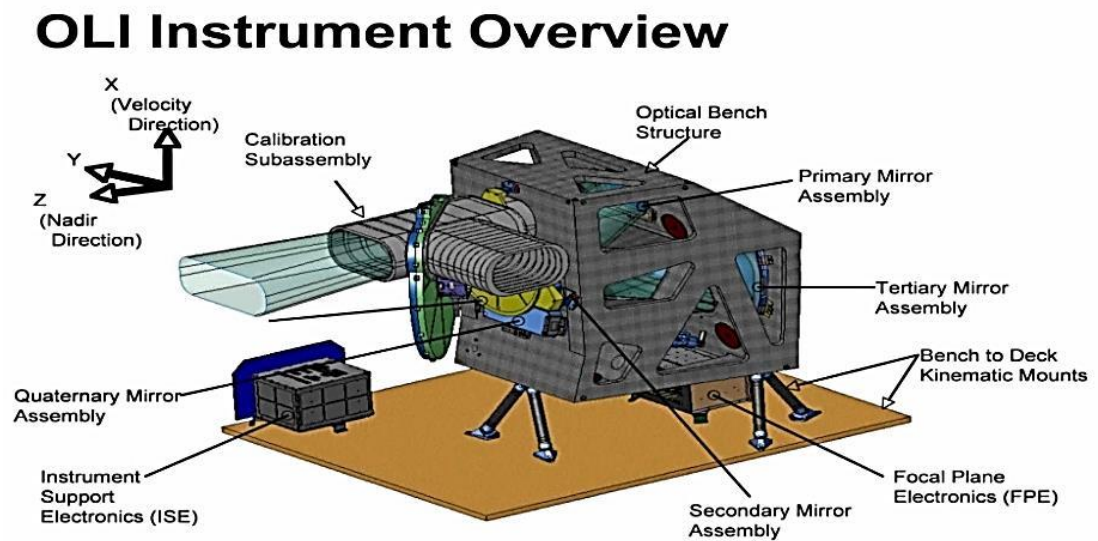


Figure 1.3 OLI Architecture [10].

1.2.3 Side-by-Side Comparison

Table 1.1 provides a summary comparison between the corresponding OLI and MSI bands used in this cross calibration work. MSI bandpasses cover the same spectral regions as OLI

bandpasses, they are generally wider in shape. Note the overlap of MSI Coastal/Aerosol and Blue bandpasses.

Band	Bandpass (nm)		Spatial Resolution (m)		SNR	
	OLI	MSI	OLI	MSI	OLI	MSI
C/A	433-453	397.3-487.3	30	60	238	129
Blue	450-515	394.1-590.1	30	10	364	154
Green	525-600	515.0-605.0	30	10	302	168
Red	630-680	626.5-702.6	30	10	227	142
NIR	845-885	831.8-897.8 (8A)	30	20	204	72
SWIR1	1560-1660	1470.7-1756.7	30	20	265	100
SWIR2	2100-2300	1960.4-2442.4	30	20	334	100

Table 1.1 OLI/MSI Comparison [11], [12].

1.3 Summary

This chapter has provided an introductory background to the work described in this thesis. It has defined the term “cross calibration” as it relates to this thesis, and has provided background information regarding the two sensors emphasized in this work. The next chapter will review previous cross calibration efforts of these sensors.

The contents of this thesis are presented as follows. Chapter 1 introduces the topic and provides a summary comparison of OLI and MSI radiometric performance. Chapter 2 briefly reviews previous cross calibration efforts in general, and previous OLI-MSI cross calibration in particular. Chapter 3 presents the steps used in performing the proposed cross calibration in greater detail. Chapter 4 reviews the results obtained from the proposed technique. Finally, Chapter 5 summarizes the thesis work and offers potential directions for future research and development of the proposed technique.

Chapter 2 Literature Review

Many techniques have been developed to perform cross calibration between satellite sensors, including efforts to calibrate all of the Landsat sensors to the OLI [13]. Research has focused on selection of ‘invariant’ calibration sites, methods to adjust for differences in spectral response between sensors, and methods to model and correct for BRDF and other effects due to differences in viewing geometry and illumination. This chapter provides a summary review of the literature describing this research, and briefly compares previous methods to the proposed technique described in Chapter 3.

2.1 Calibration Site Selection

A critical factor in producing a successful cross calibration involves selection of a calibration site regularly imaged by the sensors of interest. The site should be as temporally, spatially, and spectrally invariant as possible, in order to more easily distinguish between potential changes to a sensor’s radiometric response and potential changes to the site’s surface and/or atmospheric characteristics. Historically, these sites have been in desert regions exhibiting a high degree of uniform surface reflectance, with minimal rainfall and cloud cover, and minimal signs of human settlement or other activities [14].

2.1.1 Saharan and Arabian Desert Sites

The earliest PICS used for cross calibration were identified in areas throughout the Sahara Desert in North Africa and the deserts of Saudi Arabia. Rao and Chen (1995) used image

data acquired over the southeastern portion of the Libyan desert to i) identify rates of response degradation in the visible and NIR channels of the NOAA Advanced Very High Resolution Radiometer (AVHRR); and ii) to establish “inter-satellite calibration linkages” between the NOAA 7 and 9 AVHRRs and the NOAA 9 and 11 AVHRRs [15]. Their analysis emphasized VNIR and thermal image data acquired at satellite zenith angles of 14° or less and solar zenith angles of 60° or less to minimize BRDF and atmospheric effects. They validated their analysis results using image data acquired over the White Sands area in New Mexico. Although they derived models to account for intra-sensor response degradation and overall cross calibration between pairs of AVHRR sensors, no estimate for the uncertainties involved in their approach was presented; such results were apparently intended to be provided in subsequent journal papers.

Cosnefey, *et al* (1996) analyzed 20 desert sites in North Africa and Saudi Arabia [16] for use in calibration of sensors employing charge-coupled device detectors (e.g. the ADEOS POLDER, SPOT-4 Vegetation, EOS MISR, Envisat MERIS, etc). 100 km x 100 km regions representing the sites were extracted from cloud-free Meteosat-4 image data in order to determine their spatial uniformity. Overall, the estimated spatial variability for these sites was within 3%, while the estimated temporal variability was within 2%. They concluded that these sites could be used for future satellite calibration. Many of these sites are considered among the most temporally stable of calibration sites, and are used for calibration purposes.

2.1.2 CEOS Recommended PICS and Calibration

Using image data from the Landsat 7 ETM+ and EO-1 Advanced Land Imager (ALI) sensors, Chander, *et al* (2010) identified the following metrics indicating the usefulness of a PICS for calibration [17]:

- Useable Area
- Data Availability
- TOA Reflectance
- Spatial Uniformity
- Spectral Stability

They assessed six candidate sites (Mauritania¹, Mauritania², Algeria³, Libya¹, Libya⁴, and Libya⁵) using the above metrics. The results of their assessment indicate these metrics can reliably be used in PICS selection. The Committee on Earth Observation Sciences (CEOS) has since adopted them as calibration sites.

These analysis of PICS have been done to pick the appropriate PICS for this cross calibration work. Among the twenty CEOS PICS, four of them are considered in this work, as they have been used in previous calibration work by the Image Processing Laboratory [18]. These PICS are:

- Libya 1
- Libya 4
- Niger 2
- Sudan 1

2.2 SBAF in Cross Calibration

Two sensors imaging the same region on the Earth will measure different surface radiances and reflectances. A significant reason for this difference is due to inherent differences in their spectral responses. Correction factors applied to the uncalibrated sensor's image data, called Spectral Band Adjustment Factors (SBAFs), can result in greater equalization of its data to the corresponding image data from the calibrated sensor. Research into the determination of SBAFs and their effects on cross calibration has been performed. A summary of this research is presented in this section.

Teillet, *et al* (2004) considered the effects of spectral band differences on cross calibration [19]. Their analysis used radiometrically and geometrically corrected image data of the Railroad Valley Playa (RRV) acquired by the ETM+, ALI, and Terra MODIS, ASTER, and MISR sensors, as their overpass times were within 45 minutes of each other; no BRDF or other corrections were applied to the data. Standard radiative transfer codes were used to calculate SBAFs for selected regions in the playa, the inputs to the codes consisting of each region's surface reflectance spectra. The results of their analysis indicated that with SBAF correction, the calibration accuracy was within 3%. Based on this analysis, they recommended, in general, that SBAFs be used when cross calibrating between sensors.

Chander, *et al* (2010) used an average of 108 EO-1 Hyperion hyperspectral profiles of the Libya4 PICS, acquired from 2004 to 2009, to determine an SBAF for Terra MODIS, using the ETM+ as the calibrated reference sensor [20]. The SBAF was calculated by integrating the product of the sensor relative spectral response (RSR) and the Hyperion TOA reflectance, then dividing by the integrated sensor RSR, as shown in Eq. (1):

$$SBAF = \frac{\rho_{\lambda, (ETM+)}}{\rho_{\lambda, (MODIS)}} = \frac{\frac{\int \rho_{\lambda} \cdot RSR_{\lambda, (ETM+)} d\lambda}{\int RSR_{\lambda, (ETM+)} d\lambda}}{\frac{\int \rho_{\lambda} \cdot RSR_{\lambda, (MODIS)} d\lambda}{\int RSR_{\lambda, (MODIS)} d\lambda}} \quad (1)$$

where

$\rho_{\lambda, (ETM+)}$ = Spectrally banded TOA reflectance of ETM+ (Unitless)

$\rho_{\lambda, (MODIS)}$ = Spectrally banded TOA reflectance of MODIS (Unitless)

ρ_{λ} = Hyperspectral TOA reflectance profile of the target (Unitless)

RSR_{λ} = Relative spectral response of the sensor

Without SBAF correction, the observed Terra MODIS TOA reflectance was at least 16% greater than the corresponding ETM+ TOA reflectance in all bands. With SBAF correction, the difference was reduced to 6% or less. Greater uncertainties were found in the Blue, NIR, and SWIR1 bands.

In 2013, Chander, *et al* looked at the effect of SBAF correction derived from different hyperspectral data sources on the cross calibration of ETM+ and Terra MODIS using the Libya4 PICS as their test site [21]. Specifically, they considered Hyperion and SCIAMACHY hyperspectral data. The Hyperion-based SBAF correction resulted in reflectance differences of approximately -5.51%, 2.04%, -0.83% and 4.06% in the Blue, Green, Red, and NIR bands, respectively. The differences were even lower when SCIAMACHY-based SBAF correction was used (-0.62%, 3.26%, 0.09%, and 0.93%, respectively). Overall, using the SCIAMACHY-based SBAFs tended to produce a more consistent cross calibration.

2.3 BRDF Correction

When cross calibrating between sensors, it is highly desirable for them to image a region under similar viewing geometry and solar illumination conditions. Solar illumination and potential atmospheric effects can be accounted for if the sensors simultaneously (or near-simultaneously) image the region. Due to differences in sensor design and operation, and depending on the imaged surface, differences in viewing geometry will likely result in the introduction of bi-directional reflectance distribution function (BRDF) effects. Research into the BRDF issue has resulted in a variety of models and correction approaches. This section briefly summarizes this research and its application in the cross calibration process. Liu, *et al* (2004) used a BRDF model based on the solar zenith angle in their cross calibration between Terra MODIS and MVIRS [22], using images acquired over the Dunhuang site in China. Their model extended the model originally developed by Roujean *et al* (1992) [23], allowing consideration of solar zenith angles greater than 51° . Li's model successfully accounted for the BRDF of AVHRR bands corresponding to selected MVIRS bands over terrestrial surfaces. The estimated error due to BRDF effects was found to be approximately 2% to 3%.

Schlapfer, *et al* (2014) proposed a novel correction method for wide field-of-view (FOV) optical scanners based on the solar zenith, view zenith, and relative azimuth angles (i.e. the difference between the solar and view azimuth angles) [24]. Their method requires the image dataset to contain at least four distinct bands. It corrects surface cover-dependent BRDF effects using observed surface reflectances to “tune” the standard Ross-Thick and Li-Sparse BRDF models. The resulting “calibrated” model is then used to correct the angle-dependent reflectance behavior. The correction algorithm was tested on non SBAF-

corrected multispectral and airborne hyperspectral image data of areas with and without surface vegetation. No specific values regarding the amount of correction were given; they asserted that the correction resulted in stable reflectances across all viewing angles.

Mishra, *et al* (2014) derived an empirical BRDF model based on the solar zenith and view zenith angles of Terra MODIS near-nadir images acquired over the Libya4 PICS [25]. Scene-center TOA reflectances from approximately 160 lifetime observations were plotted as a function of solar zenith angle for all reflective bands. As an initial “guess” for the model form, a simple linear model was fit to the data. Figure 2.1 shows the resulting model for the NIR band (band 2).

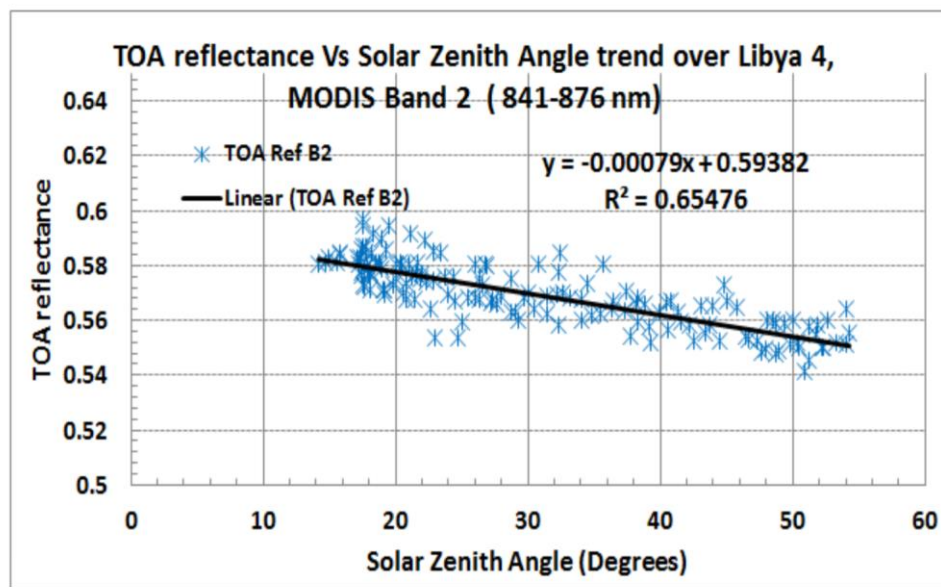


Figure 2.1 Linear BRDF Model for Libya4 Based on Solar Zenith Angle.

Their final model was implemented using a linear function of solar zenith angle and a quadratic function of view zenith angle. They found that reflectance decreased due to BRDF effects, with greater decrease at longer wavelengths; consequently, the SWIR bands were found to be most affected. The slope coefficient of model based on linear solar zenith angle based model shows an exponential decrement throughout all the wavelength. In

addition, reflectances were modeled solely as a quadratic function of view zenith angle. They proposed a vicarious calibration model which basically calculates the reflectance measured by the sensor un-biasing the BRDF effects. They compared the difference between the model vs. measured TOA reflectance which are within 3% or better for all the bands.

2.4 Cross Calibration

Following application of SBAF and BRDF corrections, the sensors' measured TOA reflectances can be compared more directly. As mentioned earlier, simultaneous (or near simultaneous) images are acquired by the sensors in order to minimize atmospheric effects. The TOA reflectances of the uncalibrated sensor are typically modeled as a linear function of the calibrated sensor's reflectances. Ideally, the plotted data lie directly on a one-to-one line, meaning that the measured reflectances from the sensors are equal. In practice, however, some residual deviation is typically observed, which represents a gain and/or offset in the uncalibrated sensor. This section briefly reviews various cross calibration results.

Lacherade, *et al* (2013) proposed a cross calibration technique using processed MERIS and PARASOL image data acquired over the set of 20 CEOS desert sites and retrieved from the French remote sensing database SADE [26]. Instead of applying SBAF correction to the uncalibrated sensor data, the uncalibrated sensor's surface reflectances were derived from interpolated and sampled TOA reflectances of the calibrated reference sensor, as shown in Figure 2.2.

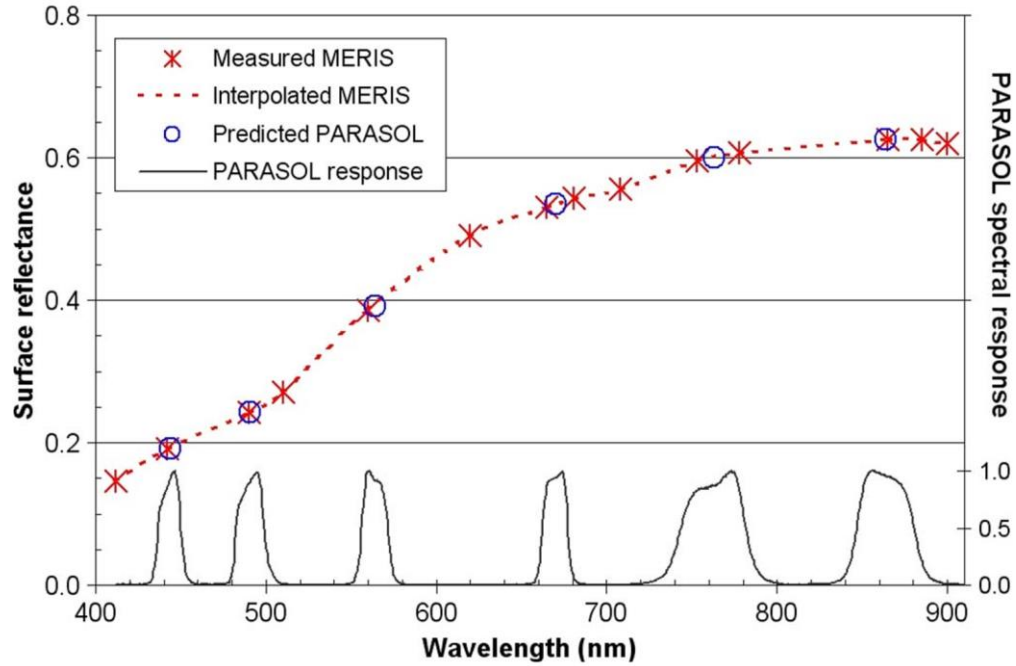


Figure 2 Example of the Computed Surface Reflectance for a CAL, PARASOL, Starting from Surface Reflectance Measurements from an REF, MERIS, for the Libya4 Site.

They tested the proposed approach on non BRDF-corrected image data acquired over the CEOS Saharan desert sites, and found an approximate 2% difference in the Red and NIR bands. Differences of approximately 4% to 6% were observed in the Green and Blue bands, respectively.

Mishra, *et al* (2014) presented radiance- and reflectance-based cross calibration of Landsat 8 Operational Land Imager (OLI) and ETM+ [27]. Two independent datasets were used in the analysis:

- Simultaneous image pairs acquired at two Saharan desert locations during a two-day underfly event on March 29-30, 2013. One location was near the Libya4 PICS (WRS2 path 182, rows 42-43); the other was over WRS2 path 198 rows 38-39.

- Time series analysis of images acquired over the Libya4 PICS

Results using both datasets indicate a cross-calibration uncertainty to within 2.5% in all bands but NIR, which had an uncertainty of 4% in both approaches. The NIR band results are most likely due to differences in each sensor's RSR--the OLI RSR is narrower, resulting in exclusion of a significant absorption feature affecting the ETM+ NIR band. Even with the difference in NIR band RSRs, the results were within the required 3% uncertainty for OLI and 5% uncertainty for ETM+.

Li, *et al* (2017) presented a method to cross calibrate the Sentinel 2A MSI and OLI sensors [28]. Using OLI as the calibrated sensor, they used Simultaneous Nadir Overpass (SNO) scenes acquired just east of the CEOS Algeria3 site. Their analysis included SBAF correction but no BRDF correction. Their results are shown in Figure 2.3.

Application of the relevant SBAFs resulted in agreement to within 3% in six of the eight corresponding bands. Overall, the MSI Blue band appeared to be the best calibrated, to approximately 0.08%.

Calibration differences on the order of 0.4% were obtained for Green, Red, and NIR bands; are slightly higher in the Coastal Aerosol, Blue, Red, and SWIR1 bands, approximately equal in Green band, slightly lower in SWIR2 band, and significantly lower in NIR and Cirrus bands.

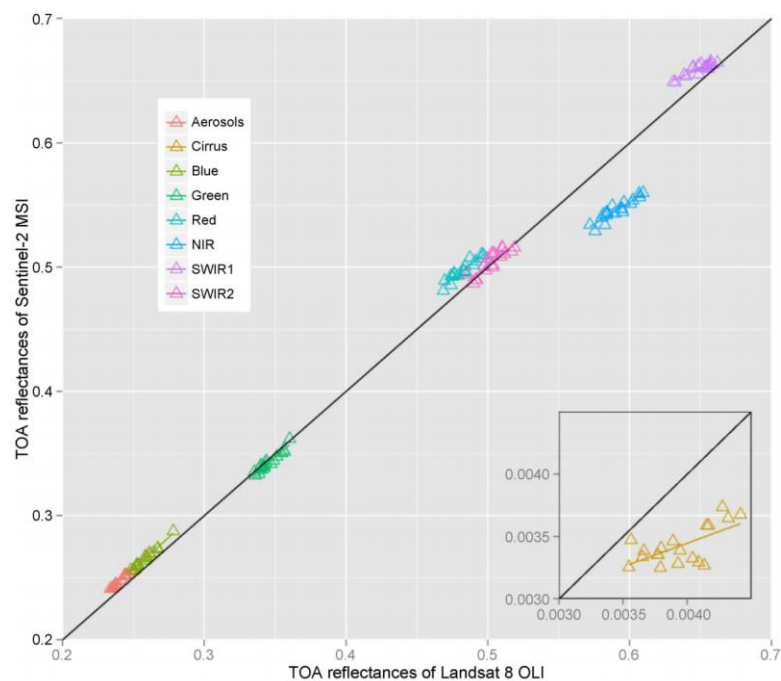


Figure 2.3 1-1 Plot of Grid-Cell TOA Reflectances of MSI and OLI. Subplot at Lower Right Corner is for Cirrus Band [28].

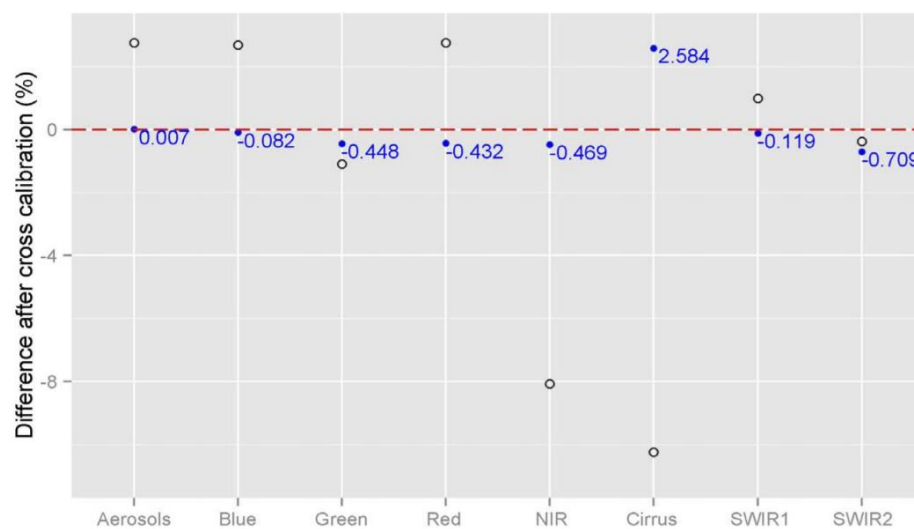


Figure 2.4. Differences between OLI and MSI Response Before (open circle) and After (closed circle) Cross Calibration [28].

Figure 2.4 shows the resulting improvement after applying the derived cross calibration gains to the MSI data. All bands except the Cirrus band improved the agreement to within 1%; the Cirrus band agreement improved to approximately 2.5%.

2.5 Uncertainty of Cross Calibration

As with other computations and measurements, each step in the cross calibration process introduces a degree of uncertainty to the final result. The sources of uncertainty at each step can be identified, and their relative contribution to the final uncertainty can be determined. This section briefly considers uncertainty related to cross calibration.

2.5.1 Uncertainty in SBAF

Chander, *et al* (2013) determined the inherent uncertainty in cross calibration due to the SBAF [29]. Their SBAFs were generated from Monte Carlo simulation of Hyperion and SCIAMACHY image data of the Libya4 PICS. Table 1 shows the estimated uncertainties in the SBAFs for each corresponding band. Assuming 10 nm spectral resolution for each band, the associated uncertainty SBAF uncertainties were approximately 0.05% for Blue and Green bands, approximately 0.04% for Red band, and approximately 0.21% for NIR band.

Pinto, *et al* (2016) derived SBAFs for the OLI and CBERS 4 Multispectral Camera, based on the corresponding Hyperion image data of the Algodones Dunes and Libya4 PICS, using Monte Carlo simulations [30]. The simulation dataset was arbitrarily sampled to generate possible SBAF values, and from the sampled values the associated uncertainties

were estimated. Their results indicated that the degree of uncertainty is dependent on the degree of correlation of the Hyperion reflectance and RSR of both sensors. Assuming maximum correlation, the uncertainty was as low as 0.0% in the Green band for Libya 4, and as high as 0.87% in the NIR band for Algodones Dunes. Similarly, assuming minimum correlation, the uncertainty was as low as 0.48% in the Red band for Libya4, and as high as 1.37% in the NIR band for Algodones Dunes.

2.5.2 Other Sources of Uncertainty

In addition to estimating the SBAF uncertainty, [29] considered uncertainties due to differences in spectral resolution, spectral filter shift, geometric misregistration, and differences in spatial resolution. The spectral uncertainty was estimated from the available Hyperion and SCIAMACHY image data. The uncertainty due to spectral filter shift was estimated to be less than 2.5% in all bands, with the Blue and Green bands exhibiting the largest uncertainties. With respect to spatial misregistration, the estimated uncertainty was less than 0.35% in all bands. Finally, with respect to spatial resolution, the estimated uncertainty was on the order of 0.1% for all bands.

In a rigorous analysis using Monte Carlo and MODTRAN simulations, Gorrone, *et al* (2017) considered different sources of spectral, spatial, and temporal uncertainties affecting cross calibration of the Sentinel 2A MSI [31]. Their reference data source was hyperspectral data simulated for the upcoming Traceable Radiometry Underpinning Terrestrial and Helio Studies (TRUTHS) sensor. Their sites focused on the La Crau, Ascension Island, and Libya4 CEOS sites, representing grassland, oceanic, and desert

landcover types, respectively; they also simulated snow cover. They estimated an overall uncertainty, for an individual MSI overpass, of approximately 0.4% to 0.5% in the “best” bands (i.e. VNIR) and approximately 0.4% to 0.7% in the “worst” bands (i.e. SWIR2). Averaging over multiple overpasses of a site, they estimated an overall uncertainty on the order of 0.2% for the “best” bands and approximately 0.3% to 0.7% for the “worst” bands. These estimates took into account both SBAF and BRDF correction.

2.6 Summary

This chapter has briefly reviewed research relating to the steps used to perform cross calibration between two sensors, and in determining associated uncertainties in some of those steps. The issues that seem to most directly impact the reviewed cross calibration work are differences in spectral response between the sensors and BRDF effects at a given site due to differences in viewing and solar geometry.

With the exception of Teillet *et al*, the reviewed cross calibration approaches tend to use SBAFs to account for sensor RSR differences; this thesis work uses SBAF correction as well, and will be considered in greater detail in Chapter 3. No cross calibration approach reviewed has used a BRDF model based on the full set of solar and view angles (i.e. solar zenith/azimuth and view zenith/azimuth). The cross calibration described in this thesis uses such a model, and will be described in greater detail in Chapter 3. In addition, a comprehensive uncertainty analysis on the steps required for this cross calibration will be performed, and will be described in Chapters 3 and 4.

In the context of cross calibration between the Sentinel 2A MSI and the OLI, there has been a subsequent update, effective December 2017, to the MSI’s Coastal Aerosol and

Blue band RSRs. This update effectively renders previous cross calibration in these bands invalid. The cross calibration derived for this thesis uses the corrected RSRs for these bands.

Chapter 3 Methodology

Overview

A typical cross calibration analysis can be represented by the following steps. It is assumed the cross calibration affects two sensors – the calibrated “reference” sensor, and the uncalibrated “target” sensor. The process flow described here can be extended to more than three sensors.

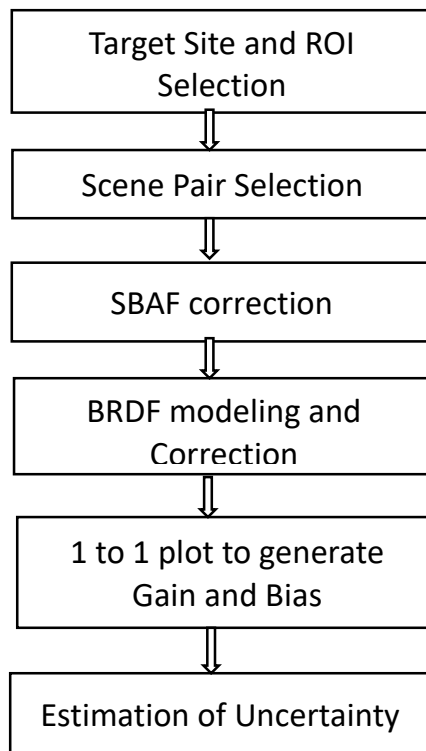


Fig 3.1 Flow Chart of Cross-Calibration Algorithm.

The flow chart shown in Fig 3.1 shows the steps of the algorithm, which is described below-

- Select appropriate region(s) of interest in one or more target sites.
- Select scene pairs of the target site(s) acquired by the reference and target sensors that are as nearly co-incident in time as possible.

- Correct the scene data for differences in spectral response.
- Correct the scene data for differences in solar and viewing geometry.
- Model the TOA radiance (reflectance) of the target sensor's scene data as a linear function of the TOA radiance (reflectance) of the reference sensor's scene data. This will result in a set of gains and offsets to apply to the target sensor's data such that it will be comparable to the reference sensor's data.
- Estimate the overall uncertainty in the estimated gains and offsets.

For the purposes of this thesis, the cross calibration is a TOA reflectance-based calibration of the Sentinel 2A MSI (target sensor) to the OLI (reference sensor). Additional details describing each of the above steps is provided in the following sections.

3.1 Select Appropriate Region(s) of Interest

The first step in cross calibration consists of selecting appropriate region(s) of interest from a target site. For the purposes of this thesis work, candidate target sites are those possessing up to 3% temporal and spatial scene uncertainty in all bands. To allow better characterization across each sensor's dynamic range, 'bright' and 'dark' target sites were considered. The bright targets consisted of rectangular regions of interest from the four Saharan desert PICS listed in Section 2.1.2 in Chapter 2. The dark targets were rectangular regions of interest taken from image data of Lake Tahoe (WRS2 path 43, row 33) and a volcanic site near the Libya1 PICS (WRS2 path 184, row 043). The regions of interest were chosen sufficiently large enough (> 30 km) to minimize errors relating to image misregistration.

3.2 Scene pair selection

Once the appropriate target sites and regions of interest are selected, the corresponding scenes are selected. Both sensors had to acquire the scene on the same date (a “co-incident” pair), with both overpasses occurring within 30 minutes of each other, in order to minimize atmospheric effects; given Landsat 8’s revisit time of 16 days and Sentinel 2A’s revisit time of 10 days, opportunities for same-day acquisition by both sensors occur approximately every 80 days. Both scenes in a given pair also had to have an estimated cloud cover of 10% or less.

3.3 SBAF Calculation and Correction

As mentioned in the Introduction chapter, differences in sensor RSR will generally result in differences in measured radiances and/or reflectances. These differences can be large enough to induce a significant error in the final cross calibration result; consequently, these differences should be accounted for [32]. As described in [33], SBAFs relating the MSI spectral response to the OLI spectral response are calculated and applied to the MSI data. For each scene date, the mean

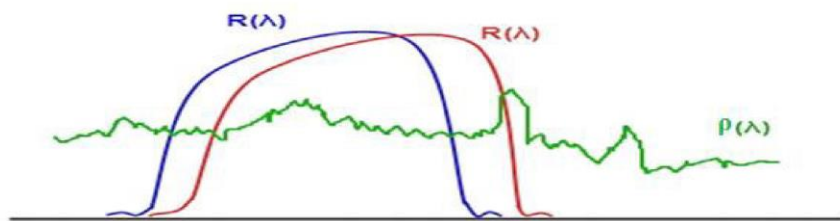


Figure 3.2 Example Spectral Signature and SBAF Representation [34].

hyperspectral reflectance profile of the target ROI is generated from the corresponding cloud-free Hyperion image data. The in-band reflectance for each sensor is calculated by integrating the portion of the hyperspectral profile (green line in Figure 3.2) contained within the sensor RSR bandwidth (red and blue curves in Figure 3.2), then dividing that value by the integral of the sensor RSR. The SBAF for the target is the ratio of the reference sensor in-band reflectance to the uncalibrated sensor's in-band reflectance:

$$\begin{aligned}
 SBAF &= \frac{\rho_{\lambda,(\text{OLI})}}{\rho_{\lambda,(\text{MSI})}} \\
 &= \frac{\frac{\int \rho_{\lambda} \cdot RSR_{\lambda,(\text{OLI})} d\lambda}{\int RSR_{\lambda,(\text{OLI})} d\lambda}}{\frac{\int \rho_{\lambda} \cdot RSR_{\lambda,(\text{MSI})} d\lambda}{\int RSR_{\lambda,(\text{MSI})} d\lambda}} \quad (1)
 \end{aligned}$$

where

$\rho_{\lambda,(\text{MSI})}$ = in-band TOA reflectance of OLI (Unitless)

$\rho_{\lambda,(\text{OLI})}$ = in-band TOA reflectance of OLI (Unitless)

ρ_{λ} = hyperspectral TOA reflectance profile of the target (Unitless)

RSR_{λ} = sensor relative spectral response

The individual SBAFs for each target ROI are then averaged to obtain an overall set of SBAFs. The relative spectral response functions for both sensors are given in Chapter 4, Section 4.2.

3.4 BRDF Modeling and Correction

When two sensors image a given target at different times, differences in their measured radiances and/or reflectances will occur due to i) changes in the solar zenith and azimuth angles between the sensor overpasses; and ii) differences in their view zenith and azimuth angles. As indicated in Chapter 2, previous cross calibration efforts have typically focused primarily on the solar zenith angle when deriving a BRDF correction. A rigorous treatment of BRDF effects should account for both solar zenith/azimuth and sensor view zenith/azimuth angles, as well as wavelength and surface cover type. This section describes a four angle, site-specific BRDF model derived for each band, where the wavelength component of BRDF is considered minimal.

From the set of solar zenith/azimuth and view zenith/azimuth angles in the spherical coordinate system (designated here as SZA, SAA, VZA, VAA), a new set of variables (x_1 , y_1 , x_2 , y_2) are generated through conversion of the angles to plane rectangular coordinates.

$$x_1 = \sin(SZA) * \cos(SAA) \quad (2a)$$

$$y_1 = \sin(SZA) * \sin(SAA) \quad (2b)$$

$$x_2 = \sin(VZA) * \cos(VAA) \quad (2c)$$

$$y_2 = \sin(VZA) * \sin(VAA) \quad (2d)$$

If modeling was performed with respect to the angles in the original spherical coordinate system, the distribution of reflectances would be discontinuous, as shown for the NIR and SWIR1 band solar zenith angles in Figures 3.3(a) and 3.3(b), respectively. The conversion

effectively spreads the data over the entire range of x_1 between $[-1, 1]$, as shown in Figures 3.4(a) and 3.4(b), respectively. Appendix Figures (A.4), (A.5), (A.6), and (A.7) show the reflectance distributions before and after solar and view angle coordinate conversion for all bands.

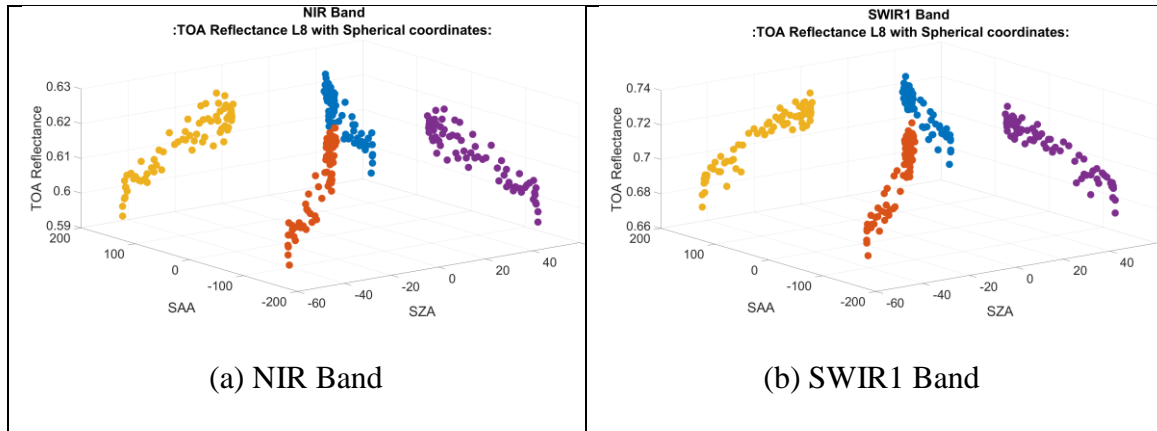


Figure 3.3 TOA Reflectance Vs Spherical Coordinate Solar Angles.

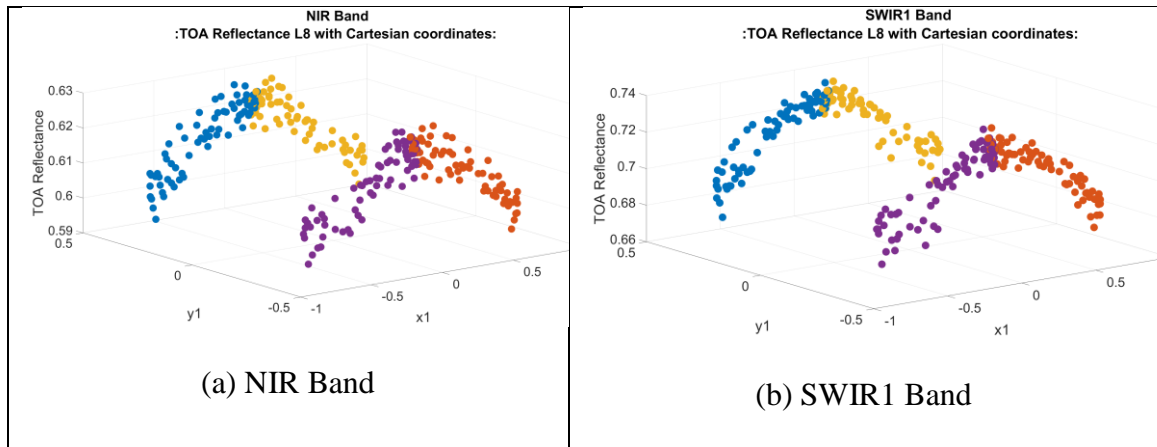


Figure 3.4 TOA Reflectance Vs Cartesian Coordinate Converted Solar Angles.

The transformed coordinates are inputs to a multilinear least-squares model where TOA reflectance is treated as the dependent ‘response’ variable and x_1, y_1, x_2, y_2 are treated as the independent variables. No interaction effects between the various angles are considered here. One important thing worth pointing out that the angles are taken as the mean of all

the angles inside an ROI for a better understanding of the impact of those angles on reflectances rather than taking the scene center angles.

$$\rho_{model} = \beta_0 + \beta_1 x_1 + \beta_2 y_1 + \beta_3 x_2 + \beta_4 y_2 \quad (3)$$

where $\beta_0, \beta_1, \beta_2, \beta_3$, and β_4 are the model coefficients.

Once the models have been generated, ‘reference’ solar and sensor view zenith/azimuth angles are selected in order to scale the TOA reflectances to a common level. The angles are selected by identifying a common set of solar and sensor view angles measured at all of the selected sites; to avoid ‘unrealistic’ TOA reflectance estimates, they should be within the range of angles used to compute the model parameters. After selecting the reference angles and using equations 2(a) – 2(d) to convert them to rectangular coordinates, a reference TOA reflectance is calculated from (3).

$$\rho_{Ref} = \beta_0 + \beta_1 * x_{1_Ref} + \beta_2 * y_{1_Ref} + \beta_3 * x_{2_Ref} + \beta_4 * y_{2_Ref} \quad (4)$$

The reference TOA reflectance is then scaled by the ratio of the observed and model predicted TOA reflectances to obtain the TOA reflectance applicable to the target site ROI:

$$\rho_{site} = \frac{\rho_{obs}}{\rho_{model}} \times \rho_{Ref} \quad (5)$$

3.5 Gain and Offset Calculation

After BRDF correction, the TOA reflectances from both sensors are now prepared for direct comparison. For each co-incident scene pair ROI, the uncalibrated sensor’s TOA reflectances are plotted as a function of the calibrated sensor’s TOA reflectances and a

linear least-squares regression is performed in order to determine the cross calibration gain and/or offset. In the ideal case where the TOA reflectances from both sensors are equal, all values would fall exactly on a 1-to-1 line; in general, the values do not fall exactly on the 1-to-1 line.

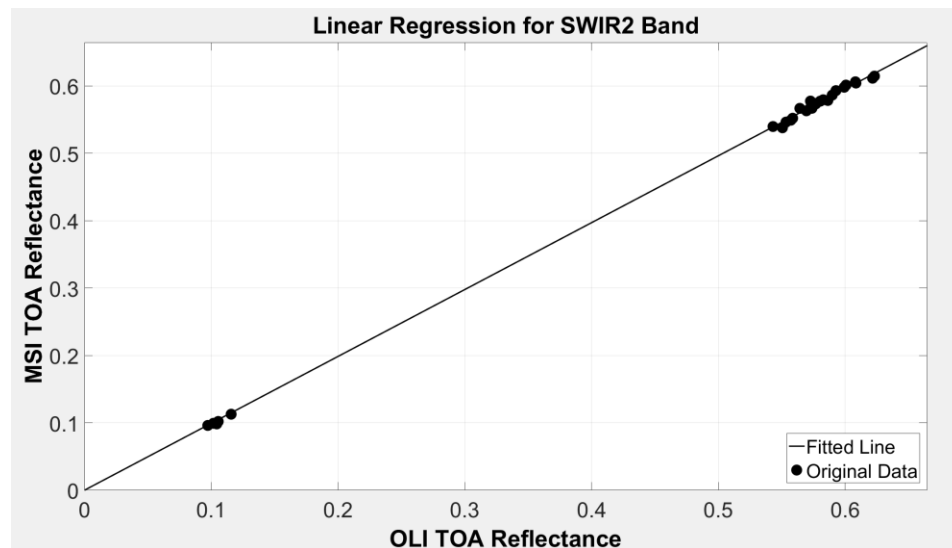


Figure 3.5 One to One Regression Plot of SWIR2 Band TOA Reflectance.

Figure 3.5 shows a regression plot for the MSI and OLI SWIR2 bands comparing the regression fit and the corresponding 1-to-1 line. TOA reflectances from dark and bright targets should be included in order to have the regression cover as wide a portion of the sensor dynamic range as possible.

t-tests at the 95% significance level are performed to assess the resulting regression fits. In all cases, the ‘null’ hypothesis is that the slope (gain) is 1, versus the ‘alternative’ hypothesis that it differs from 1. Similar t-tests are performed, at the 95% significance level, to determine whether the intercept (offset) differs from 0.

3.6 Uncertainty Analysis

This section presents the process used to determine the individual uncertainty components and the overall cross calibration uncertainty. Consistent with the uncertainty classification proposed in [31], the expected uncertainties can be grouped as follows:

- Uncertainty in the Spectral Domain
- Uncertainty in the Spatial Domain
- Uncertainty in the Temporal Domain

3.6.1 Uncertainty in Spectral Domain

For the purposes of this thesis, spectral domain uncertainty affects the estimated SBAFs. It is associated with the spectral behaviors of the reference and uncalibrated sensors, as well as the behavior of the hyperspectral sensor whose data are used in the SBAF estimation. One component of this uncertainty is inherent in the pre-launch measurement of the sensor RSRs. Another is due to shifts in the spectral filter central wavelength and/or changes in filter bandwidth over time in each sensor [34], [35]. A third component is due to the interpolation process changing the spectral resolution of the hyperspectral image data. Each component is considered in greater detail in the following sections.

3.6.1.1 Uncertainty in Pre-launch RSR

Since an end user does not usually have direct access to the pre-launch RSR characterization data, the corresponding uncertainty is given in a user guide/handbook

provided by the organization responsible for operating the sensor. It can be considered a fixed value.

3.6.1.2 Uncertainty Due to Spectral Filter Changes

The uncertainty due to center wavelength shift is determined according to the following procedure.

1. Keeping the OLI RSR fixed around its center wavelength, shift the MSI RSR in increments of 1 nm to a maximum of 10 nm, towards both shorter and longer wavelengths. After each shift, calculate the SBAF according to Equation (1).
2. Keeping the MSI RSR fixed around its center wavelength, shift the OLI RSR in increments of 1 nm to a maximum of 10 nm, towards both shorter and longer wavelengths. After each shift, calculate the SBAF according to Equation (1).
3. For the entire set of SBAFs calculated in steps 1 and 2, determine the average estimated SBAF, standard deviation, and uncertainty. Take the uncertainty as the ratio of the standard deviation to the mean.

As described above, the procedure does not explicitly account for shifts in the hyperspectral sensor RSR. In fact, these shifts are implicitly accounted for; the uncertainty estimate is the same as if the hyperspectral data were shifted in 1 nm increments, keeping both the MSI and OLI RSRs fixed at their nominal center wavelengths.

To find the uncertainty due to bandwidth change, the following procedure is used:

1. Keeping the OLI RSR bandwidth fixed, narrow and widen the MSI bandwidth in increments of 1 nm to a maximum of 5 nm, with the MSI center wavelength fixed

at its nominal value. After each change in bandwidth, calculate the SBAF according to Equation (1).

2. Keeping the MSI RSR bandwidth fixed, narrow and widen the OLI bandwidth in increments in 1 nm to a maximum of 5 nm, with the OLI center wavelength fixed at its nominal value. After each bandwidth change, calculate the SBAF according to Equation (1).
3. From the set of SBAFs generated in steps 1 and 2, determine the mean SBAF, standard deviation, and uncertainty. Take the uncertainty as the ratio of the standard deviation to the mean.

3.6.1.3 Uncertainty in Hyperspectral Profile Interpolation

For the purposes of this thesis, image data from the EO-1 Hyperion sensor are used to determine the hyperspectral profile of the target site ROI. The nominal spectral resolution of each band is 10 nm. In order to determine the SBAF, the hyperspectral data are linearly interpolated to 1 nm spectral resolution. An uncertainty component is introduced through this process; the uncertainty is increased in bands that are more sensitive to atmospheric absorption. Consistent with the approach described in [36], the uncertainty resulting from the interpolation is determined as follows.

The linear interpolation estimating the value \hat{y} at a point x , between the points x_1 and x_2 , is given by

$$\hat{y} = y_1 \times \frac{x - x_2}{x_1 - x_2} + y_2 \times \frac{x - x_1}{x_2 - x_1} \quad (11)$$

where x_1 and x_2 are the two neighboring points of x . i.e., $x_1 \leq x \leq x_2$.

The uncertainty associated with the estimated \hat{y} is given by

$$u^2(\hat{y}) = \left(\frac{(x - x_2)}{(x_1 - x_2)} \right)^2 u^2(y_1) + \left(\frac{(x - x_1)}{(x_2 - x_1)} \right)^2 u^2(y_2) \quad (12)$$

where $u(y_1)$ and $u(y_2)$ are the uncertainties associated with y_1 and y_2 , respectively.

3.6.2 Uncertainty in Spatial Domain

Another source of uncertainty in the estimated cross calibration relates to spatial variability.

Two contributing to this uncertainty are considered in additional detail in this section.

- Uncertainty due to Geometric Registration Differences
- Uncertainty due to Differences in Spatial Resolution

This section considers each of these uncertainty sources in additional detail.

3.6.2.1 Uncertainty Due to Geometric Registration Error

The estimated position and location of a given ground feature or ROI imaged by a given sensor will vary due to variations in the sensor optical path, sensor altitude and orientation during the imaging process, and imaging techniques (e.g. variations in scanning time, detector sampling, etc). These variations introduce uncertainty in the final geometric registration of the feature, and this uncertainty contributes to the overall uncertainty in the cross calibration. The procedure used to estimate the uncertainty due to potential geometric registration error for a given sensor is described below. The procedure is performed for both sensors.

1. Calculate the mean TOA reflectance within the optimal ROI at its estimated location within the image.
2. Shift the ROI from its nominal position by 60m, 120m, 180m and 300m. These shifts are directed upwards, downwards, to the right, and to the left. After each shift, calculate the mean TOA reflectance of the ROI. The corresponding pixels the ROI is shifted are given in Table 1 for both sensors.

Misregis- tration (m) Bands	60m		120m		180m		300m	
	OLI pixel	MSI pixel	OLI pixel	MSI pixel	OLI pixel	MSI pixel	OLI pixel	MSI pixel
CA	2	1	4	2	6	3	10	5
Blue	2	6	4	12	6	18	10	30
Green	2	6	4	12	6	18	10	30
Red	2	6	4	12	6	18	10	30
NIR	2	3	4	6	6	9	10	15
SWIR1	2	3	4	6	6	9	10	15
SWIR2	2	3	4	6	6	9	10	15

Table 3.1 Misregistration and Corresponding Shift in Pixels for OLI and MSI.

3. From the set of TOA reflectances calculated in steps 1 and 2, determine the mean TOA reflectance, standard deviation, and uncertainty. Take the uncertainty as the ratio of the standard deviation to the mean TOA reflectance.

3.6.2.2 Uncertainty due to Differences in Spatial Resolution

OLI and MSI differ in their ground sampling distance (GSD) or spatial resolution. The OLI has a spatial resolution of 30 m in all bands but the panchromatic band. MSI has a spatial resolution of 60 m in the Coastal Aerosol band, 10 m for the Blue, Green, and Red bands, and 20 m for the NIR, SWIR1, and SWIR2 bands. OLI image data will need to be re-sampled to match the MSI resolution (or MSI data will need to be re-sampled to match OLI resolution). The re-sampling process has an associated uncertainty that contributes to the overall cross calibration uncertainty. This section describes the procedure used to estimate this uncertainty component for each target site. The procedure is performed for each corresponding band.

1. Calculate the mean TOA reflectance of the MSI ROI.
2. Resample the MSI ROI using bilinear interpolation to match the spatial resolution of the corresponding pixels in the OLI ROI.
3. Calculate the mean TOA reflectance in the MSI ROI after resampling.
4. Determine the % difference in TOA reflectance before and after sampling.
5. Repeat steps 1-4 to calculate % difference in OLI TOA reflectance before and after re-sampling the pixels to match the spatial resolution of the corresponding pixels in the MSI ROI.
6. Estimate the uncertainty for each site as the average of its % differences.

3.6.2.3 Uncertainty due to Site Non-Uniformity

To simplify analysis, it is typically assumed that target sites exhibit Lambertian surface reflectance characteristics (i.e. the incident electromagnetic energy is reflected equally in

all directions). In practice, this seldom, if ever, occurs. In addition, target site surfaces are often non-uniform to varying degrees, due to the differing composition of materials found on the surface. Consequently, there are uncertainties associated with non-Lambertian reflectance behavior and surface non-uniformity. Estimating the uncertainty associated with non-Lambertian behavior is beyond the scope of this thesis work. The uncertainty associated with surface non-uniformity, however, can be estimated reasonably straightforwardly. This section describes how this uncertainty component is estimated. The procedure described below is to be performed for each band, on scenes acquired from the bright target PICS.

1. For an individual cloud free scene, calculate the mean TOA reflectance and standard deviation over the ROI for the given target site.
2. Take the ratio of the standard deviation to the mean TOA reflectance to get the spatial uncertainty for the individual scene.
3. Repeat steps 1 and 2 for all cloud free scenes.
4. Determine the mean uncertainty of all scenes.

3.6.3 Uncertainty in Temporal Domain

Differences in overpass times between two sensors imaging the same target site can result in differences in atmospheric transmittance seen by each sensor, which introduces uncertainty in the final cross calibration. This uncertainty can be divided into two components:

- Uncertainty due to sun angle differences

- Uncertainty due to atmospheric changes (e.g. changes in water vapor and/or aerosol content)

For most cross calibration analyses of PICS or other bright target desert sites, the sensor overpass times are “close enough” (within 30 minutes at most) that differences in atmospheric conditions are minimal and can be ignored; for overpass time differences of more than 30 minutes or for dark target sites such as Lake Tahoe, NV, atmospheric effects can have greater impact. For the purposes of this thesis, both uncertainty components are considered in greater detail.

3.6.3.1 Uncertainty Due to Sun Angle Differences

The uncertainty associated with sun angle differences is computed as described below. The description is given for calculation on a summer date; with appropriate modifications, the procedure is also applicable for calculation on a winter date. The analysis is performed for each sensor individually.

1. Select the date in the summer where image data from both sensors have been acquired, and the solar zenith angle is at its absolute seasonal minimum (solar elevation is at its absolute seasonal maximum).
2. Vary the overpass times in increments of 30 seconds, up to a maximum difference of 30 minutes. For each increment, estimate the solar zenith and solar azimuth angles.
3. Use MODTRAN to determine the corresponding TOA reflectances seen by a sensor for each solar zenith angle/azimuth angle pair. The inputs for these MODTRAN

runs consist of the sensor RSR and solar angle pair. The MODTRAN runs should specify an atmospheric profile appropriate for the season. Other MODTRAN parameters should be left at their ‘default’ or standard settings.

4. Calculate the mean TOA reflectance, standard deviation and uncertainty. As before, take the uncertainty as the ratio of the standard deviation to the mean.

3.6.3.2 Uncertainty Due to Atmospheric Changes

The procedure used to estimate the uncertainty due to changes in atmospheric conditions is described below. For this analysis, the dates selected for the uncertainty analysis described in the previous section are used. The analysis is performed for each sensor individually.

1. Keeping the solar zenith and solar azimuth angles fixed with respect to the MSI overpass time (as it has the earlier overpass time), generate random samples of the water vapor and aerosol optical depth from the corresponding normally distributed means and standard deviations, as specified in [37].
2. Use MODTRAN to determine the TOA reflectances at the fixed solar zenith/azimuth angles and sample water vapor / aerosol optical depths. As before, an additional input to each run is the sensor RSR. The atmospheric profile appropriate to the season should be specified for each run, and the other MODTRAN parameters should be kept at their default or standard settings.
3. From the set of TOA reflectances, calculate the mean, standard deviation and uncertainty. Take the uncertainty as the ratio of the standard deviation to the mean.

3.7 Summary

This chapter has described the proposed cross calibration approach and uncertainty analysis. Most of the steps in the proposed approach are consistent with previous cross calibration analyses; the analysis uses a straightforward BRDF model that considers all solar and sensor view angles, as oppose to the one or two angles considered in previous analyses. The results obtained with the proposed approach and estimates of its overall uncertainty are presented in Chapter 4.

Chapter 4 Result and Discussion

This chapter presents the results of reflectance-based cross calibration of the MSI to the OLI. The results for four Saharan desert PICS are presented first. Cross calibration results based on Algodones Dunes data are presented as a validation of the proposed approach.

4.1 Scene Pairs

Cloud-free images of the Libya1, Libya4, Niger2 and Sudan1 PICS were selected to represent bright targets. Similarly, cloud-free images of Lake Tahoe and a volcanic crater near the Libya1 PICS were selected to represent dark targets. A total of 35 scene pairs were selected from the sites; 5 scene pairs from the volcanic site were nearly co-incident (acquisitions within 3 days of each other). Table 4.1 gives the number of scene pairs selected from each target site.

Site	WRS2 Path/Row	Number of Scene pairs	Coincident/Near Coincident
Libya 1	187/043	4	Coincident
Libya 4	181/040	8	Coincident
Niger 2	188/045	7	Coincident
Sudan 1	177/045	9	Coincident
Lake Tahoe	043/033	2	Coincident
Libya Volcano	184/043	5	Near Coincident

Table 4.1 Scene Pairs Used for Cross Calibration.

The ROIs from the sites were identified as “optimal” by previous research [40]. For the purposes of this work, an “optimal” ROI contains a rectangular region exhibiting 3% or less temporal, spatial, and spectral variability with respect to TOA reflectance. The corner coordinates defining these ROIs are given in Appendix 1.

4.2 SBAF Calculation

As mentioned in Chapter 3, SBAFs were calculated for each site such that the MSI response was “matched” to the OLI response. The inputs to the SBAF calculations were the band-specific sensor RSR profiles and overall hyperspectral profiles of the site ROIs acquired from Hyperion image data screened for clouds and shadows. For each ROI, the mean TOA reflectance and associated standard deviation were calculated for each calibrated Hyperion band (196 bands total); TOA reflectances 2.5 standard deviations or more beyond the mean reflectance in any band resulted in a Hyperion scene being excluded from the SBAF calculations. Profiles of the Libya4 PICS ROI from 383 scenes before and after filtering are shown in Figure 4.1. The filtering process resulted in 343 useable scenes for this site.

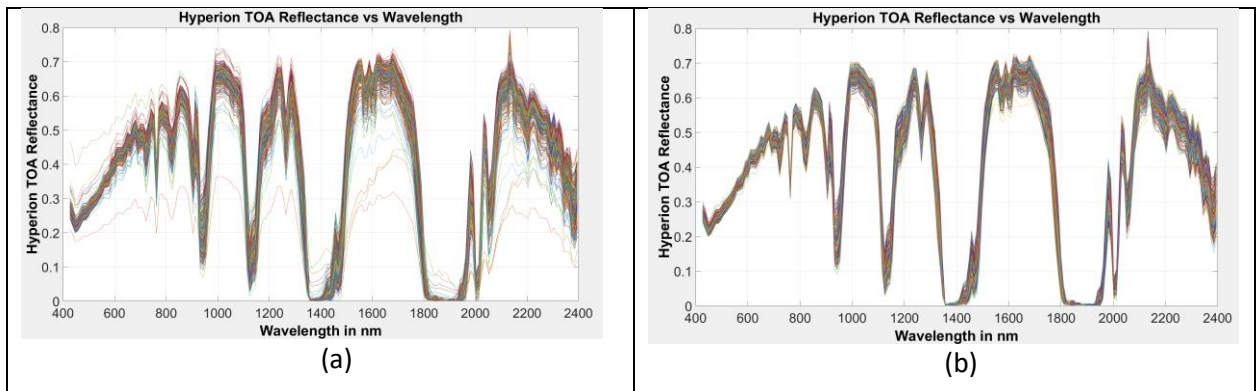


Figure 4.1 Hyperion Scenes for Libya 4, (a) Before Filter Application, (b) After filter Application.

Once the hyperspectral data was cloud screened, a set of SBAFs was calculated for each site and for each band. The mean SBAF for each site and band was taken as the representative SBAF. Figure 4.2 shows the band-specific distribution of SBAFs derived from the 343 hyperspectral profiles shown in Figure 4.1(b). For easier visualization, the SBAF histograms were generated using 100 bins.

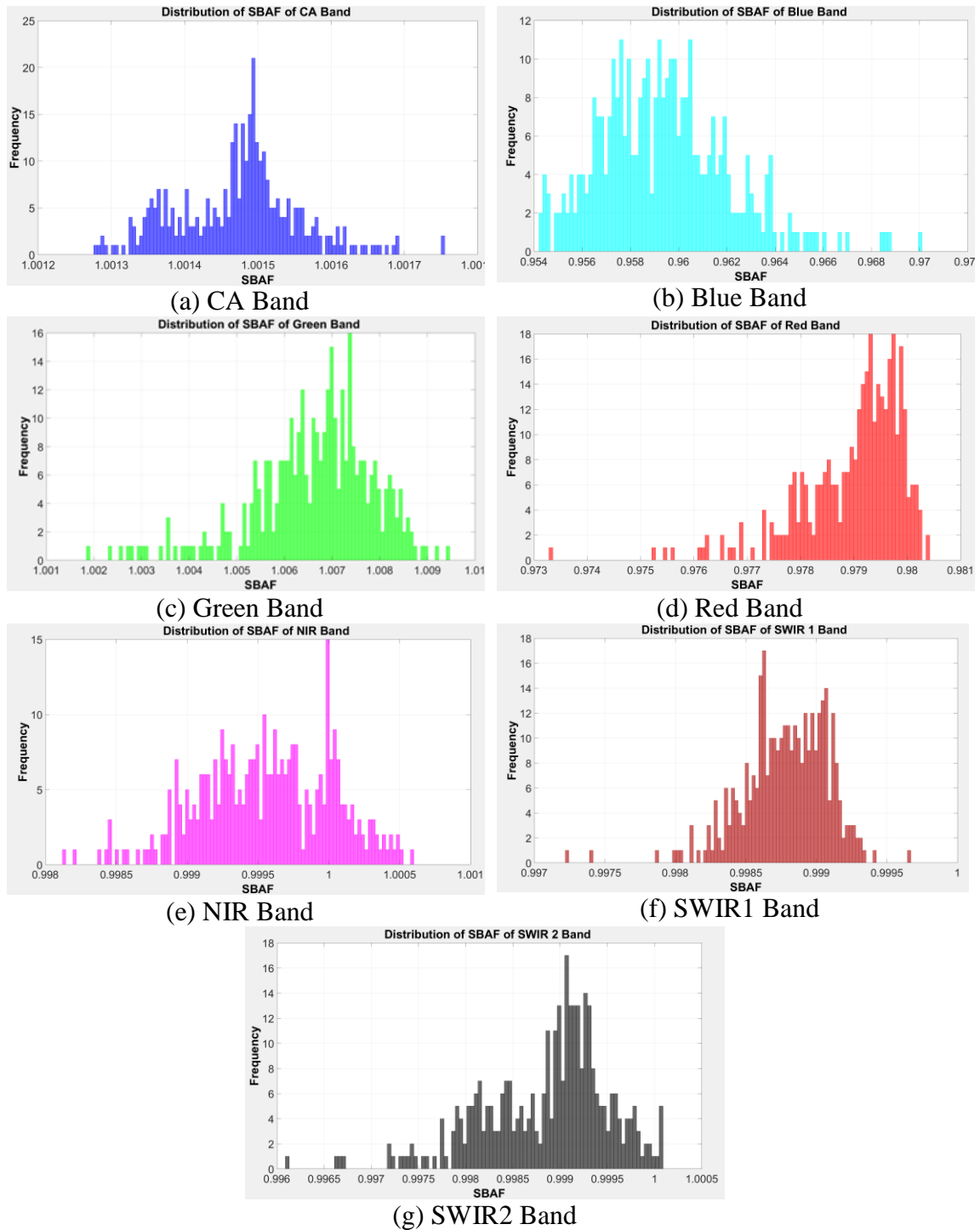


Figure 4.2 SBAF Distribution for Libya4 PICS for Different Bands.

The distributions do not appear to fit a normal distribution in any band, nor do they appear to demonstrate consistent features across bands. The distribution appears to be bi-modal in

the Coastal Aerosol band; it seems reasonable that bi-modal distributions should be observed in the other bands as well, since the scene set includes both summer and winter acquisitions. As shown in Table 4.2, the estimated SBAF values in each band are highly concentrated about the mean with minimal spread.

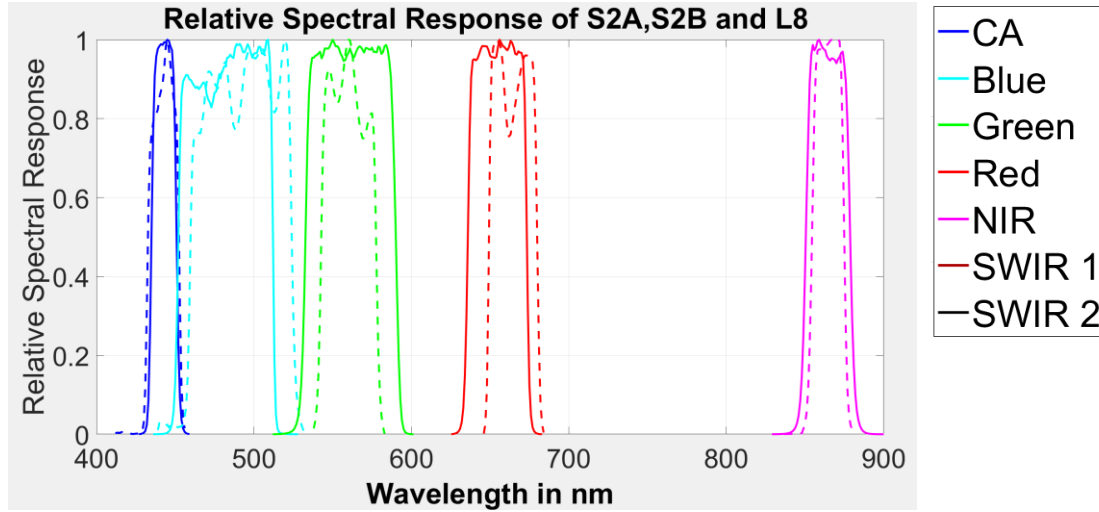
Bands	CA	Blue	Green	Red	NIR	SWIR1	SWIR2
SBAF	1.0015	0.9594	1.0066	0.9790	0.9996	0.9988	0.9989
Standard Deviation	0.0001	0.0027	0.0013	0.0010	0.005	0.003	0.007

Table 4.2 Mean Band-Specific SBAF and Standard deviation.

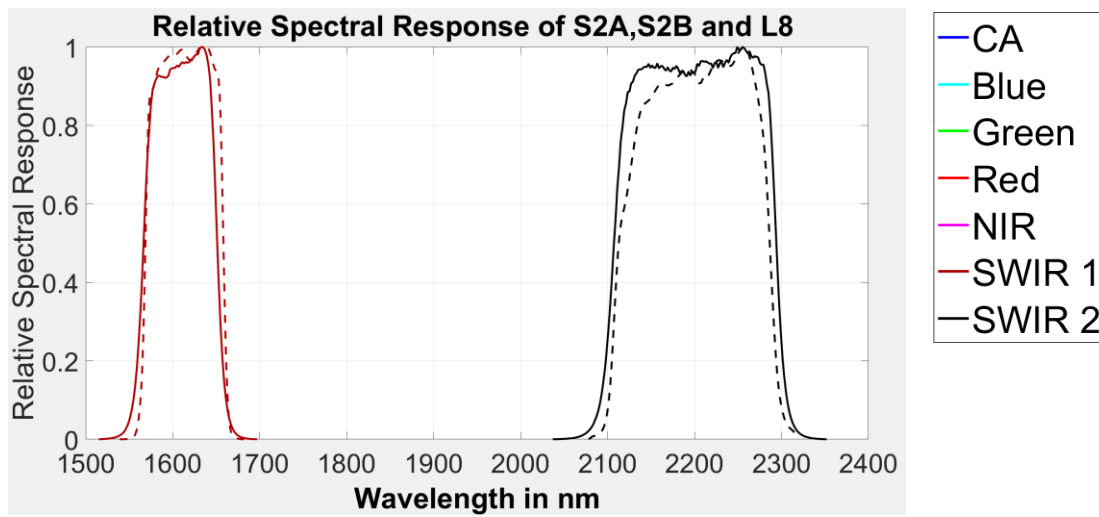
Table 4.3 gives the mean band-specific SBAFs for the other sites. The bright target SBAFs for the Blue, Green, and Red bands differed the most from 1.0. This can be seen in the RSR comparison shown in Figure 4.3(a), where the RSRs in these bands differed in overall shape, center wavelength, and/or bandwidth. Similarly, the bright target SBAFs in the NIR, SWIR1, and SWIR2 bands were very close to 1.0; as seen in Figure 4.3(b), the RSRs in these bands were very similar in overall shape, center wavelength, and/or bandwidth. The dark target SBAFs tended to differ from 1.0 more in all bands, most likely due to lower signal levels and/or noise.

Bands Sites	Scenes used	CA	Blue	Green	Red	NIR	SWIR1	SWIR2
Libya 1	81	1.0017	0.9603	1.0217	0.9777	0.999	0.9988	1.0010
Niger 2	12	1.0016	0.9681	1.0112	0.9794	1.0003	0.9989	1.0002
Sudan 1	152	1.0015	0.9643	1.0131	0.9793	1.0001	0.9990	1.0003
Lake Tahoe	25	1.02	1.08	0.982	1.018	1.005	0.998	0.998
Volcanic near Libya	4	1.0015	0.9659	1.0058	0.9800	1.0001	0.9990	0.9981

Table 4.3 Summary of the SBAF of All Target Sites.



(a)



(b)

Figure 4.3 Relative Spectral Response of OLI (Solid Line) and MSI (Dotted Line).

4.3 BRDF Models and Correction

As mentioned in Chapter 3, a four angle BRDF model was proposed that projects the solar and sensor view angles from a spherical coordinate space to a plane Cartesian coordinate space. BRDF corrections were derived from this model and applied to the images in all of the bright target scene pairs; there was insufficient cloud-free image data from the dark

target sites to run a similar comparison. Table 4.4 compares the OLI TOA reflectance uncertainty before and after correction with the four angle model, to the TOA reflectance uncertainty before and after correction with linear and quadratic models based on the solar zenith angle alone. For the Coastal Aerosol and Blue bands, the proposed four angle model provided a similar amount of correction to the linear SZA model and less correction than the quadratic SZA model, with little to no overall correction. For longer wavelength bands, the four angle model provided a significant amount of correction, but the amount of correction was similar to that provided by both SZA models. Overall, based on these results, the choice of BRDF model among these candidates would not seem to be critical.

Bands	Before Correction	Correction with Linear SZA based Model	Correction with Quadratic SZA based Model	Correction with 4 angle BRDF model
CA	1.5	1.19	1.08	1.19
Blue	1.25	1.19	1.12	1.15
Green	1.08	0.93	0.93	0.89
Red	1.23	0.85	0.84	0.81
NIR	1.28	0.73	0.69	0.65
SWIR1	2.08	0.61	0.60	0.58
SWIR2	2.48	1.91	1.80	1.76

Table 4.4 Percentage Uncertainty in OLI TOA Reflectance of Libya4 PICS Data Before and After BRDF Correction.

Figures 4.4(a) – 4.4(g) show the OLI band-specific lifetime temporal trends of the Sudan1 PICS before and after application of the four angle BRDF correction.

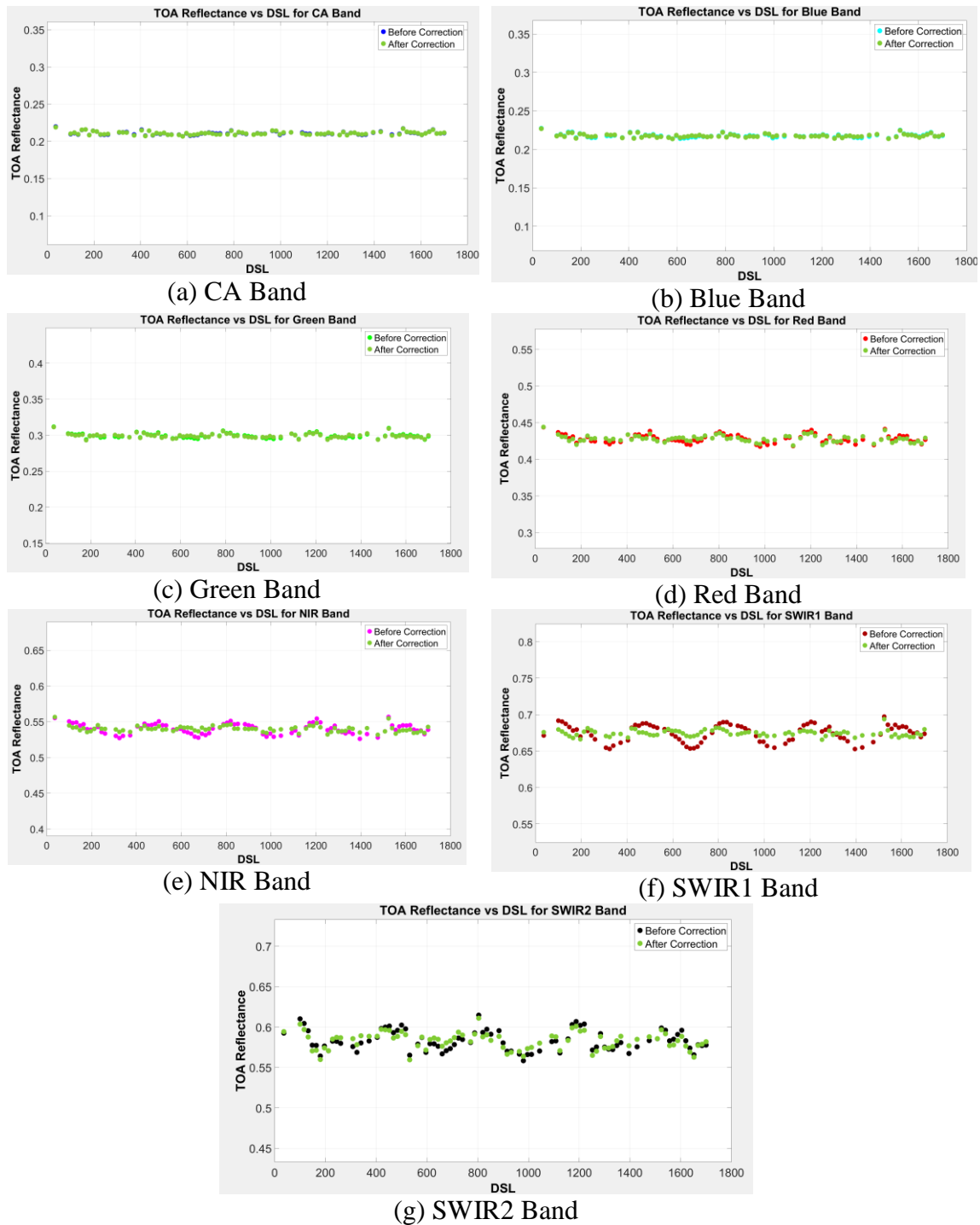


Figure 4.4 Before and After BRDF Corrected TOA Reflectance of OLI over Sudan1 Site.

The correction results are consistent with that observed for the OLI TOA reflectance uncertainties – the Coastal Aerosol and Blue bands show little to no correction (with the data mostly overlapping), and the longer wavelength bands (especially the NIR, SWIR1 and SWIR2 bands) show significant correction.

Figure 4.4 shows an example of the OLI temporal trend before and after BRDF correction with the proposed four angles model. In the shorter wavelength bands, as noted above, there was little apparent change in the uncertainty; more visually apparent correction occurred in the longer wavelength bands, with significant reductions ($> 10\%$) in the associated uncertainty. Table 4.5 shows the before and after correction reflectance summary of the BRDF process. The after correction uncertainty is lowest for NIR and SWIR1 bands, while for CA and Blue bands, there was a negligible amount of correction. Rest of the bands shows moderate correction.

Bands	Before Correction			After Correction			Change in
	Mean	STD	Uncertainty in %	Mean	STD	Uncertainty in %	Uncertainty in %
CA	0.211	0.002	1.11	0.211	0.002	1.09	1.80
Blue	0.218	0.003	1.13	0.218	0.002	1.05	7.08
Green	0.299	0.003	1.10	0.299	0.003	1.00	9.09
Red	0.428	0.006	1.32	0.428	0.005	1.05	20.45
NIR	0.540	0.007	1.34	0.540	0.004	0.78	41.79
SWIR1	0.675	0.012	1.70	0.675	0.004	0.64	62.35
SWIR2	0.583	0.012	2.13	0.583	0.010	1.79	15.96

Table 4.5 Sudan1 OLI TOA Reflectance's Before and After Four Angle BRDF Correction.

4.3.1 Reference Angle Selection

For both sensors, a set of ROI-specific solar and view angles were derived for each target site, based on the average of the measured pixel-specific sets of angles within the site ROI from all of the cloud-free scenes acquired over the site. The averaged sets of ROI angles from both sensors were then plotted on a common plot for each site, as shown in Figures 4.5(a) – 4.5(d) for the Libya1 PICS. From the set of plotted angles, a ‘common’ set of reference solar and view angles, applicable to both sensors, was selected to account for differences in sensor focal plane geometry and satellite/sensor orientation.

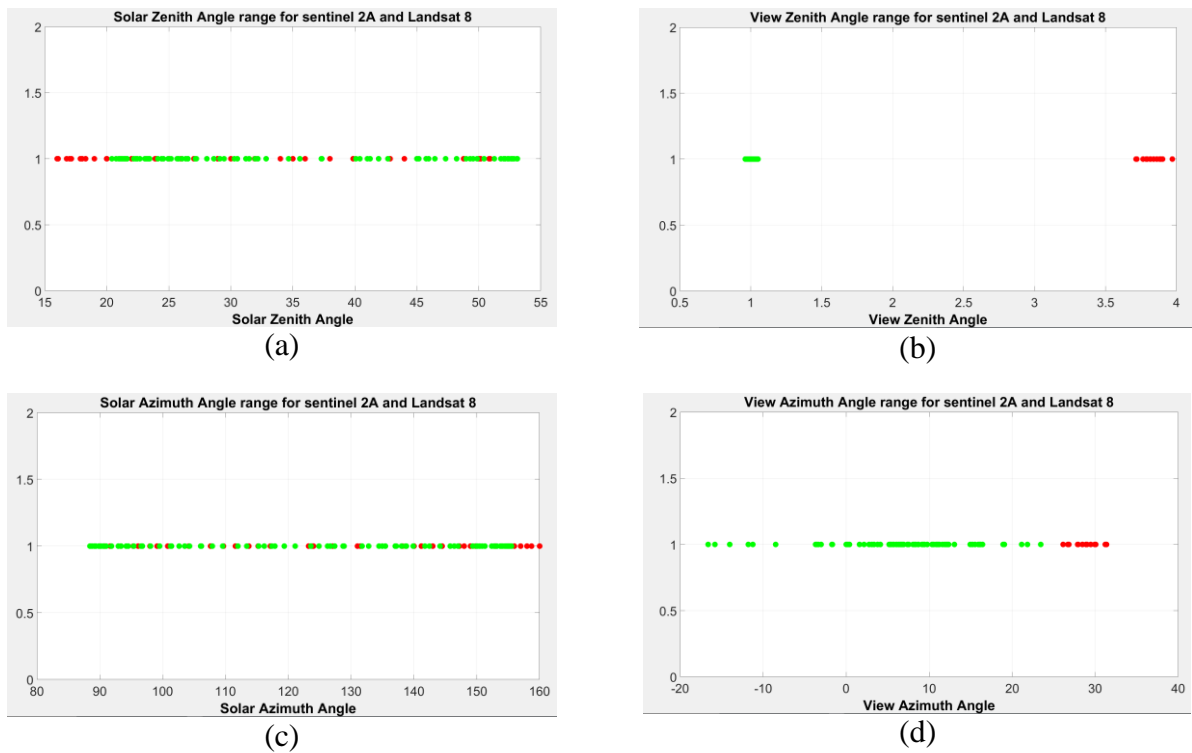


Figure 4.5 Plot of different angles over Libya 1 Sentinel 2A (Red Marker), Landsat 8 (Green Marker) (a) Solar Zenith Angle, (b) View Zenith angle, (c) Solar Azimuth angle and (d) View Azimuth angle.

A critical constraint guiding the selection process was that the reference angles fall within the ranges of observed angles in order to avoid calculation of invalid TOA reflectance values. As seen in Figure 4.5(a), a reasonable choice for a reference solar zenith angle is on the order of 30° . From Figure 4.5(b), a reasonable reference view zenith angle is approximately 3° ; even though there is no overlap in the observed view zenith angles from each sensor, the range of view angles was quite small (on the order of 3.5°). Similarly, Figures 4.5(c) and 4.5(d) suggest reasonable solar and view azimuth angles of 125° and 10° , respectively.

4.4 Gain and Bias Calculation

Least-squares linear regression was performed to determine the cross calibration gain and offset for each band, with the BRDF-corrected OLI TOA reflectances as the independent ‘predictor’ variable and the SBAF/BRDF corrected MSI TOA reflectances as the dependent ‘response’ variable. The regression data were plotted with the estimated regression line and a 1-to-1 line representing an exact match between OLI and MSI TOA reflectances.

With the exception of the Blue band, the estimated offsets from the 1-1 line were generally quite small, less than 0.002 in magnitude.

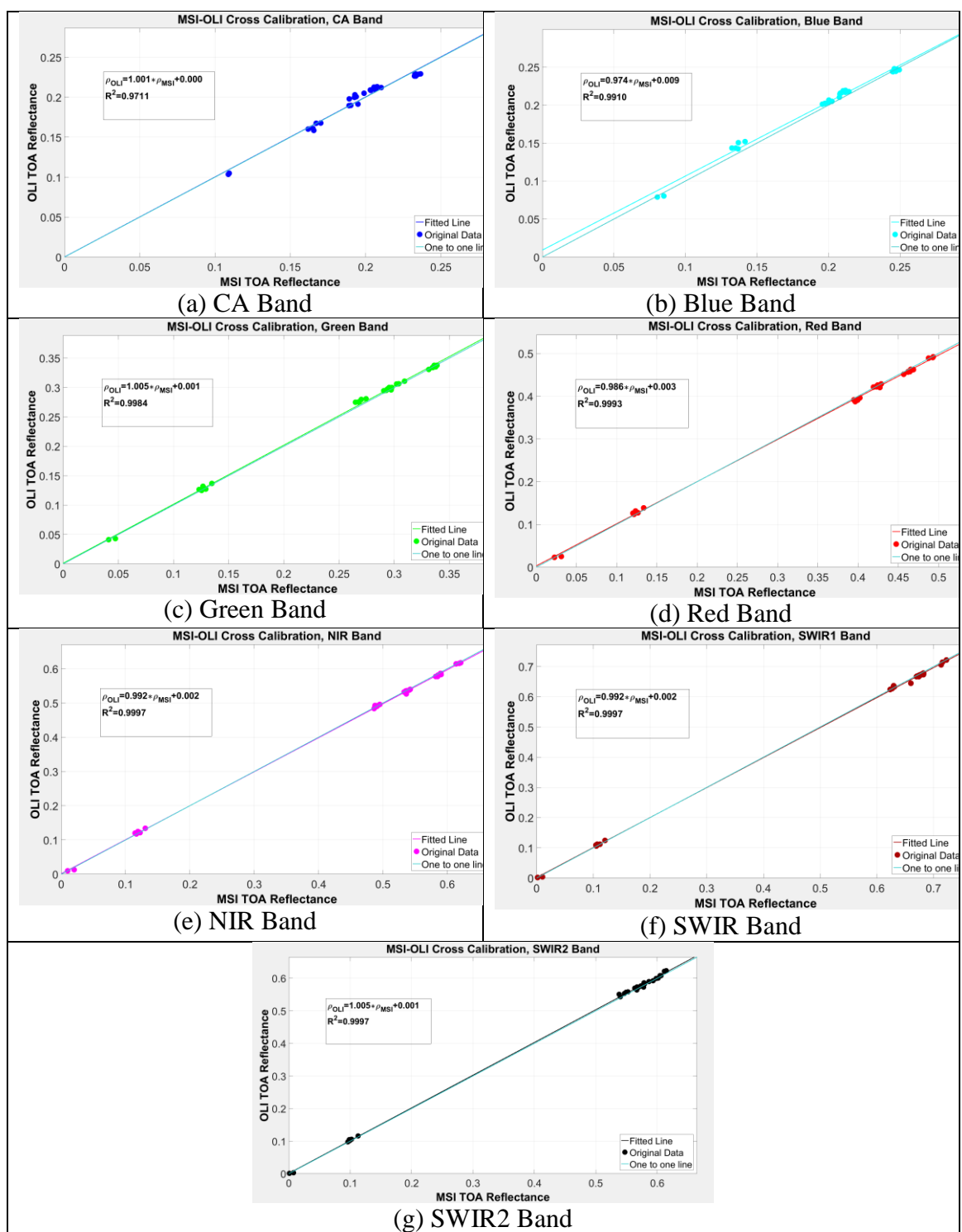


Figure 4.6 Regression Line for the Cross Calibration of OLI and MSI.

Bands	Coefficient	Estimate	SE	t-stat	p value	Null Hypothesis
CA	Bias	0.0002	0.0065	0.0240	0.9810	Fail to Reject
	Gain	1.0012	0.0326	30.6686	4.31E-23	Reject
Blue	Bias	0.0092	0.0035	2.6053	0.0145	Reject
	Gain	0.9740	0.0176	55.3842	3.69E-30	Reject
Green	Bias	0.0010	0.0020	0.5090	0.6147	Fail to Reject
	Gain	1.0046	0.0075	133.5984	8.00E-41	Reject
Red	Bias	0.0030	0.0019	1.6214	0.1161	Fail to Reject
	Gain	0.9856	0.0048	206.6281	4.03E-46	Reject
NIR	Bias	0.0016	0.0015	1.0317	0.3110	Fail to Reject
	Gain	0.9923	0.0031	315.9175	2.79E-51	Reject
SWIR1	Bias	0.0018	0.0019	0.9621	0.3442	Fail to Reject
	Gain	0.9922	0.0031	315.4981	2.89E-51	Reject
SWIR 2	Bias	0.0011	0.0017	0.6358	0.5301	Fail to Reject
	Gain	1.0051	0.0034	297.3908	1.51E-50	Reject

Table 4.6 Gain and Bias Statistics of Cross-Calibration Regression of MSI and OLI.

There does appear to be a slight deviation in the regression slopes from the 1-1 line, indicating cross calibration gains different from 1. Table 4.6 presents the results of hypothesis tests on the regression slopes and intercepts (gain and offset, respectively) at the 95% significance level. There is sufficient statistical evidence to conclude the cross calibration gains differ from 1.0, and insufficient statistical evidence to conclude the offsets are different from 0 except in case of Blue band. The offset p-value for the Blue band is indicating that the offset is different from 0 statistically.

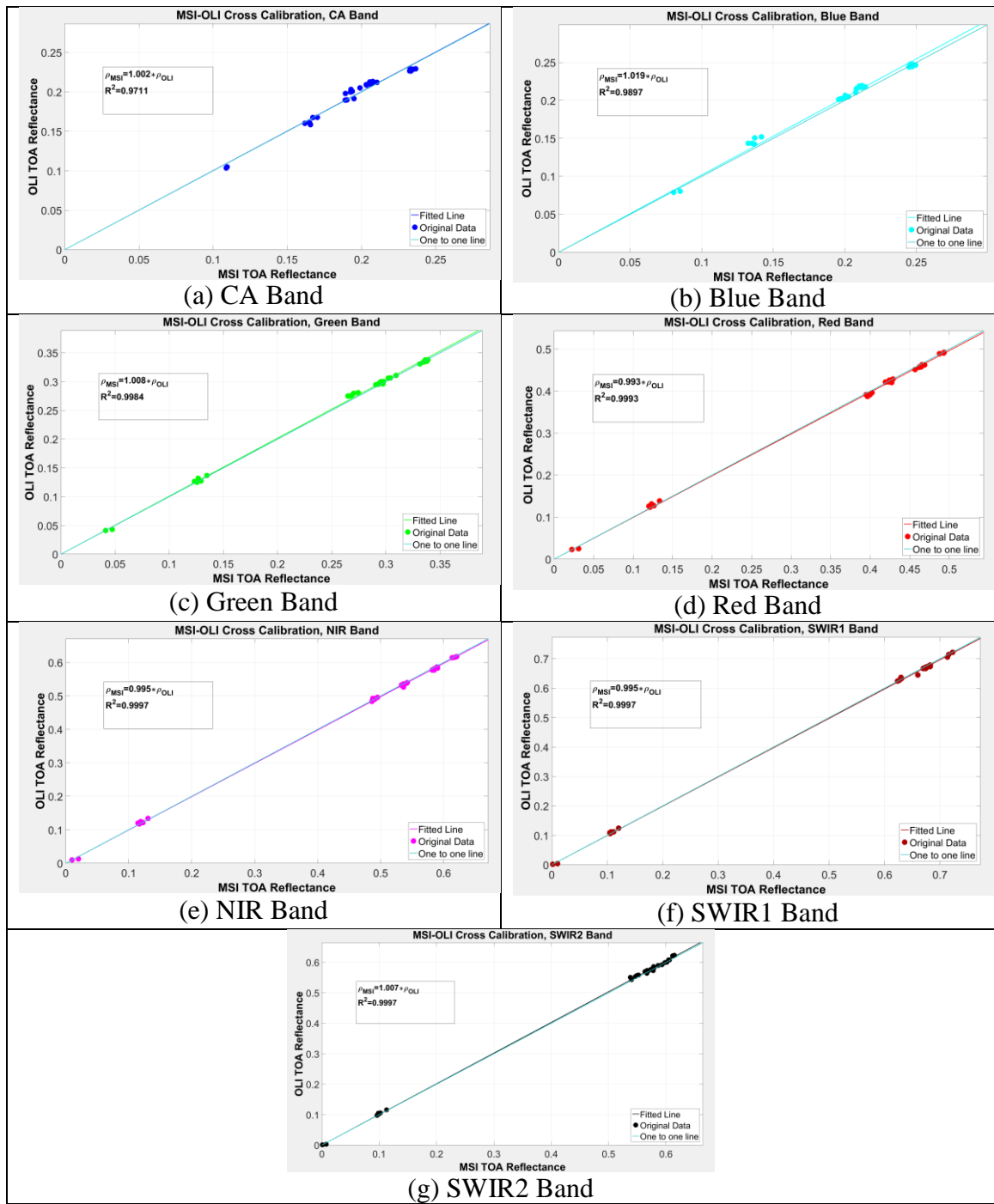


Figure 4.7 Regression Line for the Cross Calibration of OLI and MSI Without Bias.

Since there was insufficient evidence to justify assuming a nonzero offset (except in the Blue band), alternative regressions were performed such that the intercepts were forced to pass through 0. Plots of the updated regressions are shown in Figures 4.7(a) – 4.7(g). The slope hypothesis tests were re-run, again at the 95% significance level. Table 4.6 presents

the results of the updated tests. Clearly, as noted with the full regression hypothesis tests, there is sufficient statistical evidence to conclude the cross calibration gains in all bands differ from 1.0.

Bands	Estimate of Gain	SE	t-stat	p value	Null Hypothesis
CA	1.0020	0.0052	193.6356	1.11E-46	Reject
Blue	1.0186	0.0044	231.0527	6.62E-49	Reject
Green	1.0083	0.0024	415.2936	2.74E-56	Reject
Red	0.9928	0.0019	528.7881	2.49E-59	Reject
NIR	0.9952	0.0013	770.6915	4.49E-64	Reject
SWIR1	0.9949	0.0013	741.2162	1.39E-63	Reject
SWIR2	1.0070	0.0014	711.2575	4.60E-63	Reject

Table 4.7 Gain and Bias Statistics of Cross-Calibration Regression of MSI and OLI.

Table 4.7 shows the percent differences in the estimated gains, using the 0-offset gains as the basis for comparison. It is apparent that the shorter wavelengths have larger differences in gain than the longer wavelengths. This would be expected as the shorter wavelength bands, especially the Blue band, had significantly larger offsets.

4.5 Uncertainty Estimation

This section presents the results of uncertainty analysis on the estimated cross calibration gains. As mentioned in Chapter 3, the overall uncertainty in the estimated gain is determined from spectral, spatial, and temporal uncertainties.

4.5.1 Uncertainty in Spectral Domain

4.5.1.1 Uncertainty Inherent in RSR Measurements

As mentioned earlier, sensor RSRs are typically measured prior to launch; these measurements will have associated uncertainties with them. The RSRs can also change

over time due to stresses occurring during launch and component aging. Barsi *et al.* [38] described changes in the OLI RSRs due to cross-talk effects among the bands and their effects in the final reflectance values. The uncertainty in radiance due to observed cross-talk effects between bands was as high as 0.35%, with an uncertainty between the SWIR1 and SWIR2 bands as high as 0.15%.

The Sentinel 2 data quality report published in February 2018 [39] reported a spectral response non uniformity identified in the MSI. The non-uniformity manifests as soft-edged darker and brighter stripes near detector module boundaries in the along-track direction. The stripes are most apparent in the Green and Vegetation Red Edge bands (Bands 3 and 5). The maximum uncertainty in the RSR due to this anomaly was estimated as high as 2% (when the scene spectrum changes significantly over the detector's spectral bandwidth); the typical uncertainty due to this anomaly was estimated to 1%.

4.5.1.2 Uncertainty Due to Spectral Filter Change

Figure 4.8 shows the SBAF distribution based on use of an individual Hyperion scene of the Libya 4 PICS. Multiple peaks can be observed in the distributions in most bands, as seen in Figures 4.8(a) – 4.8(g), suggesting a clustering of SBAF values around a set of means. The tails of each cluster appear to overlap into adjacent clusters. The clustering may be due to a greater degree of ‘flatness’ in the Hyperion spectrum; when the RSRs are shifted, similar values are calculated.

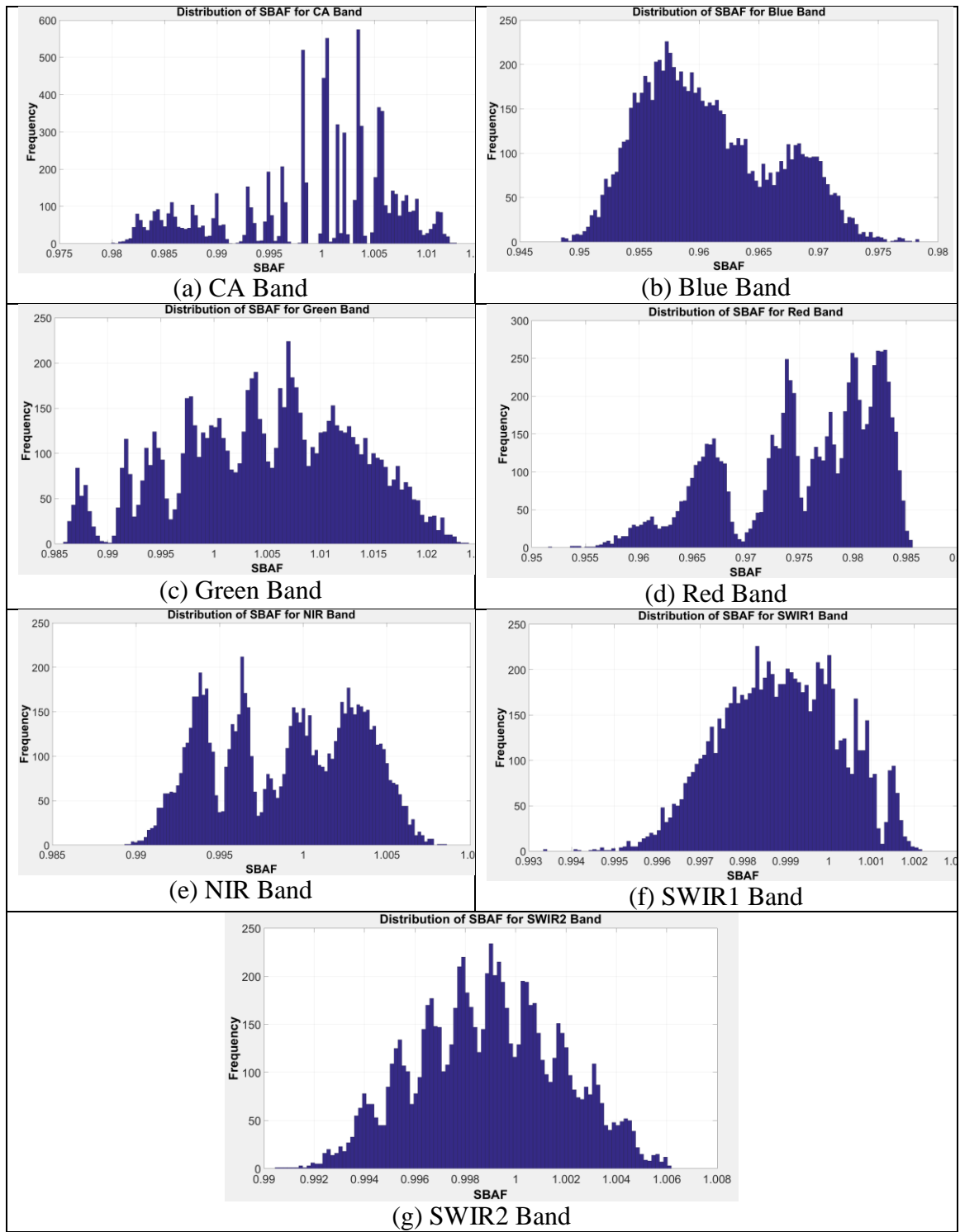


Figure 4.8 Distribution of SBAF After Simulation of SBAF Caused by Spectral Filter

Shift.

Table 4.8 shows the uncertainty across all the bands due to shifts in the spectral filter center wavelength. Not surprisingly, the uncertainty tends to be greater in the shorter wavelength bands and less in the longer wavelength bands. This is most likely due to the shorter wavelengths being more sensitive to absorption features as the center wavelength is shifted.

Bands	CA	Blue	Green	Red	NIR	SWIR1	SWIR2
Uncertainty(%)	0.78	0.58	0.82	0.71	0.43	0.14	0.28

Table 4.8 Bandwise SBAF Uncertainty Due to Spectral Filter Center Wavelength Shift.

4.5.1.3 Uncertainty Due to Spectral Bandwidth Change

Figures 4.9 (a)-(g) shows the distribution of simulated SBAFs due to changes in spectral filter bandwidth affecting both MSI and OLI. In the Coastal Aerosol and Blue bands, the SBAF distribution has a tail extending over greater SBAF values, while the other bands tend to have tails extending to smaller SBAF values. Table 4.9 shows the bandwidth change uncertainty in all bands. The uncertainty is lowest in the Coastal Aerosol band, at 0.01%, and largest in the Blue band, at 0.28%. In the Green, Red, NIR, SWIR1 and SWIR2 bands, the uncertainties are 0.12%, 0.10%, 0.05%, 0.03%, and 0.07%, respectively. These results are consistent with the range of SBAF values in each band – the Coastal Aerosol band had the smallest range (app. 0.0005), the Blue band had the largest range (app. 0.018), and the other bands had ranges of approx. 0.003 (NIR and SWIR1 bands), 0.004 (SWIR2 band), 0.007 (Green band), and 0.008 (Red band). In the Blue, Green, and Red bands, the differences in sensor RSR profiles are generally greater; smaller changes in bandwidth tend to result in larger variation in the SBAF value if the hyperspectral profile is also significantly changing within each sensor's RSR bandwidth.

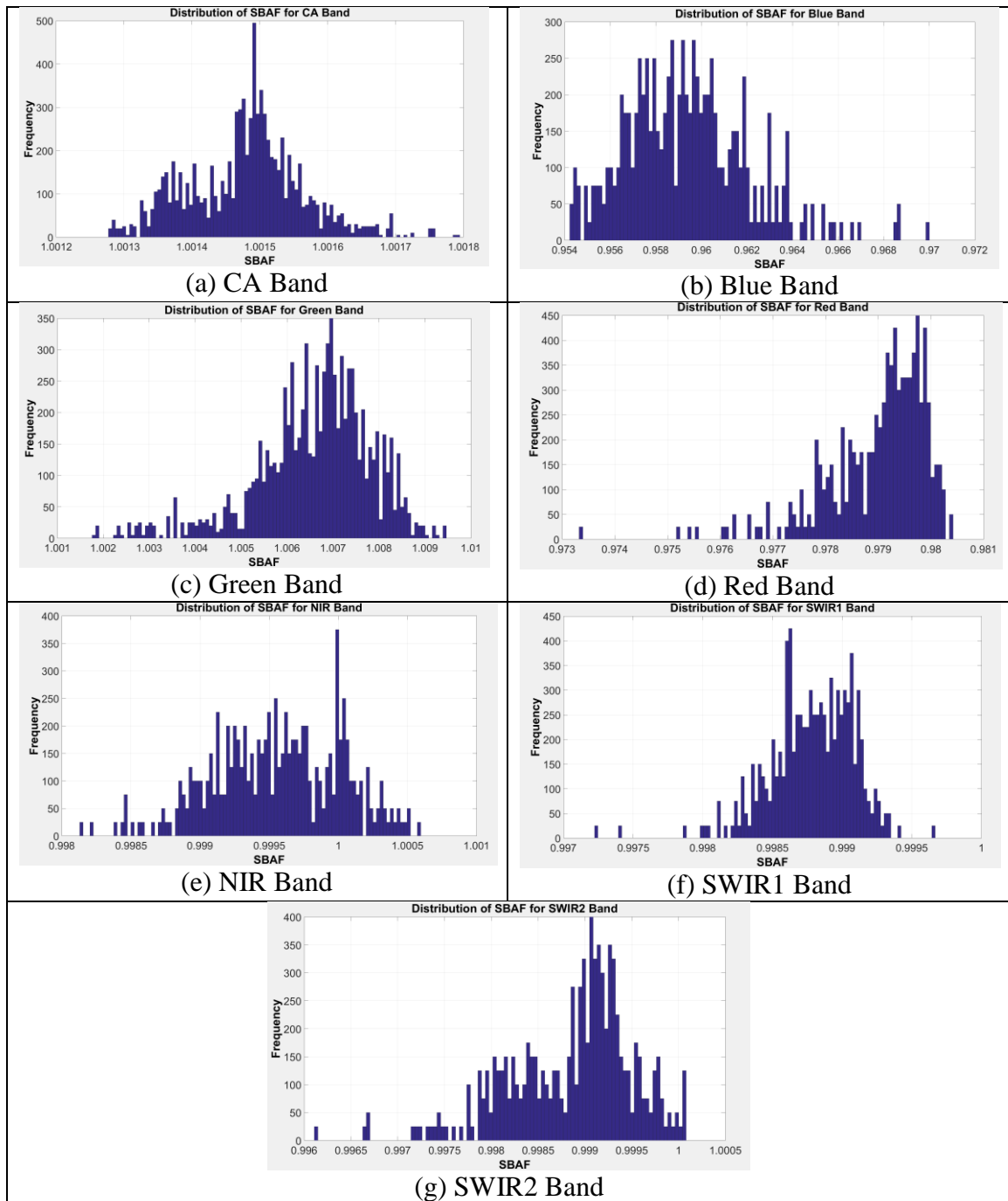


Figure 4.9 The Distribution of SBAF Due to the Change of Bandwidth.

Bands	CA	Blue	Green	Red	NIR	SWIR1	SWIR2
Uncertainty(%)	0.01	0.28	0.12	0.10	0.05	0.03	0.07

Table 4.9 Uncertainty Due to Change of Bandwidth Change of OLI and MSI.

4.5.2 Uncertainty in Spatial Domain

Uncertainty estimates due to errors in image registration and sensor spatial resolution are presented in this section. Results are presented for MSI scenes acquired over a representative bright target site (Libya4 PICS) and dark target site (Lake Tahoe, NV). It should be noted that these estimates are based on summary statistics derived from the reflectance values of the pixels within the ROI currently used for the given site.

4.5.2.1 Uncertainty due to Image Registration Error

Figures 4.10(a)-(g) show the distribution of mean TOA reflectances due to differences in image registration for the Libya4 scene acquired 03/09/2016. Similarly, Figures 4.11(a)-(g) show the distribution of mean TOA reflectances due to differences in image registration error for the Lake Tahoe scene acquired 05/22/2016.

Table 4.10 gives the corresponding estimated uncertainties due to image registration errors for both sites. For the Libya4 PICS, the estimated uncertainties are less than 0.03% in all bands. The smallest uncertainty, approx. 0.0078%, is observed in the SWIR2 band, while the largest uncertainty, app. 0.026% is observed in the Green band.

For the Lake Tahoe site, the estimated uncertainties are significantly greater. The smallest uncertainty, approx. 0.5%, is observed in the Coastal Aerosol band, while the largest uncertainty, app. 1.87%, is observed in the SWIR2 band. These results should not be surprising given the overall low signal levels in this part of the scene – the mean for the Red, SWIR1 and SWIR2 bands is likely smaller in magnitude than the corresponding standard deviation.

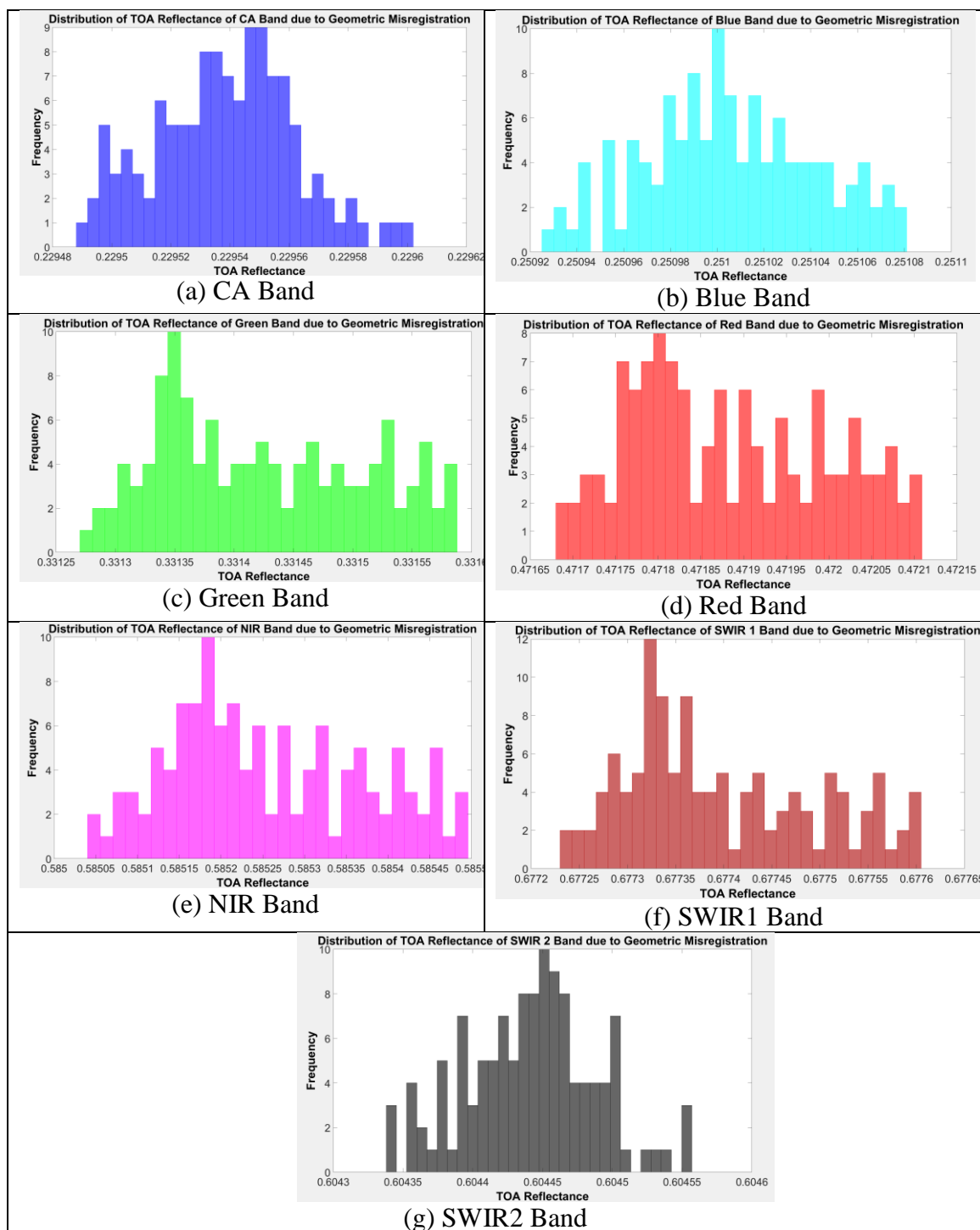


Figure 4.10 Distribution of TOA Reflectances from MSI Scene of Libya4 PICS,

03/09/2016.

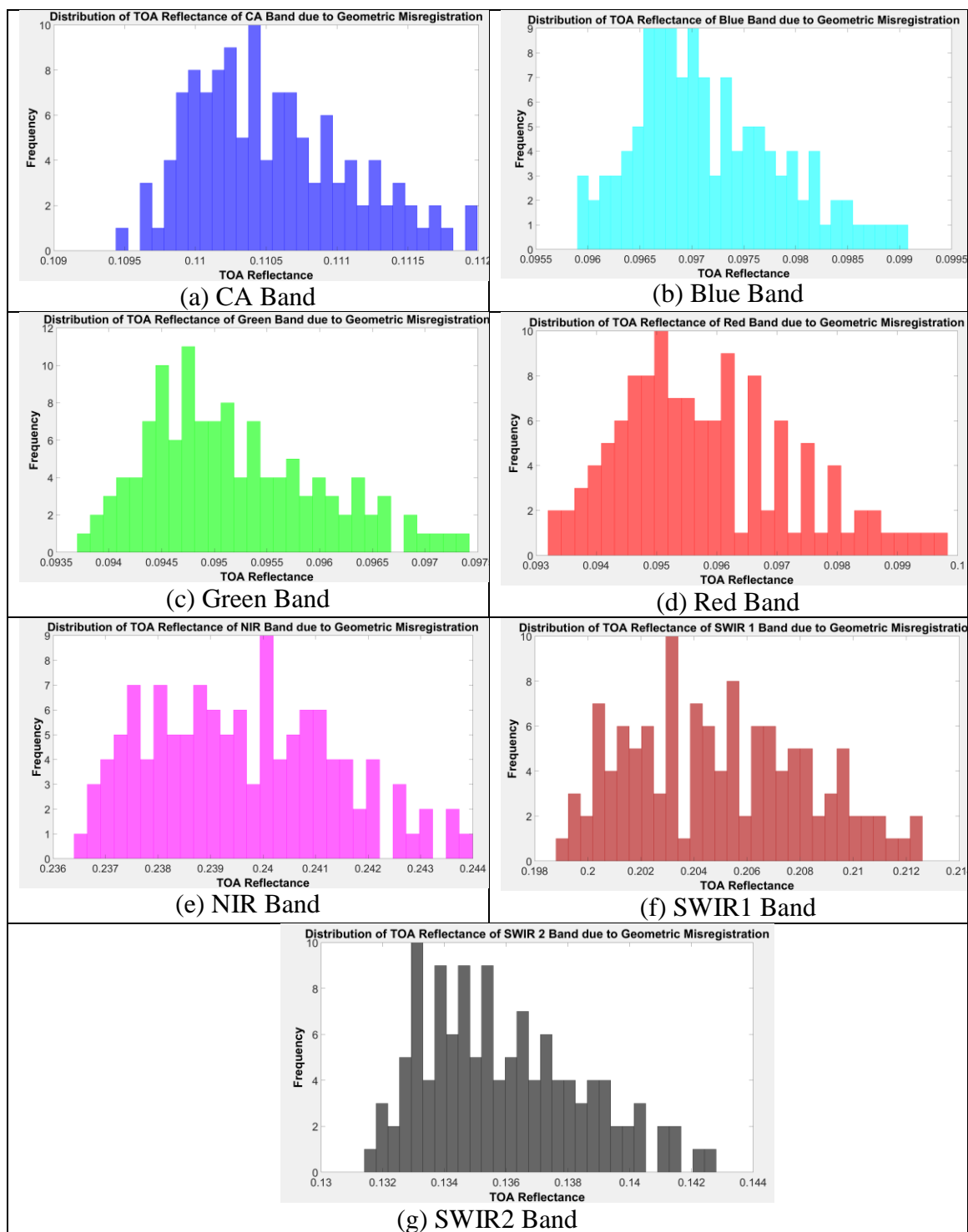


Figure 4.11 Distribution of TOA Reflectances for Lake Tahoe MSI scene, 05/22/2016.

Bands	Libya 4	Lake Tahoe	
	Uncertainty(%)	Uncertainty(%)	Standard Deviation
CA	0.0103	0.5034	0.0006
Blue	0.0145	0.7229	0.0007
Green	0.0260	0.8562	0.0080
Red	0.0242	1.5146	0.0015
NIR	0.0199	0.7357	0.0018
SWIR1	0.0146	1.6321	0.0033
SWIR2	0.0078	1.8696	0.0025

Table 4.10 Uncertainty Due to Image Registration Error of Libya 4 and Lake Tahoe.

4.5.2.2 Uncertainty due to Spatial Resolution Mismatch

Table 4.11 shows the estimated uncertainties due to spatial resolution differences in MSI with respect to OLI, as determined for individual scenes of the Libya4, Libya1, and Niger2 PICS. The estimated uncertainties are less than 0.01% in all bands, with slightly larger uncertainties in the Blue and Coastal Aerosol bands. For the purposes of this thesis, these uncertainty levels can be considered negligible.

Bands	Uncertainty(%)		
	L4	L1	N2
CA	0.0021	0.0012	0.0060
Blue	0.0008	0.0009	0.0010
Green	0.0004	0.0006	0.0001
Red	0.0002	0.0010	0.0080
NIR	0.0007	0.0091	0.0017
SWIR 1	0.0015	0.0014	0.0008
SWIR 2	0.0009	0.0005	0.0008

Table 4.11 Uncertainty Due to Spatial Resolution Mismatch.

4.5.2.3 Uncertainty due to Site Spatial Non-Uniformity

Table 4.12 shows the uncertainty due to spatial non-uniformity for the bright target PICS. The estimated uncertainty for all sites is within 3%, which is to be expected given that the ROI selection criterion was that the total spectral, temporal, and spatial uncertainty was to be within 3%.

Band	Libya4	Libya1	Niger2	Sudan1
CA	1.56	1.77	0.86	0.96
Blue	1.35	2.22	1.13	1.23
Green	1.80	1.79	1.30	1.22
Red	1.36	1.25	1.43	1.29
NIR	1.54	1.26	1.39	1.26
SWIR1	1.35	1.26	0.95	0.88
SWIR2	1.32	1.07	1.07	1.01

Table 4.12 Uncertainty Due to Site Inhomogeneity.

4.5.3 Uncertainty in Temporal Domain

4.5.3.1 Uncertainty Due to Overpass Time Difference

To estimate the uncertainty related to overpass time differences, the TOA reflectance of the Libya4 PICS was simulated in MODTRAN over varying solar elevation and azimuth angles. A ‘summer’ overpass date of 06/22/2017 (DOY 173) and a ‘winter’ overpass date of 12/31/2017 (DOY 365) were selected as the simulation dates, as these dates had the most extreme solar positions. The range of overpass times on both dates was set at 30 minutes, starting at 09:00 AM UTC (app. 5 minutes after the OLI overpass) and ending at 09:30 AM UTC (app. 12 minutes after the MSI overpass). An auxiliary MATLAB function script was used to estimate the solar position throughout the time range in increments of 30 seconds.

Figure 4.12 shows the reference surface reflectance profile used by MODTRAN to estimate TOA reflectance for the Libya4 PICS.

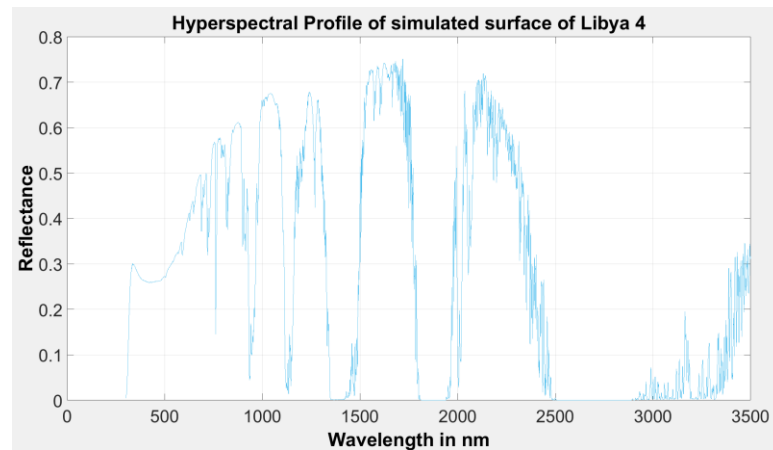


Figure 4.12 Hyperspectral Reference Surface Reflectance Profile.

Figure 4.13 shows the resulting variation of absolute and relative TOA reflectance over the Libya4 PICS on DOY 173. Only the Coastal Aerosol and SWIR2 bands are presented here; the remaining bands are shown in Appendix, as the overall pattern of variation is quite similar. Figure 4.14 shows the resulting variation of absolute and relative TOA reflectance on DOY 365.

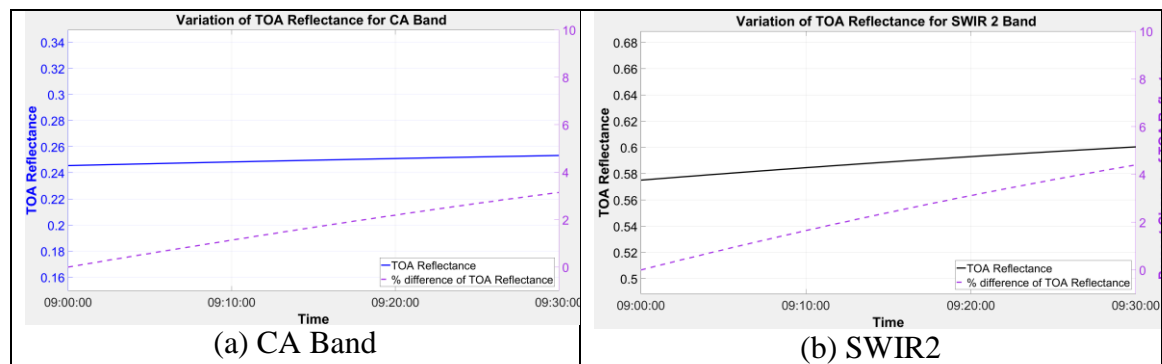


Figure 4.13 MODTRAN Simulated TOA Reflectance over Libya4 PICS, 06/22/2017 (DOY 173).

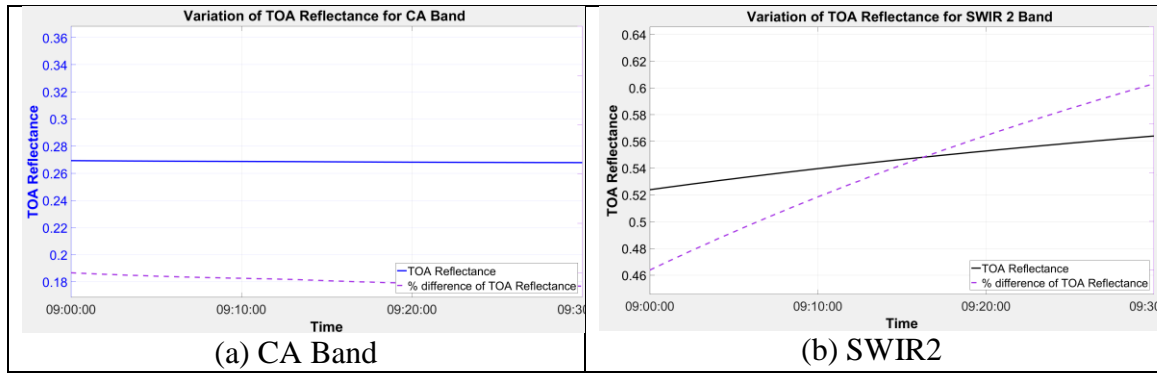


Figure 4.14 MODTRAN Simulated TOA Reflectance over Libya4 PICS, 12/31/2017 (DOY 365).

All bands but the Coastal Aerosol band show similar variation in TOA reflectance on both days. In the Coastal Aerosol band, the TOA reflectance appears to be slightly decreasing over time. The results for rest of the bands are shown in Appendix.

Table 4.13 summarizes the worst-case percent difference in TOA reflectance on both dates (“worst-case” referring to the difference in TOA reflectance between the simulation starting and ending times). On both dates, the estimated percent differences tend to be lower in the shorter wavelength bands and higher in the longer wavelength bands. In addition, the NIR, SWIR1 and SWIR2 band differences are slightly lower than the Green and Red band differences. The percent differences in the Coastal Aerosol and Blue bands are significantly lower on DOY 365 as compared to DOY 173, and significantly higher in the Green, Red, NIR, SWIR1 and SWIR2 bands. This observed behavior is consistent with the results obtained for BRDF correction, as the degree of correction was much less significant in the Coastal Aerosol and Blue bands. It can be concluded that effects due to varying solar angles are significantly greater in the longer wavelength bands.

Bands	%Difference@DOY 173	%Difference@DOY 365
CA	3.15	-0.55
Blue	3.57	1.09
Green	4.64	7.00
Red	4.58	8.00
NIR	3.92	5.85
SWIR1	4.01	6.00
SWIR2	4.40	7.66

Table 4.13 Highest Percent Difference on DOY 173 and DOY 365.

The parameters used for this simulation are -

Latitude=28.815753⁰

Longitude=23.372903⁰

Altitude=118m

Summary statistics for the simulated TOA reflectances and the corresponding uncertainties are given in Table 4.12.

Bands	%Uncertainty @DOY 173	%Uncertainty @DOY 365
CA	0.92	0.17
Blue	1.04	0.32
Green	1.34	2.00
Red	1.32	2.27
NIR	1.13	1.67
SWIR1	1.16	1.72
SWIR2	1.27	2.17

Table 4.14 Uncertainty in Simulated TOA Reflectance at DOY 173 and 365 over Libya4.

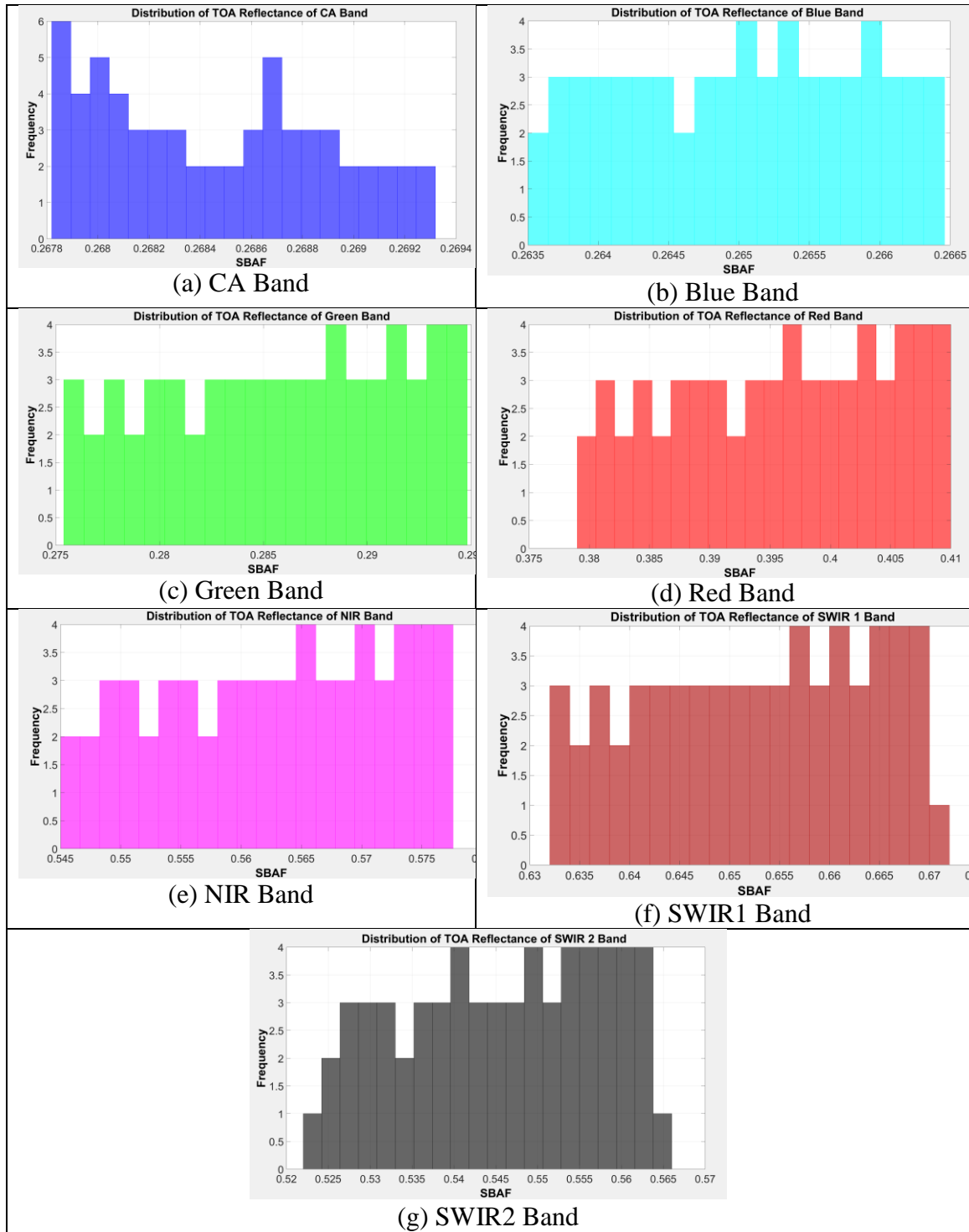


Figure 4.15 Distribution of Simulated Mean TOA Reflectance, DOY 365.

From Table 4.14 it can be inferred that the uncertainty is consistent with the uncertainties estimated from the non-BRDF corrected reflectances. As might be expected, there appears to be a seasonal dependence to the estimated uncertainty. During the summer, the largest

uncertainties are observed in the Green and Red bands, followed by the SWIR2 band; during the winter, the largest uncertainties are observed in the Red and SWIR2 bands, followed by the Green band. In addition, the observed uncertainties in the Coastal Aerosol and Blue bands are on the same magnitude on DOY 173 and DOY 365, on the order of 1% and around 0.3% respectively. Again, this behavior supports the observation that changes in solar geometry tend to have a greater impact on TOA reflectance at longer wavelengths.

4.5.3.2 Uncertainty due to Atmospheric Variation

To estimate the uncertainty due to changes in atmospheric characteristics, additional MODTRAN simulations were performed to generate TOA reflectances of the Libya4 PICS. For these simulations, the overpass time was kept constant at 09:30 AM UTC, but the water vapor content and aerosol optical depth were varied. One thousand normally distributed random samples of water vapor content were generated from a baseline mean value of $2.8 \pm 0.7 \text{ g/cm}^2$; similarly, one thousand normally distributed random samples representing aerosol optical depth were generated with respect to a baseline value of 0.11 at 550 nm. The resulting distributions are shown in Figures 4.16(a) and 4.16(b).

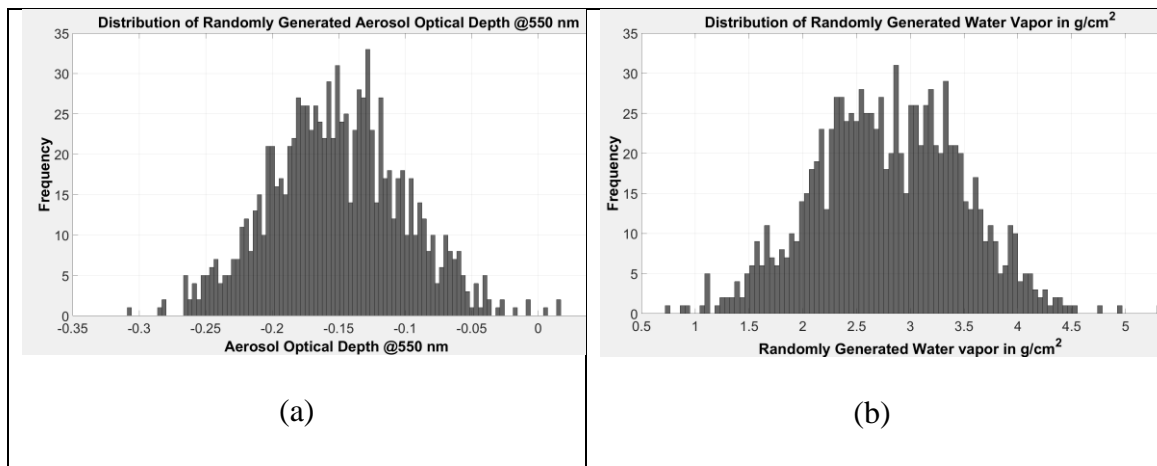


Figure 4.16 (a) Generated Random Aerosol Optical Depth at 550nm, (b) Generated

Random Water Vapor.

Figure 4.17 (a)-(g) show the resulting distributions of simulated TOA reflectance at the Libya4 PICS, on DOY 173 at 09:30 AM UTC. The distributions in the Coastal Aerosol and Blue bands appear to be skewed towards higher reflectance values; the distribution in the other bands is close to normal. This is as expected, as the Coastal Aerosol and Blue bands are more sensitive to changes in aerosol optical depth.

Table 4.15 shows the uncertainty associated with the simulated TOA reflectances for all bands due to atmospheric variation over the Libya4 PICS. Overall, the estimated uncertainty is on the order of 0.25% (Blue band) to 1.25% (SWIR2 band). The largest uncertainty is found in the SWIR2 band, which is more sensitive to changes in atmospheric water vapor content. The uncertainties in the shorter wavelength bands are generally lower; the Coastal Aerosol band uncertainty is significantly higher (0.45%) than the Blue band uncertainty, as it i) measures lower signal levels overall and ii) is more sensitive to atmospheric aerosol content. For the Green, Red, NIR and SWIR1 bands, the estimated uncertainties are between approx. 0.49% and 0.82%.

Bands	CA	Blue	Green	Red	NIR	SWIR1	SWIR2
Uncertainty(%)	0.45	0.25	0.49	0.81	0.82	0.50	1.29

Table 4.15 Atmospheric Uncertainty Associated with Simulated TOA Reflectances.

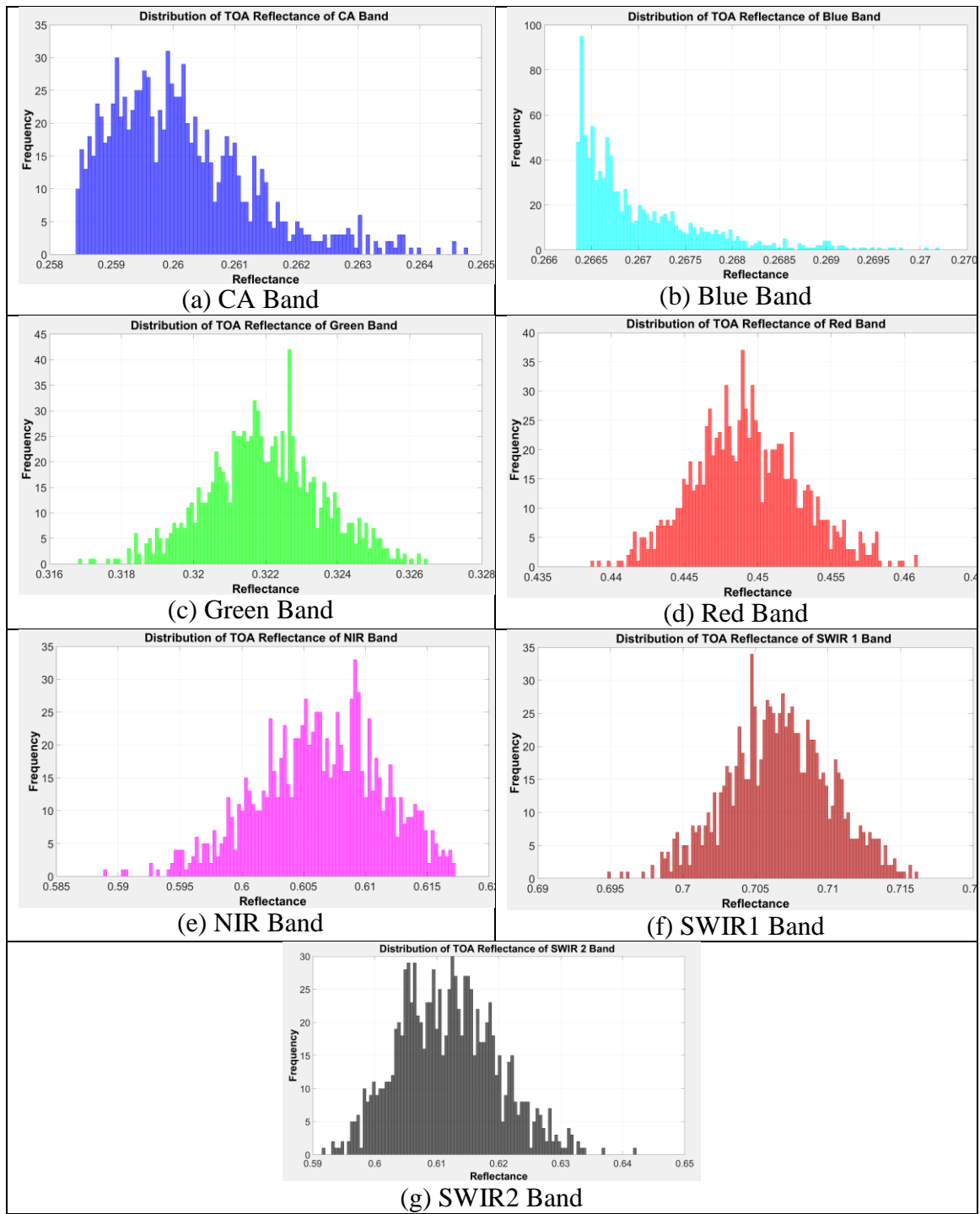


Figure 4.17 Simulated Reflectance with Randomly Sampled Water Vapor and Aerosol

Optical Depth at 550nm.

4.5.4 Summary of Uncertainty Analysis

Table 4.16 summarizes the worst-case uncertainties of all sources. The final uncertainty estimate was calculated using the root sum-of-squares method, under the assumption that all sources are independent of one another (i.e. the sources are uncorrelated).

Domain	Source of Uncertainty	Uncertainty (%)
Spectral	Measured RSR	1.000
	Spectral Filter shift	0.820
	Spectral Bandwidth Change	0.280
Spatial	Registration Error	0.026
	Spatial resolution Mismatch	0.002
	Site	1.800
Temporal	Overpass Time Difference	2.270
	Atmospheric Variation	1.290
Sensor	MSI Calibration	5.000
	OLI Calibration	3.000
Total Uncertainty		6.768

Table 4.16 Summary of all the Uncertainties.

The calibration uncertainties of the OLI and MSI are 3% and 5% respectively, are the most significant contributor to the overall uncertainty. Uncertainties due to atmospheric variability, target site non-uniformity, and differences in the measured sensor RSR also contributed significantly to the overall uncertainty. Uncertainties due to spatial registration errors and spatial resolution mismatch contribute little to the overall uncertainty.

4.6 Validation

Validation of the estimated cross calibration gains and biases was performed using 61 cloud free OLI and 37 cloud free MSI scenes of the Algodones Dunes target site in southeastern California, USA (WRS2 path 039, row 037). Summary statistics of the TOA reflectances from the Optimal ROI (SDSU IP Lab.) used for the site were analyzed with the parametric

2-sample t-test and nonparametric Wilcoxon Rank Sum test. Both parametric and nonparametric tests were employed due to lack of confidence in the assumption of a normal distribution in the reflectances; the observed distributions were more heavily skewed, with the direction of skew depending on the band.

Figures 4.18 (a) – (g) show box plots of each band's TOA reflectances for both sensors. In each figure, the first two box plots show the OLI and MSI reflectances after SBAF correction alone; the next two plots show the OLI and MSI reflectances after SBAF and BRDF correction; and the final two plots, respectively, show the MSI reflectances after application of gain only and application of gain and bias respectively. Box plots of the observed reflectance distribution were analyzed because the temporal sampling frequency for both sensors was not the same, especially due to exclusion of cloudy scenes. The difference in the resulting number of useable scenes for the analysis would adversely bias the estimated reflectance means towards a lower uncertainty for the sensor with fewer scenes.

As seen in Figure 4.16(a), the OLI TOA reflectance after BRDF correction was slightly higher than the corresponding MSI TOA reflectance after SBAF and BRDF correction, especially in the Blue and Green bands. After application of either set of gains to the MSI reflectances, the differences were decreased by essentially the same amount in both cases.

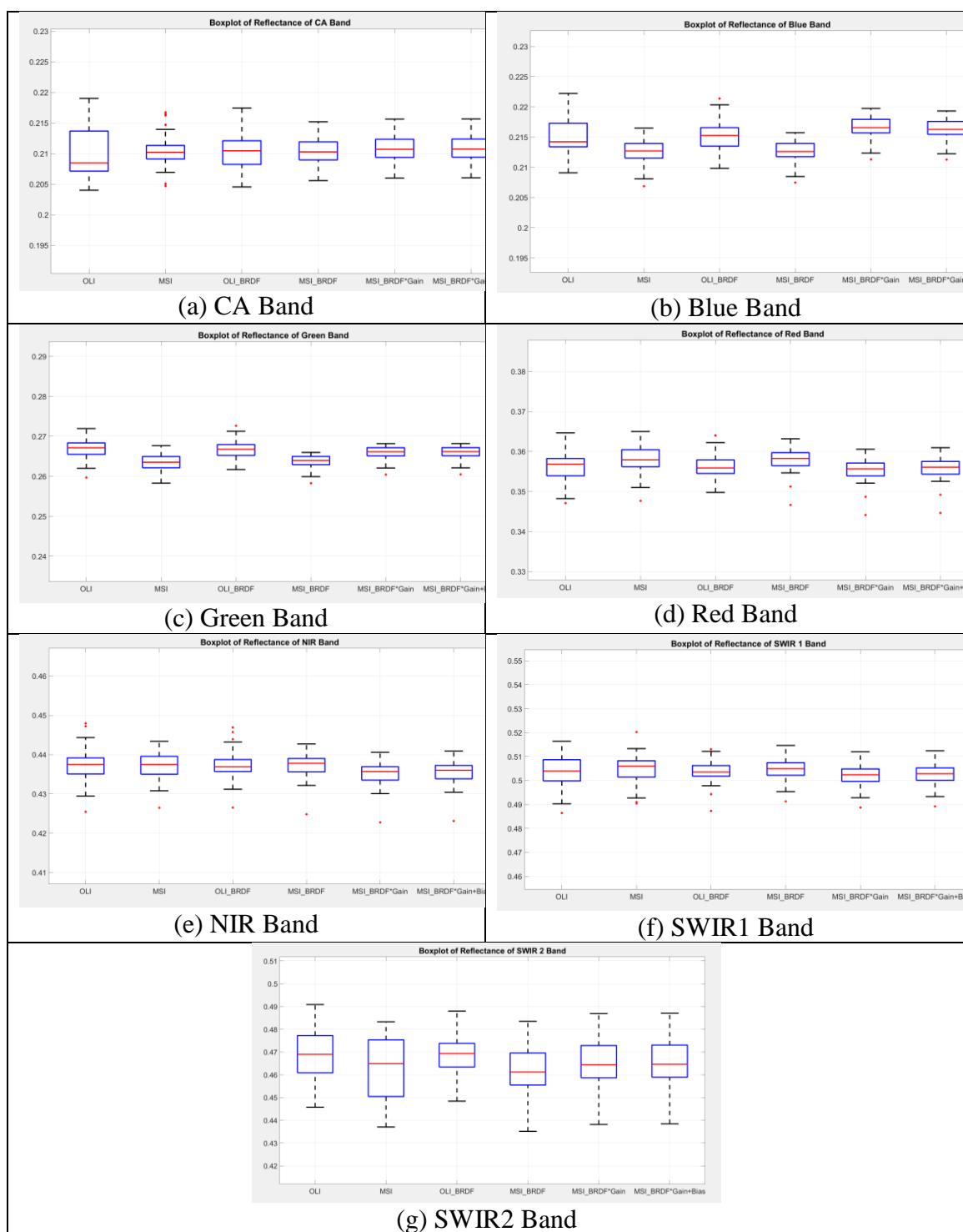


Figure 4.18 Boxplot of OLI and MSI Reflectance Before and After BRDF Correction, MSI After Applying Both set of Gain, Algodones Dunes.

In general, although the relative difference between the OLI and MSI reflectance distributions was small, application of the cross calibration gains and offsets observably improved inter-sensor agreement across all bands.

Statistical tests were performed to quantitatively verify the observed improvement in inter-sensor agreement. First, the two-sample t test was run assuming the variances in TOA reflectance of the sensors are equal after BRDF correction, with an additional, implicit assumption that each sensor's reflectances are normally distributed. The 2 sample t test statistic is given by

$$t = \frac{\overline{X}_2 - \overline{X}_1}{S \sqrt{\frac{1}{n_1} + \frac{1}{n_2}}}$$

where the reflectance standard deviations for both sensors are equal to a value S , n_1 is the number of OLI reflectance measurements, and n_2 is number of MSI reflectance measurements. The null hypothesis under test is that the reflectance means are equal, against the hypothesis that the reflectance means are not equal. The test was performed as a two-tailed test at the 95% significance level.

To check the validity of the t -test results, the Wilcoxon Rank Sum test was performed with the same null and alternative hypotheses. The test was also performed at a 95% confidence interval. Table 4.14 shows the results obtained from both tests, using both sets of gains to perform the cross calibration.

Bands	Set of Gain	2 sample t test		Wilcoxon Rank Sum Test	
		Null Hypothesis	p value	Null Hypothesis	p value
CA	Gain	Fail to Reject	0.3455	Fail to Reject	0.2846
	Gain and Bias	Fail to Reject	0.3176	Fail to Reject	0.2529
Blue	Gain	Reject	0.0079	Reject	0.0030
	Gain and Bias	Reject	0.0350	Fail to Reject	0.141
Green	Gain	Reject	0.0248	Fail to Reject	0.0933
	Gain and Bias	Reject	0.0284	Fail to Reject	0.1007
Red	Gain	Fail to Reject	0.1663	Fail to Reject	0.4076
	Gain and Bias	Fail to Reject	0.4532	Fail to Reject	0.8719
NIR	Gain	Reject	0.0010	Reject	0.0015
	Gain and Bias	Reject	0.0043	Reject	0.0080
SWIR1	Gain	Reject	0.0409	Reject	0.0312
	Gain and Bias	Fail to Reject	0.1129	Fail to Reject	0.1007
SWIR2	Gain	Fail to Reject	0.0959	Fail to Reject	0.0877
	Gain and Bias	Fail to Reject	0.1162	Fail to Reject	0.1069

Table 4.17 Comparison of Statistical Test Results for Cross Calibration Gain Applied to MSI Reflectances.

Based on the test results shown in Table 4.17, the following observations can be made:

- There was insufficient evidence to indicate differences between OLI and MSI mean TOA reflectances in the Coastal Aerosol, Red, and SWIR2 bands. The offset was not a statistically significant factor in these bands; the estimated gains were essentially equal.
- There was sufficient evidence to indicate differences between OLI and MSI mean TOA reflectances in the NIR band. The difference was more statistically significant

when only the gain was applied, as the p-value in this case was significantly smaller than the corresponding p-value when gain with offset was applied. This might be expected given the outliers in this band's OLI reflectances. Even so, the differences did not appear to be physically significant.

- For the Green band, there was sufficient evidence to indicate differences between OLI and MSI mean TOA reflectances according to the two-sample t test, but insufficient evidence to indicate differences according to the Wilcoxon Rank Sum test. This should be expected given the apparent non-normality of the OLI reflectance distribution.
- In the Blue band, there was insufficient evidence to indicate differences between OLI and MSI mean TOA reflectance according to the Wilcoxon test when gain only was used in the cross calibration. According to the two-sample t test and the Wilcoxon test when gain with offset was used in the cross calibration, there was sufficient evidence to indicate differences. Again, this is likely due to the non-normal distribution observed for the OLI reflectances. The disagreement in the Wilcoxon test results follows from the fact that the cross calibration offset in this band was significant.
- In the SWIR1 band, there was sufficient evidence to indicate differences between OLI and MSI mean TOA reflectance when gain only was used in the cross calibration, but insufficient evidence to indicate difference when gain with offset was used. The evidence for difference in the gain only case was “weak”, i.e. the p-values were not significantly less than 0.05. This may be explained by the fact that the MSI reflectance variance was larger than the corresponding OLI reflectance

variance, which violates the assumption of equal variance required by the two-sample t test.

With the exception of the SWIR1 band, the OLI reflectance variances were larger than the corresponding MSI reflectance variances due to the much larger amount of available OLI data.

Anomaly ID	Title	02.00	02.01		02.02	02.03	02.04
		Deployed 11/23/2015	Deployed 01/27/2016	Deployed 03/31/2016	Deployed 05/03/2016	Deployed 06/09/2016	Deployed 06/15/2016
3	Incorrect tile numbering	yes					
4	Instrument Measurement Time MTD	yes	yes	yes	yes	yes	yes
5	Minimum Reflectance "0"	yes	yes				
6	Detector Footprint at Equator	yes	yes				
7	Missing Physical Gains MTD	yes	yes	yes	yes	yes	yes
8	Shifted Pixels	yes, until 25/01/2016					
11	Missing Viewing Angles MTD	yes (random)	yes (random)				
12	Anomalous Pixels	yes	yes	yes			
15	Strong Mis-registration					yes	

Table 4.18 Sentinel 2A Different Processing Versions and Their Anomalies [41].

While all of the OLI data has been processed to a consistent baseline, the same cannot be said of the MSI data. Image data from 2015 were processed to baseline version 2.04, while image data from 2017 and 2018 were processed to baseline version 2.05 or 2.06. Depending on the kind and amount of change between baseline versions, this could be expected to cause or contribute to some discrepancies in the results. Table 4.15 shows the identified “anomalies” in the Sentinel 2A MSI image data at different versions and the dates when corrections were officially deployed. Clearly, there are major differences between the different processing baselines [41].

The Algodones Dunes site is not currently considered as an appropriate PICS for sensor calibration. Its surface characteristics and overall weather conditions are too variable compared to the Saharan Desert sites used to generate the cross calibration gains and offsets presented in this thesis. After application of the cross calibration gains with offsets, however, good agreement between the MSI and OLI reflectance distributions was achieved for this site. data for all the bands.

4.7 Summary

This chapter describes the results obtained the proposed cross calibration procedure. This final section summarizes the important results obtained during each stage of the process.

With the exception of Lake Tahoe, the absolute deviation from a unity SBAF factor for all target sites was on the order of 3% to 4% in the Blue band; for Lake Tahoe, the absolute deviation from a unity SBAF factor was on the order of 8%. For all target sites, the absolute deviation from a unity SBAF factor was on the order of 2% or less in the other bands. Smaller absolute deviations from unity SBAF were observed in the longer wavelength

bands, which can be explained by the fact that these bands have similar profiles and center location in both sensors.

The proposed 4 angles BRDF correction model appeared to show good potential for correction in the longer wavelength bands. Much less potential for correction was observed in the shorter wavelength bands. This can be explained by the fact that the Coastal Aerosol and Blue bands are more sensitive to changes in atmospheric characteristics than direct changes in solar position.

When cross calibration gains and nonzero offsets are considered, the Blue and Red bands exhibited the largest deviations from unity gain, on the order of -2.6% and -1.44%, respectively. The Coastal Aerosol band was found to have the largest regression standard error and lowest corresponding R^2 value for this parameter. With the exception of the Blue band, the offset was not found to be statistically significant. When cross calibration gains are considered alone (given offsets of zero), the Blue band again exhibited the largest deviation from unity gain, on the order of 1.86%.

The largest contribution to the overall cross calibration uncertainty, 6.8%, is due to the uncertainty in each sensor's calibration; for the OLI this uncertainty is on the order of 3%, while for the MSI it is on the order of 5%. Temporal uncertainty due to differences in solar zenith and azimuth angles caused by the difference in local overpass times is the next largest component in the overall uncertainty, on the order of 2.27%. Potential shifts in the spectral filter location and/or bandwidth contributed up to 0.82% of the uncertainty in the SWIR2 band. The uncertainty due to image registration is within 0.55% across all bands.

Finally, the uncertainty due to differences in sensor spatial resolution in all bands is at a level that can effectively be ignored.

Overall, both sets of estimated gains were shown to improve the agreement between sensors for both PICS sites and sites such as Algodones Dunes in all bands, with the possible exception of the NIR band. Given the significance of the offset in the Blue band and the generally “better” statistical results, it is recommended that the set of cross calibration coefficients for each band include the estimated offset.

It is also recommended, given the relatively small number of data points and apparent deviations from a normal reflectance distribution in both sensors, that non-parametric methods of inference such as the Wilcoxon test be used when evaluating the efficacy of the derived cross calibration coefficients. Such non-parametric tests tend to be more resistant to the effects of potential outliers in the reflectance data, as the metric statistics are often median-based.

Chapter 5 Conclusion

A new cross calibration technique was developed for the Sentinel 2A MSI and Landsat 8 OLI sensors with the object of increasing data harmonization between them. The cross calibration was developed using reflectance data from Saharan Desert PICS and dark targets such as Lake Tahoe and the Libyan volcano. Specific uncertainties associated with each step of the proposed cross calibration were estimated, as was the overall uncertainty associated with the entire process. Finally, the proposed cross calibration was validated using image data acquired over the Algodones Dunes site.

5.1 Process Recommendations

Based on the results presented in Chapter 4, the following summary recommendations can be made regarding the present work:

- SBAFs should be estimated from as much available hyperspectral image data as possible. If too little data are used in the estimation, the resulting mean SBAF and associated uncertainty could be skewed towards either extreme.
- BRDF correction should explicitly be performed as part of the cross calibration procedure.
- For all bands, the offset should be included in the cross calibration calculations. It provided better agreement than when the cross calibration gain alone was used, and appeared to be required when performing cross calibration in the Blue band. Its inclusion would make the cross calibration calculations consistent across all bands. Table 5.1 shows the set of recommended cross calibration gains and biases.

Bands	CA	Blue	Green	Red	NIR	SWIR1	SWIR2
Gain	1.0012	0.9740	1.0046	0.9856	0.9923	0.9922	1.0051
Bias	0.0002	0.0092	0.0010	0.0030	0.0016	0.0018	0.0011

Table 5.1 Recommended Gain and Bias of Cross Calibration for Each Band.

- Uncertainties in sensor calibration contributed the most to the overall cross calibration uncertainty, on the order of 3% and 5% for the OLI and MSI, respectively. Spatial domain uncertainties relating to image registration errors and spatial resolution mismatch contributed the least to the overall uncertainty, on the order of 0.026% and 0.0002%, respectively. Temporal domain uncertainties due to overpass time differences—primarily the seasonal variability in the solar azimuth and zenith angles—and atmospheric parameter variation contributed significantly to the overall uncertainty, but to a lesser degree than the sensor calibration uncertainty. Spectral domain uncertainties due to spectral filter center wavelength shift and/or bandwidth change also contributed significantly to the overall uncertainty, but, again, to a lesser degree than the sensor calibration uncertainty.

5.2 Direction of Future Work

Future directions to potentially extend and enhance the cross calibration work presented in this thesis include the following:

- To simplify the cross calibration analysis, atmospheric effects were not explicitly taken into account. The use of desert PICS such as Libya4 as bright targets should minimize, to a certain extent, atmospheric effects directly over the land surface (with the exception of wind-blown sands and dust contributing to the aerosol

concentration). However, Libya4 is fairly near a significant water body (the Mediterranean Sea) that can contribute a significant degree of water vapor and/or aerosol concentration to the local atmosphere.

- The process to generate SBAFs depends on the availability of reasonably accurate hyperspectral profiles of the target. For this thesis, EO-1 Hyperion data were used to generate the hyperspectral profiles. This resulted in a restricted selection of calibration sites, as Hyperion either did not image them at all or imaged them inconsistently. Unfortunately, Hyperion has recently been decommissioned and is no longer providing data. Other readily available sources of hyperspectral data will need to be considered if cross calibration is to be carried out over time. With other sources of hyperspectral data, additional sites may be useable and allow a denser sampling across each sensor's dynamic range.
- Additional validation can be performed using another site such as Gobabeb, Namibia (WRS2 path 79, row 76) where RadCalNet data are also available. This is an arid area with minimal cloud cover. Validation sites should also include, if possible, vegetation target sites such as LaCrau in France (WRS2 path 196, row 30), or the Brookings, SD 3M site (WRS2 path 29, row 29).

References

- [1] D. L. Helder, B. L. Markham, K. J. Thome, J. A. Barsi, G. Chander and R. Malla, "Updated Radiometric Calibration for the Landsat-5 Thematic Mapper Reflective Bands," in *IEEE Transactions on Geoscience and Remote Sensing*, vol. 46, no. 10, pp. 3309-3325, Oct. 2008.
- [2] R. Muller, "Calibration and Verification of Remote Sensing Instruments and Observations", in *mdpi journal of Remote Sensing*, vol 6, pp. 5692-5695, June 2014.
- [3] Chandler, G.; Meyer, D. J.; Helder, D. L. "Cross Calibration of the Landsat-7 ETM+ and EO-1 ALI sensor". *IEEE Transactions on Geoscience and Remote Sensing*. 42, n. 12, p. 2821–2831, 2004.
- [4] P.M. Teillet, B. L. Markham, Richard R. Irish, " Landsat Cross-Calibration based on near simultaneous imaging of common ground targets" *Remote Sensing of Environment* 102(2006) 264-270.
- [5] Class lecture of Dr. Cibele Teixeira Pinto, EE 790, Spring 2017, Lecture 15.
- [6] F. Gascon, O. Thépaut et al. "Copernicus Sentinel-2 Calibration and Products Validation Status" , Preprints (www.preprints.org) ,NOT PEER-REVIEWED, Posted: 19 October 2016,doi:10.20944/preprints201610.0078.v1
- [7] Sentinel 2 Handbook available at:
https://sentinel.esa.int/documents/247904/685211/Sentinel-2_User_Handbook
[Last accessed: 08-11-2017]
- [8] <https://earth.esa.int/web/sentinel/user-guides/sentinel-2-msi/resolutions/spatial>
[Last accessed: 08-11-2017]

- [9] <https://landsat.gsfc.nasa.gov/the-worldwide-reference-system> [Last accessed: 08-11-2017]
- [10] Knight, Ed. J., and Geir Kvaran. "*Landsat-8 operational land imager design, characterization and performance*", Remote Sensing 6.11 (2014): 10286-10305.
- [11] <https://earth.esa.int/web/technical-guides/sentinel-2-msi/performance>[Last accessed: 08-11-2017]
- [12] J. A. Barsi, K. Lee, G. Kvaran, B. L. Markham and Jeffrey A. Pedelty, "*The Spectral Response of the Landsat-8 Operational Land Imager*", Remote Sensing, 2014, Vol. 6, pp. 10233
- [13] B. L. Markham, and D. L. Helder, "*Forty-year calibrated record of earth-reflected radiance from Landsat: A review*," *Remote Sensing of Environment*, vol. 122, pp. 30-40, 2012
- [14] D. L. Helder, B. Basnet and D. Morstad "*Optimized identification of worldwide radiometric pseudo-invariant calibration sites*," Canadian Journal of Remote Sensing, vol. 36, pp. 527-539
- [15] C. Nagaraja Rao and J. Chen, "*Inter-satellite calibration linkages for the visible and near-infrared channels of the Advanced Very High Resolution Radiometer on the NOAA-7, -9, and -11 spacecraft*," *International Journal of Remote Sensing*, vol. 16, pp. 1931-1942, 1995.
- [16] H. Cosnefroy, M. Leroy, and X. Briottet, "*Selection and characterization of Saharan and Arabian desert sites for the calibration of optical satellite sensors*," *Remote Sensing of Environment*, vol. 58, pp. 101-114, 1996.

- [17] G. Chander, A. Angal, D. L. Helder, N. Mishra, and A. Wu, "*Preliminary assessment of several parameters to measure and compare usefulness of the CEOS reference pseudo-invariant calibration sites*," in *Remote Sensing*, 2010, pp. 78262L-78262L-12.
- [18] L. Morstad, D. L. Helder, Dennis, "Use of Pseudo-Invariant Sites for Long-Term Sensor Calibration" International Geoscience and Remote Sensing Symposium (IGARSS), 2008, 1. I-253 . 10.1109/IGARSS.2008.4778841.
- [19] Philippe M. Teillet, G. Fedosejevs, K. J. Thome, "*Spectral band difference effects on radiometric cross-calibration between multiple satellite sensors in the Landsat solar-reflective spectral domain*", Proc. SPIE 5570, Sensors, Systems, and Next-Generation Satellites VIII, (4 November 2004); doi: 10.1117/12.562709
- [20] Chander, G. & Mishra, N. & Helder, D. & Aaron, D. & Choi, T. & Angal, A. & Xiong, X. (2010), "Use of EO-1 Hyperion data to calculate spectral band adjustment factors (SBAF) between the L7 ETM+ and Terra MODIS sensors", International Geoscience and Remote Sensing Symposium (IGARSS). 1667-1670. 10.1109/IGARSS.2010.5652746.
- [21] G. Chander, N. Mishra, D. L. Helder, D. B. Aaron, A. Angal, T. Choi, Xiaoxiong Xiong, David R. Doelling, "Applications of Spectral Band Adjustment Factors (SBAF) for Cross-Calibration", *Geoscience and Remote Sensing IEEE Transactions on*, vol. 51, pp. 1267-1281, 2013, ISSN 0196-2892.

- [22] Liu, JJ, Li, Z, Qiao, YL, Liu, YJ, Zhang, YX (2004), “*A new method for cross-calibration of two satellite sensors*”, International Journal of Remote Sensing, 25(23), 5267-5281.
- [23] Roujean, J. L., Leroy, M., and Deschamps, P. Y., 1992, “*A bi-directional reflectance model of the Earth’s surface for the correction of remote sensing data*”, Journal of Geophysical Research, 97, 20 455–20 468.
- [24] Schlapfer, D.; Richter, R.; Feingersh, T., “*Operational BRDF Effects Correction for Wide-Field-of-View Optical Scanners (BREFCOR)*” IEEE Transactions on Geoscience and Remote Sensing, vol. 53, issue 4, pp. 1855-1864.
- [25] Mishra, N.; Helder, D.; Angal, A.; Choi, J.; Xiong, X., “*Absolute Calibration of Optical Satellite Sensors Using Libya 4 Pseudo Invariant Calibration Site*” Remote Sens. **2014**, 6, 1327-1346.
- [26] Lacherade, S.; Fougne, B.; Henry, P.; Gamet, P., “*Cross Calibration Over Desert Sites: Description, Methodology, and Operational Implementation*” IEEE Transactions on Geoscience and Remote Sensing, vol. 51, issue 3, pp. 1098-1113
- [27] Mishra, N.; Haque, M.O.; Leigh, L.; Aaron, D.; Helder, D.; Markham, B. “*Radiometric Cross Calibration of Landsat 8 Operational Land Imager (OLI) and Landsat 7 Enhanced Thematic Mapper Plus (ETM+)*” . Remote Sens. **2014**, 6, 12619-12638
- [28] Li, S., Ganguly, S., Dungan, J.L., Wang, W.L. and Nemani, R.R. (2017) “*Sentinel-2 MSI Radiometric Characterization and Cross-Calibration with Landsat-8 OLP*”. Advances in Remote Sensing, 6, 147-159

- [29] Chander, G., D. L. Helder, D. Aaron, N. Mishra, and A. K. Shrestha. 2013. "Assessment of Spectral, Misregistration, and Spatial Uncertainties Inherent in the Cross-Calibration Study." IEEE Transactions on Geoscience and Remote Sensing 51: 1282–1296. doi:10.1109/TGRS.2012.2228008.
- [30] C. T. Pinto, F. J. Ponzoni, R. M. Castro, Larry Leigh, Morakot Kaewmanee, David Aaron & Dennis Helder, "Evaluation of the uncertainty in the spectral band adjustment factor (SBAF) for cross-calibration using Monte Carlo simulation", Remote Sensing Letters, 7:9, 837-846, DOI: 10.1080/2150704X.2016.1190474
- [31] J. Gorroño, A. C. Banks, N. P. Fox, C. Underwood, "Radiometric inter-sensor cross-calibration uncertainty using a traceable high accuracy reference hyperspectral imager", ISPRS Journal of Photogrammetry and Remote Sensing, pp 393-417
- [32] Teillet, P. M., et al. "Impacts of spectral band difference effects on radiometric cross-calibration between satellite sensors in the solar-reflective spectral domain." Remote Sensing of Environment 110.3 (2007): 393-409.
- [33] G. Chander et al., "Applications of Spectral Band Adjustment Factors (SBAF) for Cross-Calibration," in IEEE Transactions on Geoscience and Remote Sensing, vol. 51, no. 3, pp. 1267-1281, March 2013.
- [34] S. K. Chittimalli, "Reflectance Based Calibration and Validation of the Landsat Satellite Archive," South Dakota State University- Thesis Dissertation, 2016.
- [35] Chander, G., D. L. Helder, D. Aaron, N. Mishra, and A. K. Shrestha. 2013. "Assessment of Spectral, Misregistration, and Spatial Uncertainties Inherent in

- the Cross-Calibration Study.*” IEEE Transactions on Geoscience and Remote Sensing 51: 1282–1296. doi:10.1109/TGRS.2012.2228008
- [36] D. R. White, “*Propagation of Uncertainty and Comparison of Interpolation Schemes*”, Int J Thermophys (2017), 38:39, DOI: 10.1007/s10765-016-2174-6
- [37] Mishra, N.; Haque, M.O.; Leigh, L.; Aaron, D.; Helder, D.; Markham, B.
 “*Radiometric Cross Calibration of Landsat 8 Operational Land Imager (OLI) and Landsat 7 Enhanced Thematic Mapper Plus (ETM+)*.” Remote Sens. 2014, 6, 12619-12638.
- [38] J. A. Barsi, K. Lee, G. Kvaran, B. L. Markham and J. A. Pedelty, “The Spectral response of the Landsat-8 Operational Land Imager”, Remote Sens. 2014, 6, 10232-10251; doi:10.3390/rs61010232.
- [39] Sentinel 2 Data Quality Reports, pulished on February 8th, 2018 available at <https://sentinel.esa.int/documents/247904/685211/Sentinel-2-Data-Quality-Report> [Last Accessed 2/28/2018]
- [40] Vuppula, Harika, "*Normalization of Pseudo-invariant Calibration Sites for Increasing the Temporal Resolution and Long-Term Trending*" (2017). Theses and Dissertations. 2180. <https://openprairie.sdstate.edu/etd/2180>
- [41] <https://sentinel.esa.int/web/sentinel/missions/sentinel-2/news/-/article/new-processing-baseline-02-04-for-sentinel-2a-products> [Last Accessed: 03/07/2018]

Appendix

ROI and Sentinel 2A footprint over Landsat 8 image:

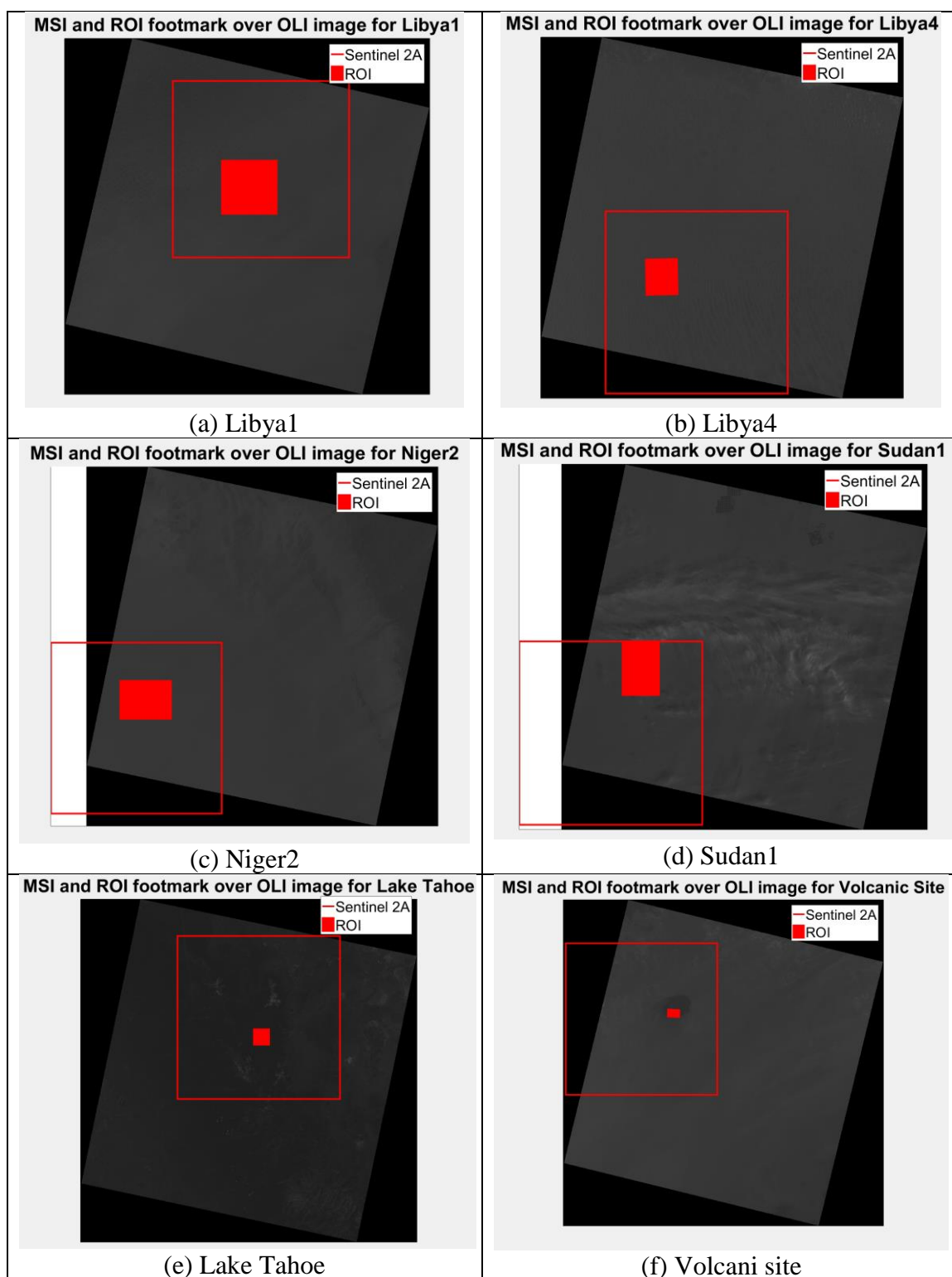


Figure A.1 OLI, MSI and ROI position for Target Sites.

ROI for Target Sites:

Target Site	WRS2 Path	WRS2 Row	ROI's UTM Coordinates in meter			
			ULX	ULY	LRX	LRY
Libya1	187	043	330150	2750850	365070	2716860
Libya4	181	040	723825	3171375	743805	3149685
Niger2	188	045	644190	2375910	677670	2350590
Sudan1	177	045	561570	2405850	584250	2367450
Lake Tahoe	043	033	751125	4337625	762315	4326405
Volcanic Near Libya	184	043	775652	2755834	784770	2749872

Table A.1 UTM Values for ROI Corner Coordinates for Target Sites.

Uncertainty Due to Overpass Time Difference:

Variation of Reflectance, DOY 173:

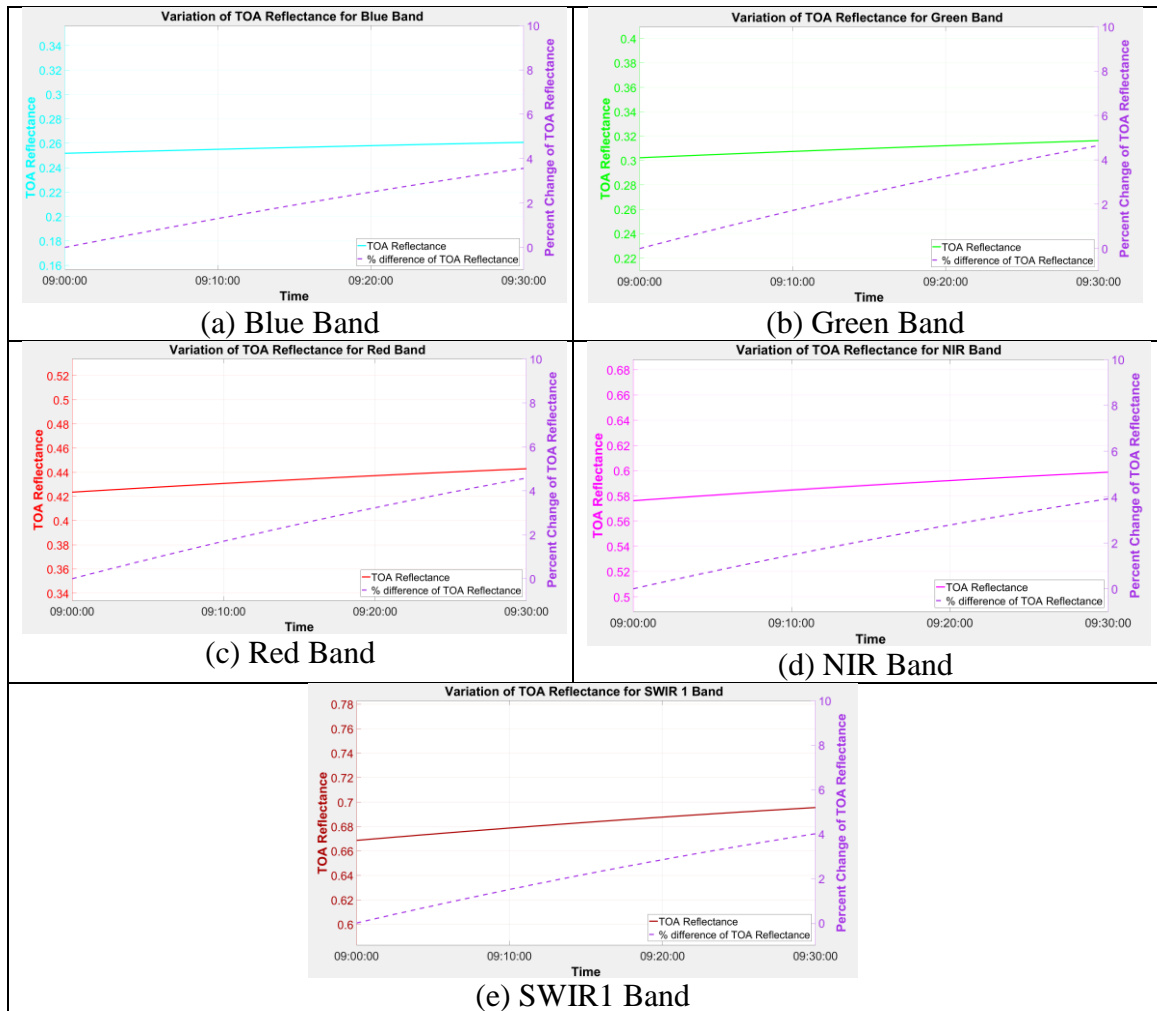


Figure A.2 Variation of Reflectance for Overpass Time Difference over Libya4 @DOY

Variation of Reflectance, DOY 365:

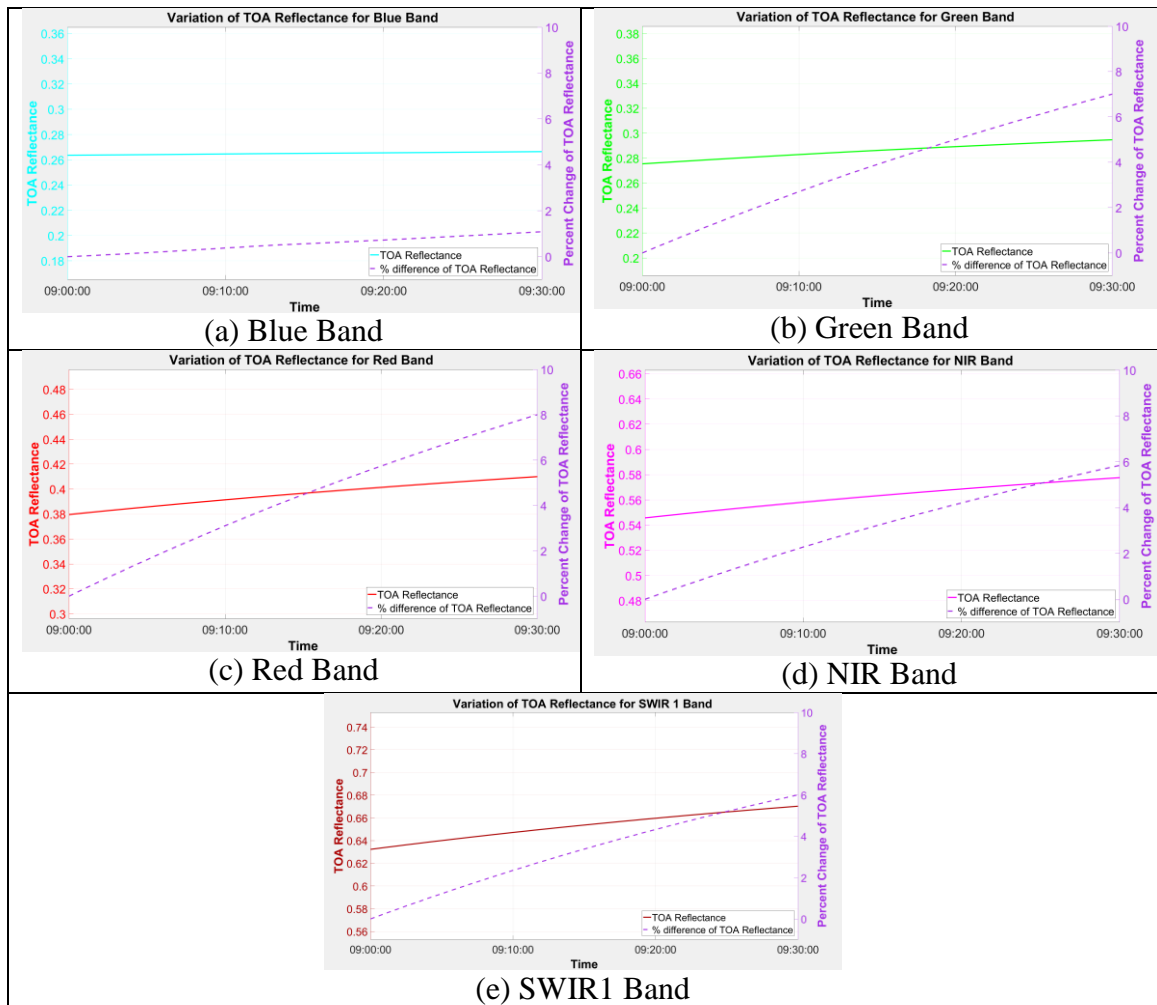


Figure A.3 Variation of Reflectance for Overpass Time Difference over Libya4 @DOY 365

TOA Reflectance Vs Spherical Coordinate Solar Angles

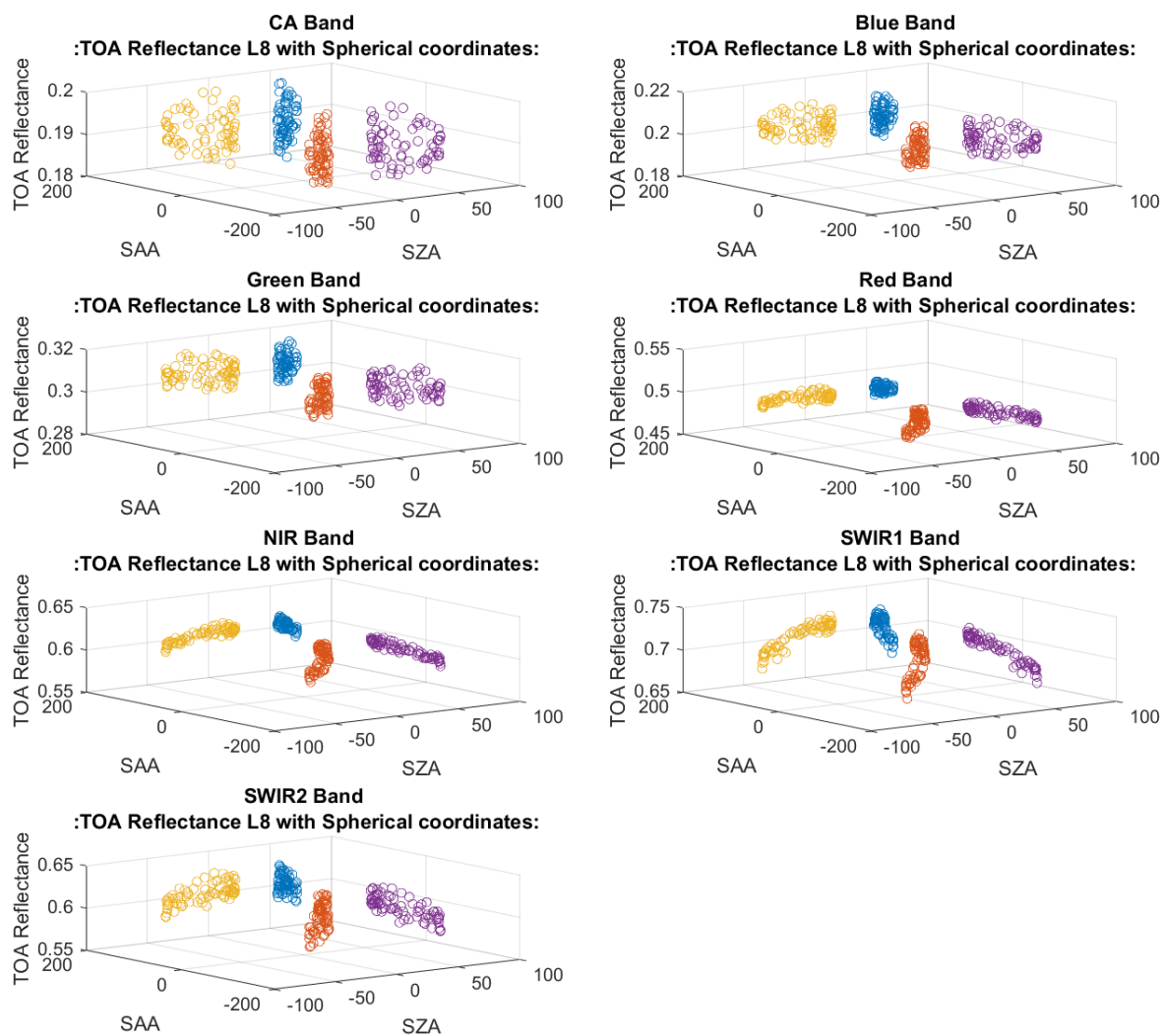


Figure A.4 Reflectance vs Spherical Coordinate Solar Angles

TOA Reflectance Vs Converted Cartesian Coordinate Solar Angles

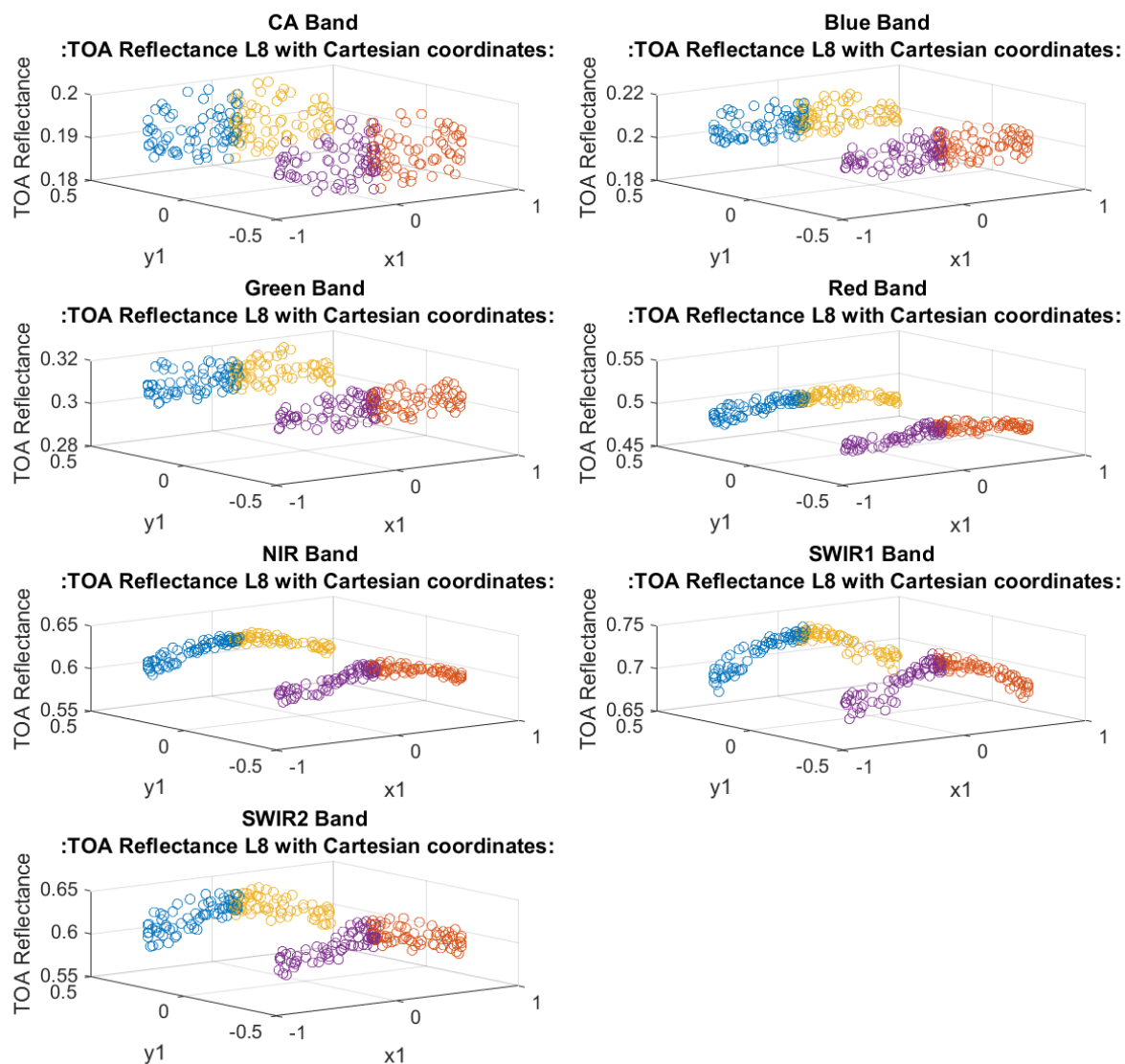


Figure A.5 Reflectance vs Cartesian Coordinate Converted Solar Angles.

TOA Reflectance Vs Spherical Coordinate View angles

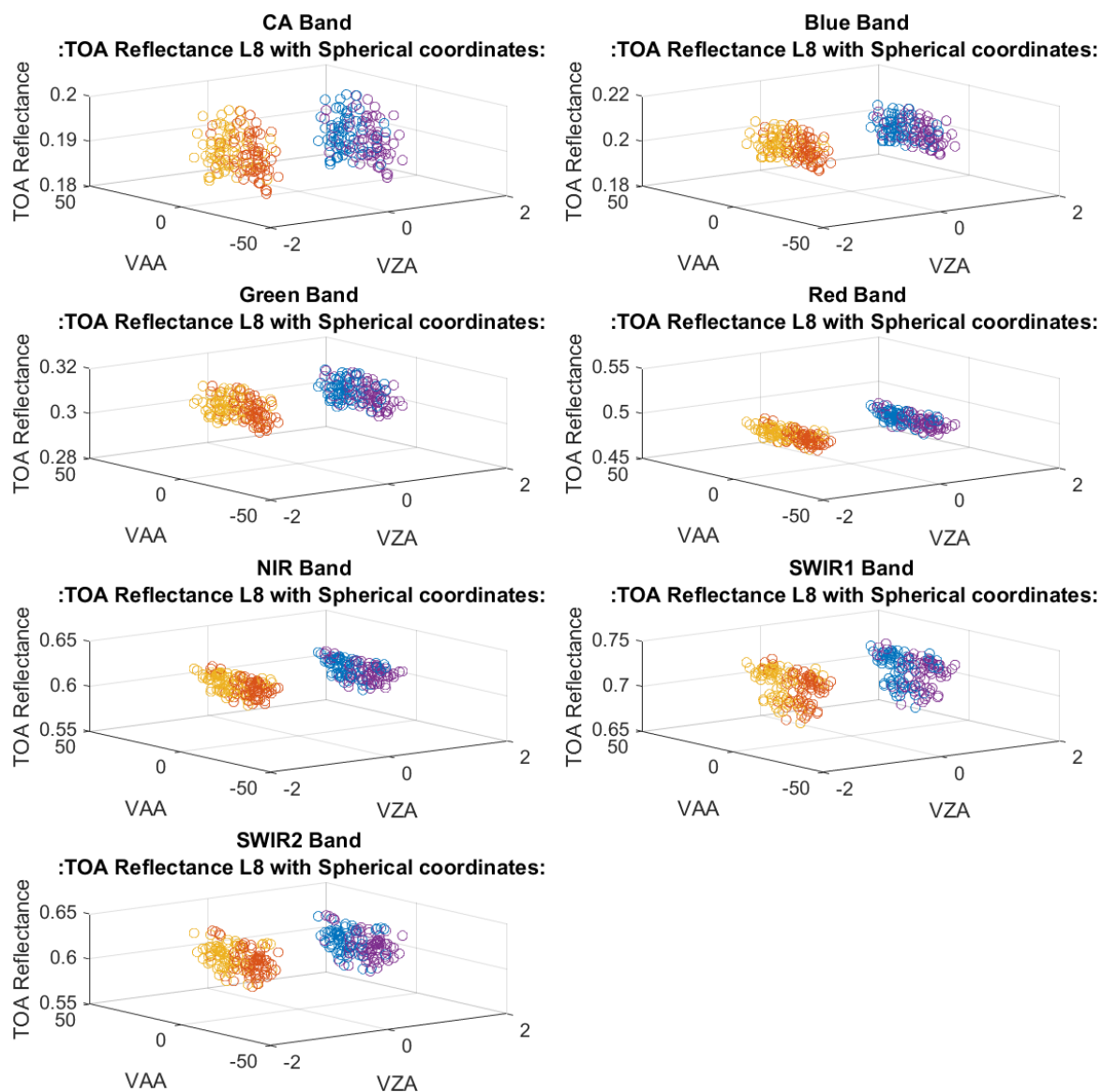


Figure A.6 Reflectance vs Spherical Coordinate View Angles

TOA Reflectance Vs Converted Cartesian Coordinate View angles

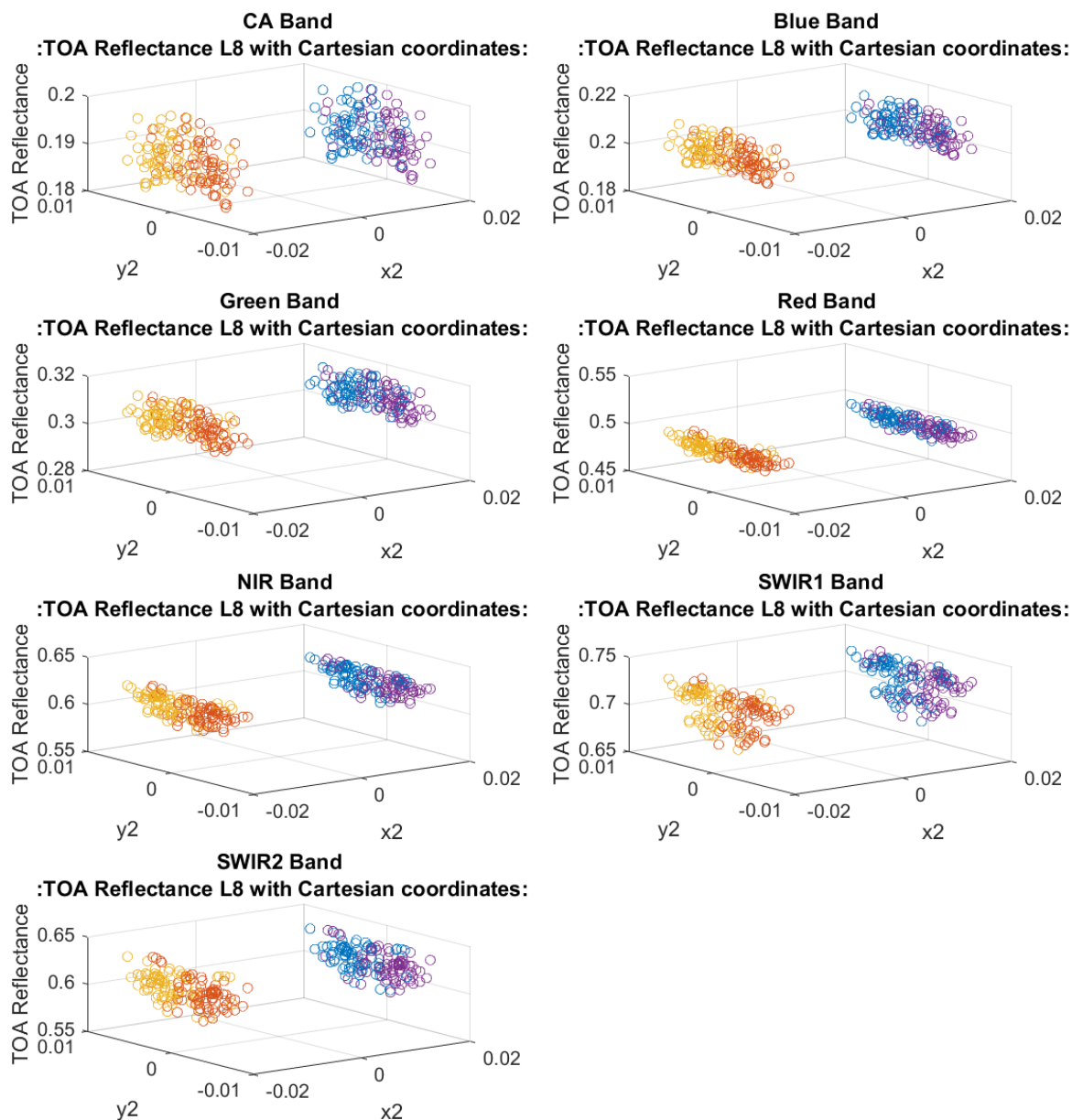


Figure A.7 Reflectance vs Cartesian Coordinate Converted Solar Angles.